THE GRADUATE UNIVERSITY FOR ADVANCED STUDIES, SOKENDAI

DOCTORAL THESIS

Measurement of Spin-orbit Obliquity of WASP-33b by Doppler Tomography and Transit Photometry

---

Author:
Noriharu WATANABE

Supervisor:
Dr. Norio NARITA
Dr. Yasunori HORI
Dr. Hideki TAKAMI
Dr. Aoki WAKO

A thesis submitted in fulfillment of the requirements for the degree of Doctor of Philosophy in the

Department of Astronomical Science

March 12, 2021

Abstract

This thesis describes the research of a hot Jupiter around hot stars for observing its nodal precession to measure its spin-orbit obliquity and the stellar quadrupole moment. The first discovered extra-solar planet, also known as an exoplanet, surprised us because that was a Jupiter-like planet orbiting very close (about 4-day orbital period) to its host star: this type of planet is hot Jupiter. There are 4200 confirmed exoplanets: 500 of them are hot Jupiters. Hot Jupiters are uncommon planets for our solar system and difficult to be born in situ following the classical planet formation. Thus, new orbital evolution models to bring them near the host stars have been proposed.

There are three major orbital evolution models of hot Jupiter. One model drops a hot Jupiter near its host star by the gravitational interaction between the planet and the gas disk (planet-disk interactive model) and often aligns the orbit with the stellar spin. Another model scatters more than three hot Jupiters by their mutual interactions (planet-planet scattering model), and the stellar rotation axis is inclined easily to the planetary orbital axis. The other model oscillates the orbit of hot Jupiter by the Kozai effect (Kozai-Lidov mechanism) and tends to make the obliquity distribution more widely than one via the planet-planet scattering. While the first model keeps an orbit circular, the second and the third ones make an orbit elliptic. Especially, the eccentric orbit gets circular by tidal evolution keeping its misaligned orbit.

However, a solar-like star, whose effective temperature is less than 6250 K, is realigned with a planetary orbit because its thick convective has been affected by the tidal dissipation. On the other hand, a hot star, whose effective temperature is more than 7000 K, has no convective zones and hardly undergoes realignment. Thus, the spin-orbit obliquity of hot Jupiter around the hot star is the clue to understanding its origin.

Doppler tomography is a powerful method to measure the spin-orbit obliquity of hot Jupiters around hot stars by transit spectroscopy. Nevertheless, a single observation can only measure the projected one and never detect the real one. The nodal precession occurs and moves the transit trajectory when a hot Jupiter revolves around a hot star, which tends to be oblate by its fast rotation, in the misaligned

orbit. The larger stellar quadrupole moment J_2, which is the index of the stellar oblateness, makes the speed of the nodal precession faster. This movement changes two orbital parameters, projected spin-orbit obliquity and impact parameter, which is available by more than one observation. In terms of measuring an impact parameter, transit photometry is also a valuable method for the nodal precession. Finally, we can measure the real spin-orbit obliquity by the two variations.

WASP-33b, a hot Jupiter around a hot star, is the only planet whose real spin-orbit obliquity has been measured by the nodal precession via Doppler tomographic observation. However, because the previous study measured it by only two-epoch Doppler tomographic datasets, it is not enough to confirm WASP-33b's nodal precession. Thus, I observed WASP-33b using HIgh Dispersion Echelle Spectrograph (HIDES) in 2019 by Doppler tomographic observation. I utilized this data from HIDES. I also analyzed Doppler tomographic data by High Dispersion Spectrograph (HDS) in 2011, and Robert G. Tull Coudé Spectrograph (TS23) in 2008, 2014, and 2016 to search the variations of its projected spin-orbit obliquity and its impact parameter. I also observed the hot Jupiter for adding data points of its impact parameters by Multicolor Simultaneous Camera for studying Atmospheres of Transiting exoplanets (MuSCAT) in 2017 and the second generation (MuSCAT2) in 2018. I calculated its real spin-orbit obliquity and J_2 by MCMC with the time variation models of the two orbital parameters. Then, I confirmed the more precise WASP-33b's nodal precession with more extended and more observations than the previous study. I obtained WASP-33b's real spin-orbit obliquity, $110^{+1.3}_{-1.4}$ deg. This planetary orbit has evolved with the mechanisms which makes the orbit misaligned easily such as the planet-planet scattering and the Kozai migration. This research is the first step to make a histogram of the real spin-orbit obliquity by Doppler tomography and transit photometry. I also found $J_2 = 1.11^{+0.15}_{-0.11} \times 10^{-4}$, which is slightly smaller than the calculated one in theory. This may indicate the possibility that its actual stellar internal structure is different from the theoretical one. In the future, I will clarify how hot Jupiters have migrated by increasing the measured samples.

Acknowledgements

Many people supported this thesis. First, I would like to offer my special thanks to my advisers. My deepest appreciation goes to my main advisers, Dr. Norio Narita and Dr. Yasunori Hori. I am grateful for your support for this thesis, my research, and ways to write some documents and proposals. I thank Dr. Akihiko Fukui and Dr. Nobuhiko Kusakabe for helping with observations using MuSCAT and MuSCAT2. I would also like to express my gratitude to Dr. Marshall C. Johnson for teaching me how to analyze least-squares deconvolution, which is an essential part of Doppler tomography. It was a great experience when I studied in Ohio. Moreover, I owe gratitude for your advice about my research. I thank Dr. Enric Palle and Dr. Hannu Parviainen for discussing MuSCAT2 when I was in Tenerife.

Second, I would like to express the deepest appreciation to my same-year students, Hiroyuki Ishikawa, Satoshi Tanioka, Yoshiki Hatta, Masayuki Yamaguchi, and Jin Sai. Your talks about researches always made me excited, and I laughed at your funny and nonsensical jokes. I owe a very important debt to my friendly colleagues of MuSCAT members, Dr. John Livingstone, Dr. Kiyoe Kawauchi, Jerome de Leon, Yuka Terada, Taku Nishiumi, and Mayuko Mori. It was very beneficial to discuss the exoplanet with you. I also enjoyed drinking with you. I would also like to express my gratitude to Nuria Casasayas-Barris and Rafa Luque. I remember you taught me about analysis for transmission spectroscopy and transit photometry. You also made great memories when I stayed in Tenerife.

Finally, I want to thank my private friends and my family for supporting me during these five years.

I was grateful for SOKENDAI's budget supports. Thanks to their aids, I could go to study and to present my researches in foreign countries. These are also helpful for my observations for this research.

This thesis is based on data collected at the Subaru Telescope, which is located atop Maunakea and operated by the National Astronomical Observatory of Japan (NAOJ). We wish to recognize and acknowledge the very significant cultural role and reverence that the summit of Maunakea has always had within the indigenous

Hawaiian community. The thesis also includes data taken at The McDonald Observatory of The University of Texas at Austin and taken at The Okayama Astrophysical Observatory. Pyraf is a product of the Space Telescope Science Institute, which is operated by AURA for NASA. This work has made use of the VALD database, operated at Uppsala University, the Institute of Astronomy RAS in Moscow, and the University of Vienna.

Contents

List of Figures

List of Tables

Chapter 1

Introduction

1.1 Brief History of Exoplanet

Inhabitants on the Earth have struggled to probe extrasolar planets, also known as exoplanets, around other stars than the Sun since the middle of the 19th century. Jacob (1855) and See (1896) insisted that a dim target near the binary system, 70 Ophiuchi, was a planet, which Moulton (1899) rejected unluckily. After that, van de Kamp (1963) claimed a Jupiter-like giant planet around Barnard's Star adopting the astrometry method, validating a bit wobbling star due to planetary gravitation by imaging. This planet turned out to be systematic systematics, after all.

Before Kamp's claim, Struve (1952) declared that radial velocity (RV) observation with a high spectrograph could hunt an exoplanet by measuring the Doppler shift of a star vibrates due to planetary gravitation. Campbell et al. (1979) improved the radial velocity precision and observed 21 main-sequence and sub-giant stars for 12 years. However, Walker et al. (1995) revealed no detected planets around them. During the two dozen years, Latham et al. (1989) found an object more massive than 13 Jupiter mass (hereafter, I write this unit as M_J) orbiting around The star HD114762, which advanced the research of exploring exoplanets.

In the middle of the 1990s, Mayor et al. (1995) accomplished discovering an exoplanet around the main-sequence star, 51 Pegasi, for the first time. They detected this planet's mass 0.5 M_J and orbital period 4.2 days by the RV observation. These parameters describe a Jupiter-like planet exiting at closer orbit than the distance between the Sun and Mercury. This exoplanet, whose type is called "hot Jupiter" today, was so uncommon that it surprised human beings living in the Solar system. This

discovery overturned the usual formation theory for our Solar system.

After the discovery, the number of hot exoplanets increased gradually by the RV method and the transit method. Charbonneau et al. (2000) utilized the transit observation for the first time to validate the hot Jupiter HD 209458b. This method can find an exoplanet by photometry because it blocks the stellar disk partially during transiting in front of its host star. Since the beginning of 21 century, it has contributed for exoplanet exploration with the ground-based transit survey such as SuperWASP (Wide Angle Search for Planets; Collier Cameron et al., 2007), HATNet (Hungarian Automated Telescope Network; Bakos et al., 2002), KELT (Kilodegree Extremely Little Telescope; Pepper, Gould, and Depoy, 2004), and the space transit surveys such as CoRoT mission (Convection Rotation et Transits planètaires; Barge et al., 2005), NASA's Kepler mission (Borucki et al., 2010) and NASA's TESS mission (Transiting Exoplanet Survey Satellite; Ricker et al., 2016). They have found about 3,000 exoplanets; most of the number, around 2000 exoplanets, is a fruit of Kepler's mission. After all, the total number of confirmed exoplanets is more than 4200 in 2020 (see Figure 1.1).

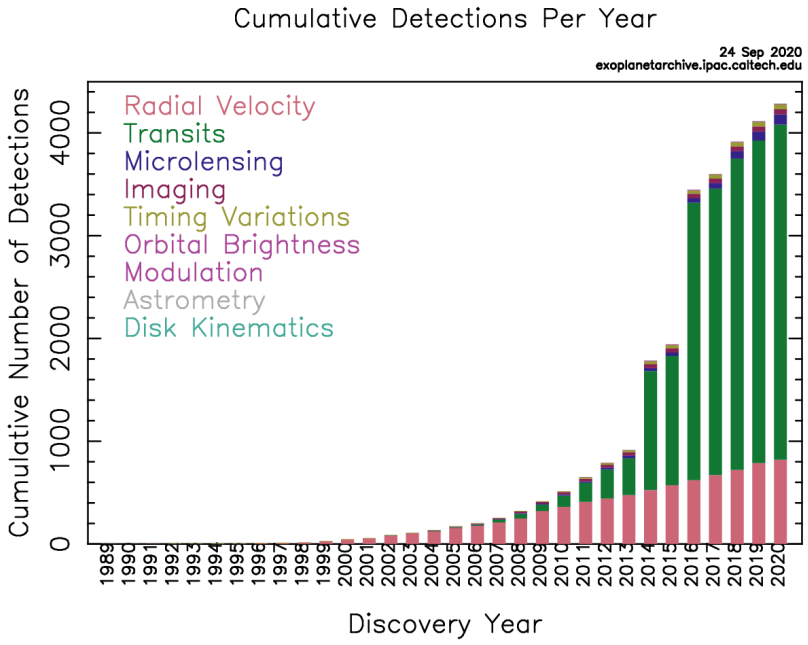

FIGURE 1.1: Bar chart of the total number of confirmed exoplanet every year. Each color corresponds each discovery method. (citing from https://exoplanetarchive.ipac.caltech.edu).

1.2 Orbital Evolution Models and Alignment

1.2.1 Classic Planet Formation Model: Core Accretion Model

Safronov (1972) and Hayashi, Nakazawa, and Nakagawa (1985) suggested that the core accretion model supports the formation of the solar system. A protoplanetary with $0.01 - 0.02$ solar mass ($M_\odot$) is created when a star is born. Next, dust components sink into the mid-plane of the disk and generate planetesimals. These planetesimals turn solid planets by colliding and combining each other. When the mass of a solid planet reaches more than 10 Earth-mass ($M_\oplus$), this planet accumulates gas promptly. It is easy to make a massive solid planet beyond the ice line ($>$ 2.7 AU in the Solar system) with abundant dust, including condensed ices. Then the massive solid planet turns to a gas giant planet. Thus, gas giant planets should exist in the distant region from the star. I display an illustration of this formation model in Figure 1.2. However, creating hot Jupiters in situ is challenging because ices cannot keep as solids the inner area. Therefore, another method to bring a gas giant planet near its host star was requisite. There are mainly three orbital evolution models for hot Jupiters.

1.2.2 Another Planet Formation Model: Gravitational Instability Model

Before I explain the orbital evolution models, I add a description of another planet formation model. Kuiper (1951) and Cameron (1978) argued the disk gravitational instability model for gas giant planets. This model can create gas giant planets in the outer area ($>$ 20 AU) by shrinking divided clumps of a protoplanetary disk, which implies that this planetary model cannot create hot Jupiters in situ. Self-gravitational instability occurs when

$$Q \equiv \frac{c_s \Omega_K}{\pi G \Sigma_g} < 1 \tag{1.1}$$

where Q is the Toomre stability parameter (Toomre, 1964), c_s is the sound speed, Ω_K is the angular velocity of a circular orbit, G is the constant of gravitation, and Σ_g is the gas surface density of the disk. Equation 1.1 is satisfied when the disk instability is symmetric, whereas $Q < 1.5 - 2.0$ when the instability is nonaxisymmetric.

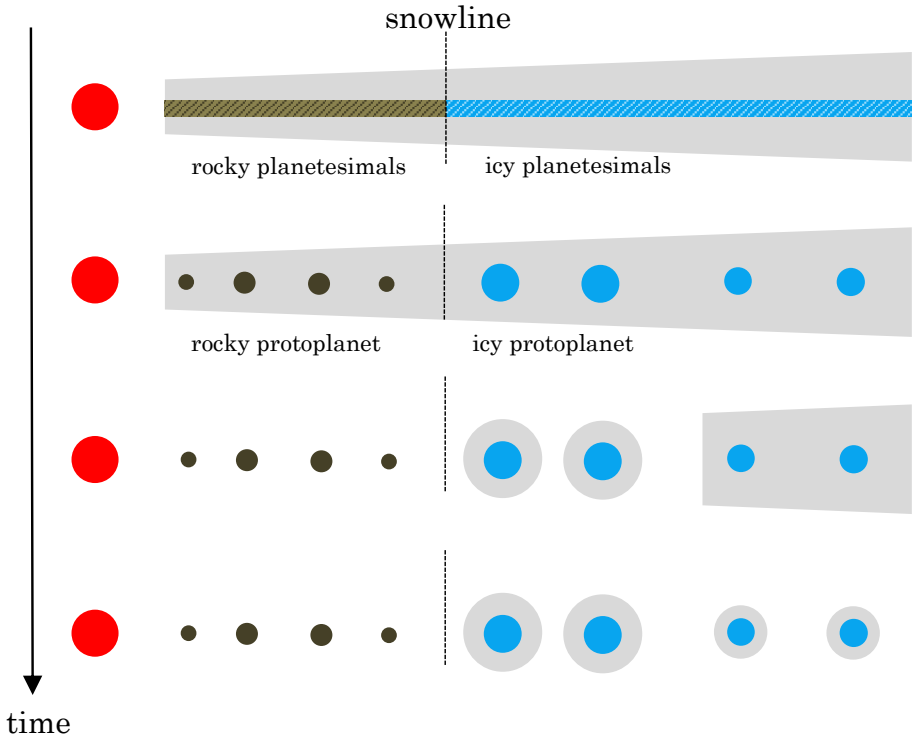

FIGURE 1.2: Illustration of classical planet formation process.

Following this method, gas planets should have almost the same metallicity as their host star. However, Jupiter's metallicity is higher than the solar one. Moreover, this model is not for the terrestrial planet formation, but for the gas planet formation. Therefore, the disk gravitational instability model had not been interesting to consider the solar system formation for several dozen years. After discovering exoplanets, this model has been reconsidered for the exoplanet formation (e.g., Boss, 1997) with orbital evolution. Recently, Galvagni and Mayer (2014) presented that the disk gravitational instability model can make hot Jupiters via planet-planet scattering, which I will explain in Subsection 1.2.4.

1.2.3 Planet-disk Interaction

When a protoplanetary disk remains after creating planets, a planet falls toward its host star by the interaction between the planet and the disk (Lin, Bodenheimer, and Richardson, 1996). Originally, Lin and Papaloizou (1986) suggested this process though it was not remarkable before the discovery of hot Jupiter. After a solid planet's mass gets above dozens of Earth masses, its gravity scatters gases around

its orbit and forms a gap because its Hills radius is larger than the disk thickness. As the viscous gas moves to the center of the disk by losing its angular momentum, the giant planet migrate toward the host star in the moving gap (Type II migration; Lin and Papaloizou, 1986, see Figure 1.3). This migration takes about $\sim 3 \times 10^5$ years when Jupiter mass planet is at 5AU in the classical method (Nelson et al., 2000). On the other hand, Ida et al. (2018) shows that Jupiter-mass planet at 3AU migrates for about several million years considering the turbulence in the disk; the time scale is longer when the disk turbulent is stronger.

In the case of a terrestrial planet, though it cannot construct a gap, the planet drops to its host star due to friction between the disk and the planet (Type I migration; Ward, 1986). After a planet followed this planet-disk interaction model, including type-I and type-II, its orbital momentum typically aligns with the stellar spin axis. Then the orbit keeps circular.

However, some disk conditions can lean disks and make misaligned orbits with the inclined disks. First, we have to consider that variable accretion and interactions between stars can slant a protoplanetary disk in a stellar cluster from a turbulent molecular cloud (Bate, Lodato, and Pringle, 2010). Warped strong magnetic field from a host star with larger than several kG is also one of the causes to make misaligned disks (Lai, Foucart, and Lin, 2011), but the misaligned orbits due to the strong magnetic fields hardly seem to occur because the young stars tend to have about $< 1kG$ magnetic fields (Bouvier et al., 2007).

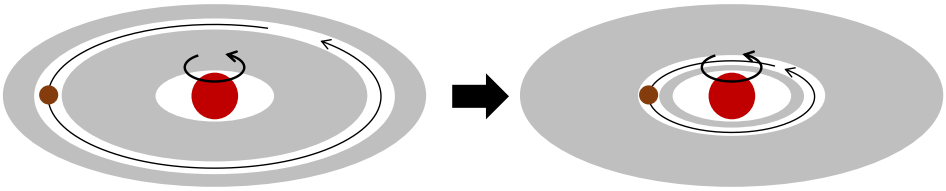

FIGURE 1.3: Illustration of type II migration.

During the planet-disk migration, the orbit always aligns with the disk. Thus, To check the orbital evolution from the distribution of the measured spin-orbit obliquity ϕ, the angle between the stellar rotation axis and the orbital angular momentum vector, we can compare them with the simulated distribution. Lai, Foucart, and Lin,

2011 calculated the distribution with the magnetic torque even though the disks with weak magnetic torque are the majority (see Figure 1.4).

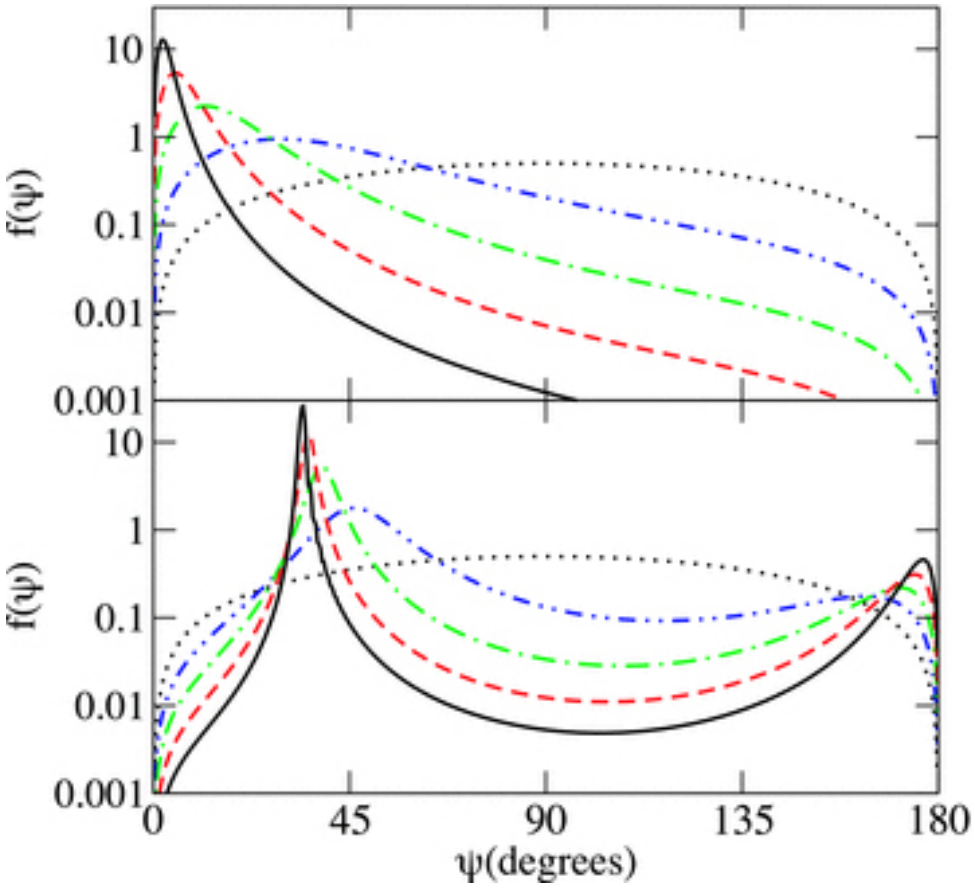

FIGURE 1.4: Obliquity histogram of the disk via planet-disk interaction when the magnetic torque is weak (upper figure) or strong (bottom figure) from Lai, Foucart, and Lin (2011). The horizontal line is the spin-orbit obliquity, and the vertical line is the frequency. The solid black line shows the initial distribution. This distribution changes into blue line, green line, then red line. Finally, it settles as a black solid line.

1.2.4 Planet-planet Scattering

We consider three gas giant planets to be orbiting close to each other after the gas disk has gone. Although they have continued circular orbit for 10 Myrs, gravitational scattering occurs suddenly so that their eccentricities and inclinations change randomly (see Figure 1.5). Rasio and Ford (1996) proposed this mechanism initially after the discovery of Peg. 51b. Then Chatterjee et al. (2008) explained the reason for the existence of misaligned or eccentric planets by the scattering model. Depending

on the scattering situation, some planets get flipped far away from their systems; they never orbit around their host star.

If the distance between the periapsis and the star is very close ($\leq$ 10 stellar radius (R_s): 0.05 AU for the Sun), the orbit approaches toward the star holding the periapsis. The planet changes its shape near the point. This dynamic tide decreases the planet's kinematic energy and its semi-major axis (Jackson, Greenberg, and Barnes, 2008 and Nagasawa, Ida, and Bessho, 2008). Therefore, this tidal evolution brings a hot Jupiter with a misaligned orbit.

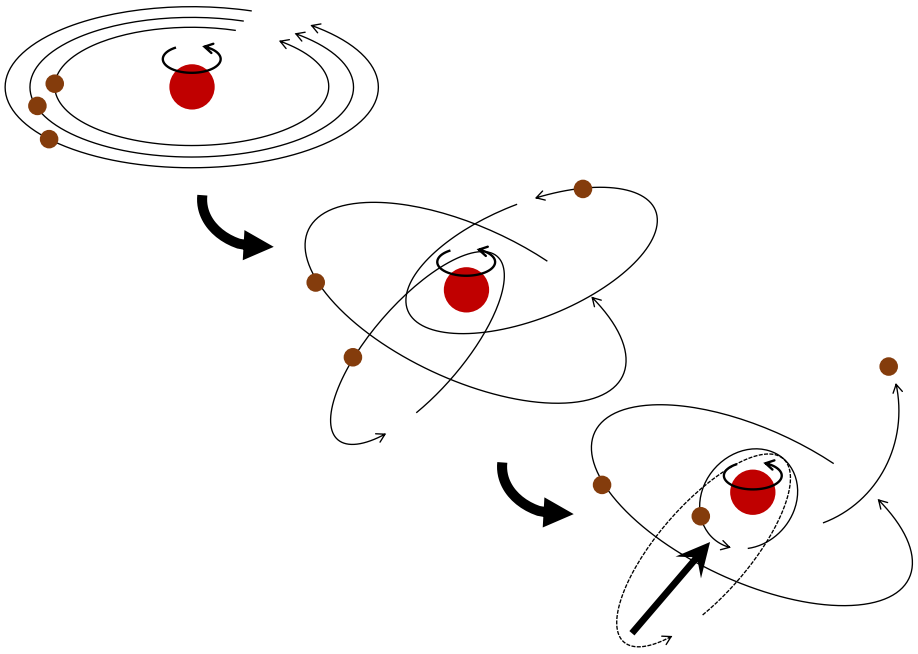

FIGURE 1.5: Illustration of planet-planet scattering.

Nagasawa and Ida (2011) simulated the planet-planet scattering creating samples of the system with three giant planets with the dynamical tide formulae from Ivanov and Papaloizou (2007). This simulation displays the distribution of the spin-orbit obliquity ϕ, the angle between the stellar rotation axis and the orbital angular momentum vector, in Figure 1.6. Following this histogram, it is easy to create misaligned prograde planets (30 deg $< \phi <$ 90 deg), but there are 28% retrograde planet samples.

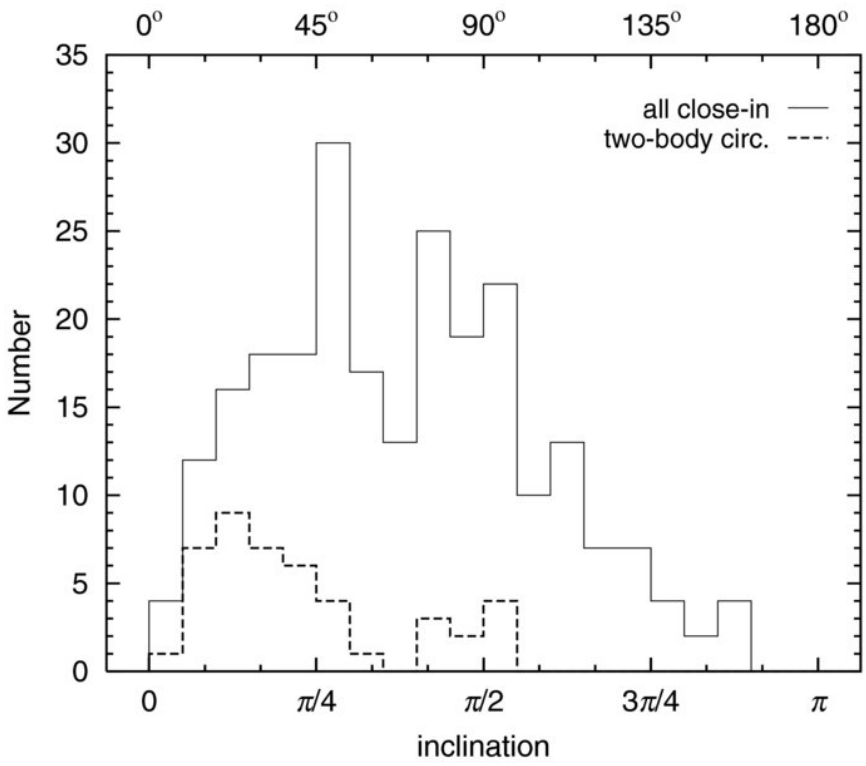

FIGURE 1.6: Obliquity histogram via planet-planet scattering from the samples of Nagasawa and Ida (2011), which expresses obliquity as inclination. The solid line shows the distribution of all close-in planets, while the dotted line is one of the planets whose systems have lost one or two planets by scattering. In this simulation, they set the migration time 10^8 years.

1.2.5 Kozai Migration

The gravitational perturbation of a massive giant planet or a companion star shakes an inner planet when their orbital planes are inclined to each other. Inner planet's eccentricity and mutual inclination continue to oscillate so that z' component, the direction of the node of the comparison star's orbit plane, of the inner planet's angular momentum L keeps preserved; HD80606b, a highly eccentric ($e = 0.93$) giant planet whose system has a companion star, has oscillated with a 20-Myr-period swing for 0.1 Gyrs (Wu and Murray, 2003) for instance (Equation 1.2; Kozai, 1962).

$$L = m_p \sqrt{GM_s a(1 - e^2)} \cos I \tag{1.2}$$

where m_p, a, e are respectively the mass, the semi-major axis and the eccentricity of the inner planet, and G, M_s, I are the constant of gravitation, the host star's mass, and mutual inclination respectively. Thus, when the inner planet's orbital plane goes closer to the outer one, the eccentricity becomes high. When $I > 39.2$ deg, this vibration is striking. This phenomenon is called the Kozai-Lidov mechanism (see Figure 1.7). Kozai (1962) and Lidov (1962) proposed this theory for the orbital evolution of asteroids by Jupiter's gravitational perturbation originally. This mechanism is also another cause of the occurrence of misaligned planets. Wu and Murray (2003) and Fabrycky and Tremaine (2007) showed that highly eccentric planet due to the Kozai-Lidov mechanism undergoes the tidal decay. This whole orbital changing process is called Kozai migration. Hence this is also one of the origins of misaligned hot Jupiters.

Fabrycky and Tremaine (2007) simulated the Kozai migration and showed the obliquity distribution. They set the companion stellar orbit as a circular orbit with a semi-major axis of 500 AU. The distribution is different from that via planet-planet scattering. Half samples are aligned (< 30 deg), while the other half are misaligned from 30 deg to 140 deg. Petrovich (2015) considered with the various values of companion stars' semi-major axes and eccentricities. Then the simulation resulted in the obliquity distribution as shown in Figure 1.8. The distribution is roughly flat from 10 deg to $\sim$ 140 deg and the range is wider than the result via planet-planet scattering simulation by Nagasawa and Ida (2011) (Figure 1.6) (see text).

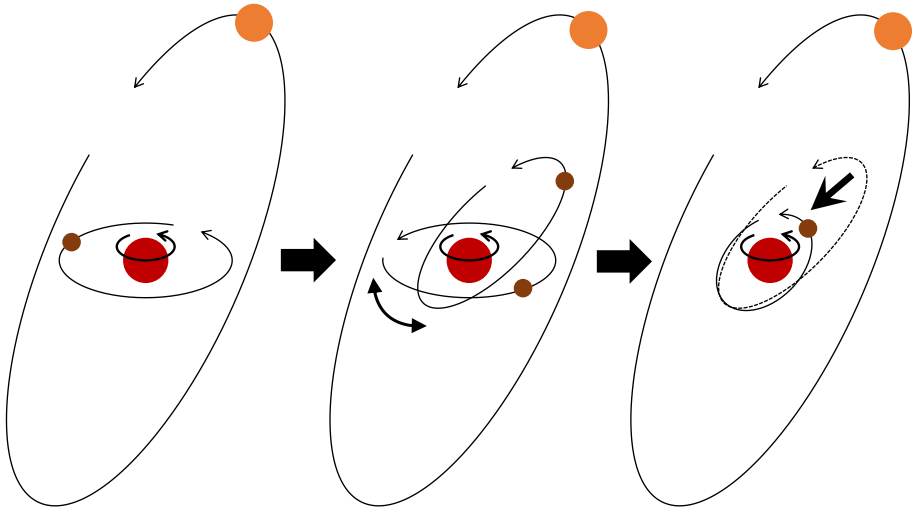

FIGURE 1.7: Illustration of Kozai Migration. The orbital oscillation in the middle figure shows Kozai-Lidov mechanism.

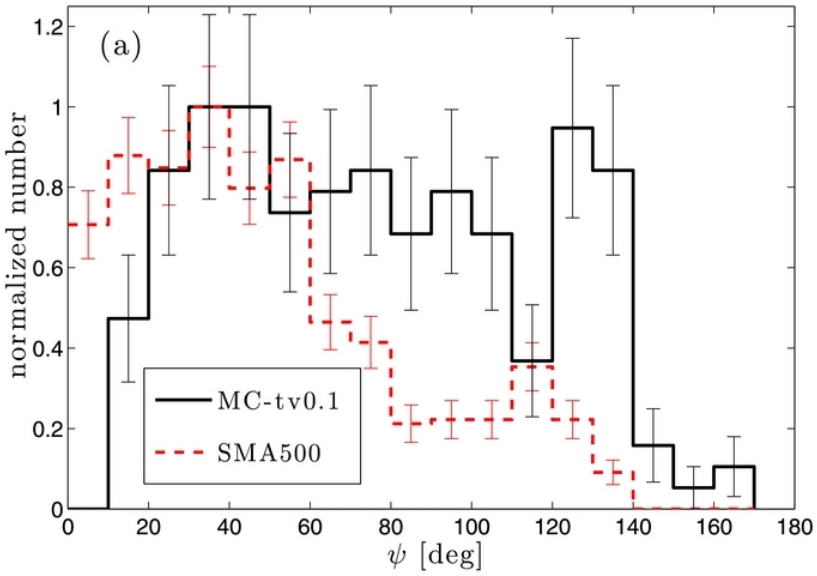

FIGURE 1.8: Obliquity histogram via Kozai migration from Petrovich (2015). The black solid line shows the distribution of hot Jupiters' obliquities. The red dotted line shows the distribution simulated with the condition of Fabrycky and Tremaine (2007).

1.3 How to Measure Spin-Orbit Obliquity

As shown in Section 1.2, an orbit stays aligned with the stellar spin in the gas disk migration model generally, while the other models tend to make one misaligned easily. For this reason, the spin-orbit obliquity ϕ, the angle between the stellar rotation axis and the orbital angular momentum vector, is the key to investigate which orbital evolution the planet has followed ; the angle between the solar spin axis and the Earth's orbital momentum vector is $\phi \sim 7$ deg (Beck and Giles, 2005) as a reference. However, Rossiter-McLaughlin measurement and Doppler tomography, which are the main techniques and showed in this Section, can only measure "projected" spin-orbit obliquity λ (See Figure 1.9).

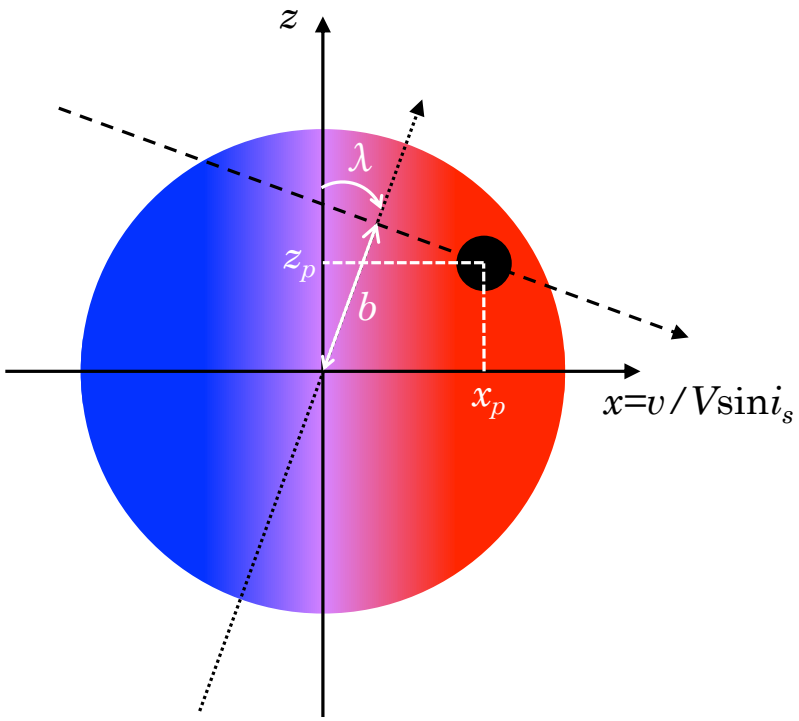

FIGURE 1.9: Illustration of a planet crossing its stellar disk from an observer. The dashed line shows orbit, and the dotted line is the orbital momentum vector. I set the projected direction of the stellar spin axis as z axis. z is normalized by stellar radius R_s. When we adopt the assumption that the stellar spin axis is parallel to the night sky and the star is rigid, the velocity in the line profile standardized by $V \sin i_s$ correspond to the position of x divided by stellar radius R_s. Here I note that v is the radial velocity at the position of x. The blue side and the red side represent the approaching semicircle and the receding semicircle, respectively. b, x_p, and z_p is the impact parameter and the planet's position in the coordinate (x, z).

1.3.1 Rossiter-McLaughlin Effect

The Rossiter-McLaughlin effect (RM effect) means a phenomenon that the apparent radial velocity shifts because eclipsing binary blocks the stellar surface of one of them (Rossiter, 1924 and McLaughlin, 1924). The same phenomenon occurs when a planet transit in front of its host star. Queloz et al. (2000) adopted this method for the spectroscopic transit observation of HD209485b and measured its projected spin-orbit obliquity.

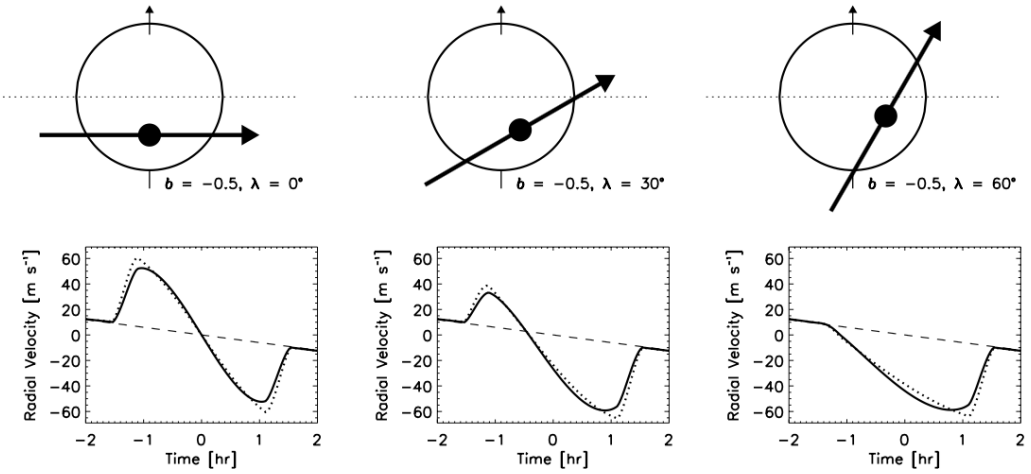

FIGURE 1.10: Apparent radial velocity changes during transit by Rossiter-McLaughlin effect. the behave of the change is different from λ and b. This figure is cited from Gaudi and Winn (2007).

A star generates an approaching side and a receding side on the stellar disk by rotating. Observers detect it as if the star was receding when a planet covers on the approaching side. On the other hand, they can observe as if the star was approaching when a planet blocks on the receding side. We can measure the projected obliquity from the change of the apparent radial velocity during planet transit. It can also measure the impact parameter b, the apparent distance scaled by the stellar radius from the center of the stellar disk to the transit trajectory.

We can measure the apparent radial velocity from the shifted peak of the stellar line profile when the apparent stellar velocity $V \sin i_s$ is similar to FWHM of the proper stellar line-profile W_p ($\sim$ 5 km s^{-1}), derived from the thermal broadening and the uncertainty principle. However, when $V \sin i_s$ is much larger than W_p, the stellar line profile broadens, and the bump called "planetary shadow" appears in the

profile. Thus, reading the shift of the peak comes to be hard.

1.3.2 Doppler Tomography

Doppler tomography can visualize the planetary shadow by subtracting a line profile during in-transit from one during out-of-transit. I show the model of Doppler tomography in Figure 1.12. It can trace only planetary shadow even though stellar activities such as starspots and pulsations occur on a stellar surface, which warps its stellar line-profile and arises systematic errors by RM measurement (Brown et al., 2012). We can measure λ and b by this method as well as by the RM method (Figure 1.13 and Figure 1.14).

This method was initially used to observe starspots blocking the stellar surface initially (e.g., Rice, 2002). Collier Cameron et al. (2010a) attempted the technique for the first time to measure the projected obliquity of HD18973b by a spectrograph with high resolution (R $\sim 100,000$) though its host star spins slow ($V \sin i_s < 5$ km s^{-1}). Just after the research, Collier Cameron et al. (2010b) validated a hot Jupiter, WASP-33b, around a rapid rotation star ($V \sin i_s \gg 5$ km s^{-1}) by Doppler tomography for the first time. They argued that the method could help to confirm a planet around a rapid rotation star. When the stellar rotation speed is about 100 km s^{-1}, spectral resolution $R > 30000$ is required to detect a shadow of a Jupiter-size planet.

1.3.3 Other Techniques

There are not only these two main methods but also other techniques to measure the spin-orbit measurements. One of them is gravity-darkened transit photometry. A rapid rotation star makes itself oblate, its poles brighter, and its equator darker. Thus, the intensity distribution of the stellar disk depends on the stellar latitude. Hence, this method can measure the spin-orbit obliquity ϕ by photometric transit observation (e.g., Barnes, 2009). However, because stellar activities cause the light curve warped, the systematic error is larger when the host star is active.

The starspots bother the RM and gravity darkening observation, but they are also useful to measure ϕ by counting the frequency that a planet crosses a spot. When a planet is in front of a starspot, the apparent flux is slightly brighter for a short

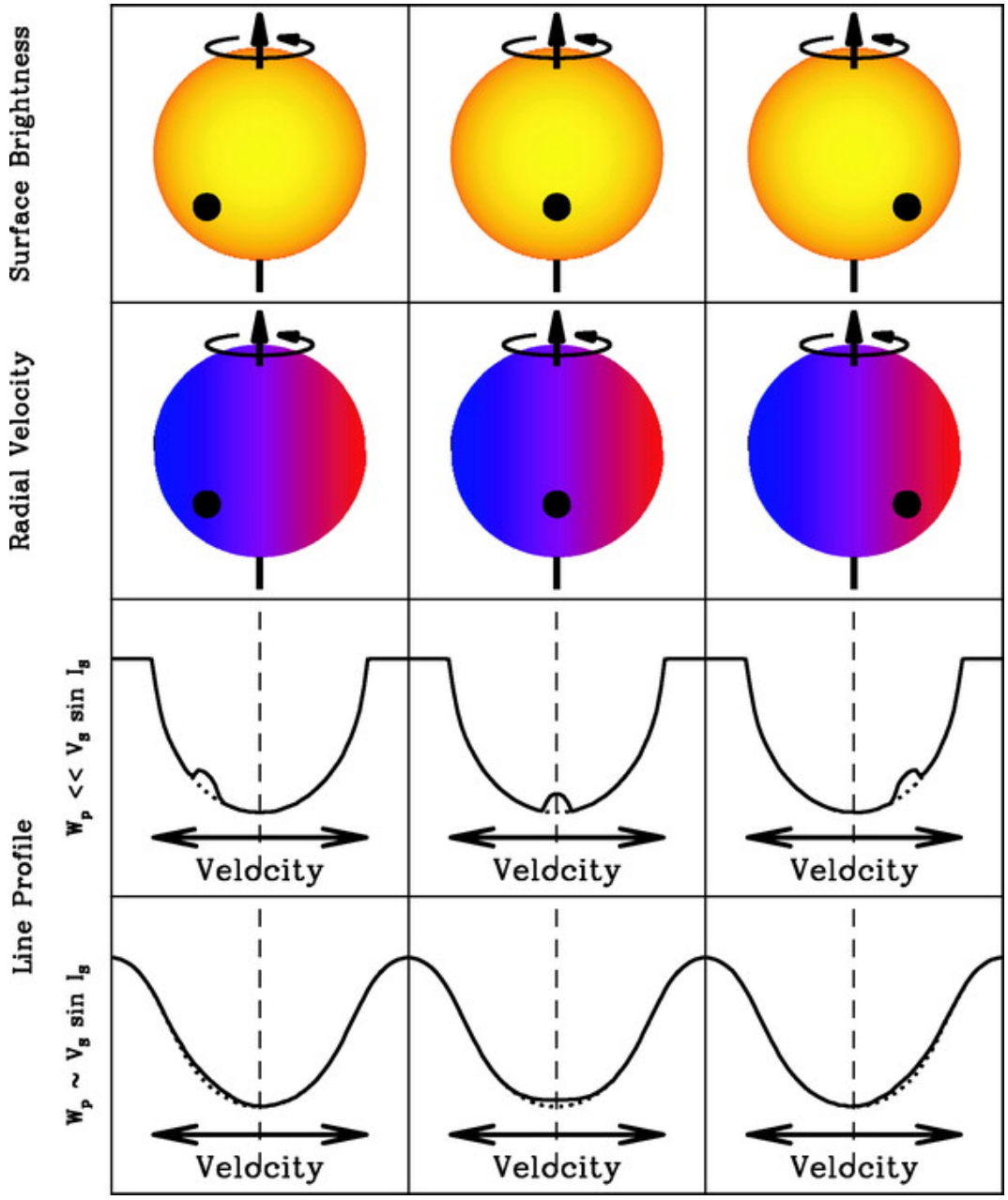

FIGURE 1.11: First row: Illustration of intensity distribution. Second row: Illustration of radial velocity distribution. Third row: Line profile during transit when $V \sin i_s \gg W_p$. Fourth row: Line profile during transit when $V \sin i_s \sim W_p$. In this figure, these line profiles show downward. This figure is cited from Gaudi and Winn (2007).

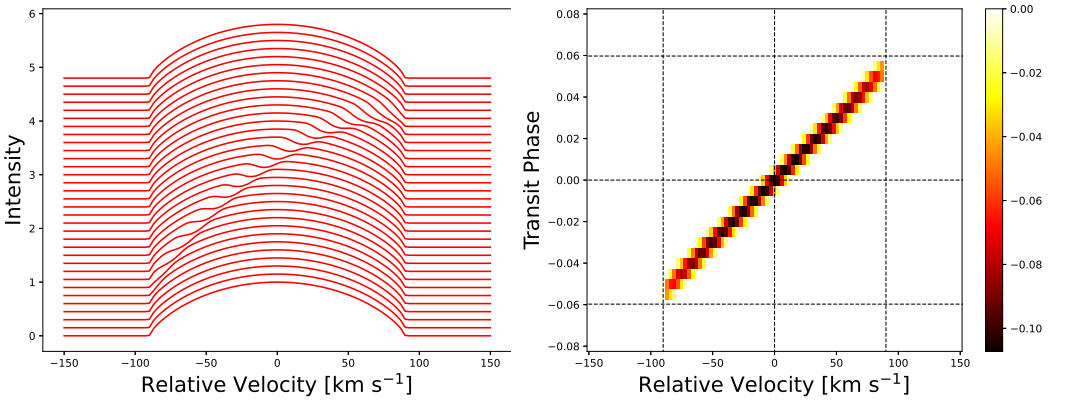

FIGURE 1.12: Left: Model of stellar line profile during transit when a stellar spin velocity is fast. The horizontal line and the vertical line are the relative velocity of the profile and the intensity, respectively. The stellar line profile changes from bottom to top. During the transit, planetary shadow shows in the line profile. In this figure, I set parameters $\lambda = 0$ deg, $b = 0$, $R_p/R_s = 0.1$, $a/R_s = 3.0$ and $V \sin i_s = 90$ km s^{-1}, Right: Model of planetary shadow . The horizontal line and the vertical line show the relative velocity and the time passing from bottom to top, respectively. A track of the planetary shadow appears as a dark part. Lower, middle and upper horizontal dotted lines are ingress, transit-middle and egress time. Left and right vertical dotted lines indicates the stellar rotational velocity.

time during transit. Unless the stellar axis is parallel to the line of sight, starspots move horizontally. Thus, the frequency is higher when the orbit is more aligned. Sanchis-Ojeda and Winn (2011) used this method first to observe HAT-P-11b.

1.4 Tendency of Orbital Obliquity

1.4.1 Hot Jupiters

Mainly, RM measurement and Doppler tomography have succeeded in measuring the projected obliquities of 110 hot Jupiters. Here I define hot Jupiter as planets with $0.5M_J < M_p < 13M_J$, $R_p > 0.8R_J$ and $P_{\rm orb} < 10$ days. I show the distribution between the host star's effective temperature and the projected misalignment in Figure 1.15. Winn et al. (2010) noticed the pattern that orbits of hot Jupiters around stars with $T_{\rm eff} < 6250$ K tend to be aligned with the stellar spin, whereas stars with $T_{\rm eff} > 6250$ K are apt to have a planet with misaligned orbit. When $T_{\rm eff} < 6250$ K, The host star has a thick convective zone in the surface layer. On the other hand, when the stellar effective temperature is beyond 6250 K, the hotter star contains thinner convective layer in its surface layer. Tidal dissipation occurs in the convective zone

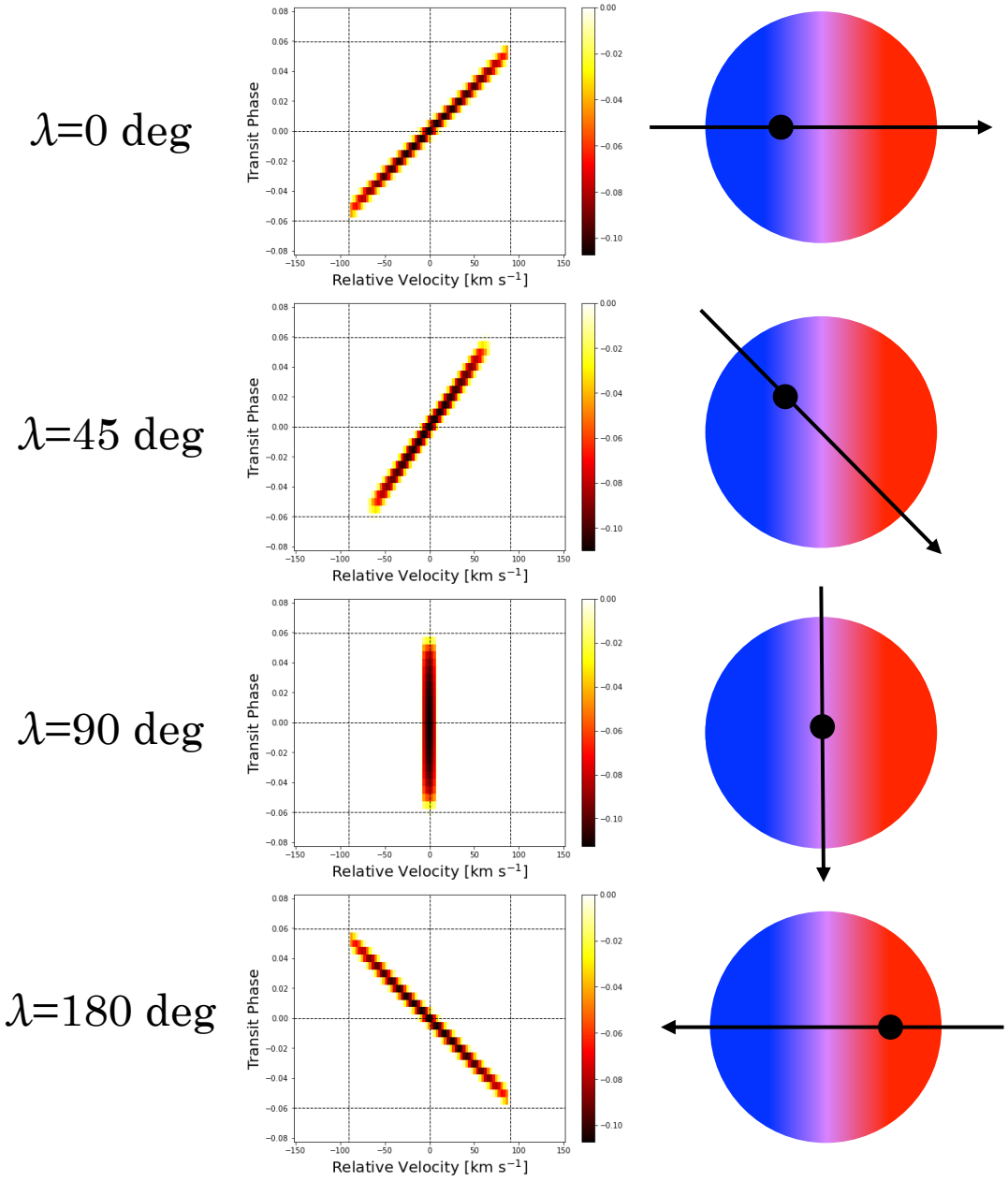

FIGURE 1.13: The setting parameters are the same as Figure 1.12 but $\lambda = 0$ deg, $\lambda = 45$ deg, $\lambda = 90$ deg, $\lambda = 180$ deg from top to bottom.

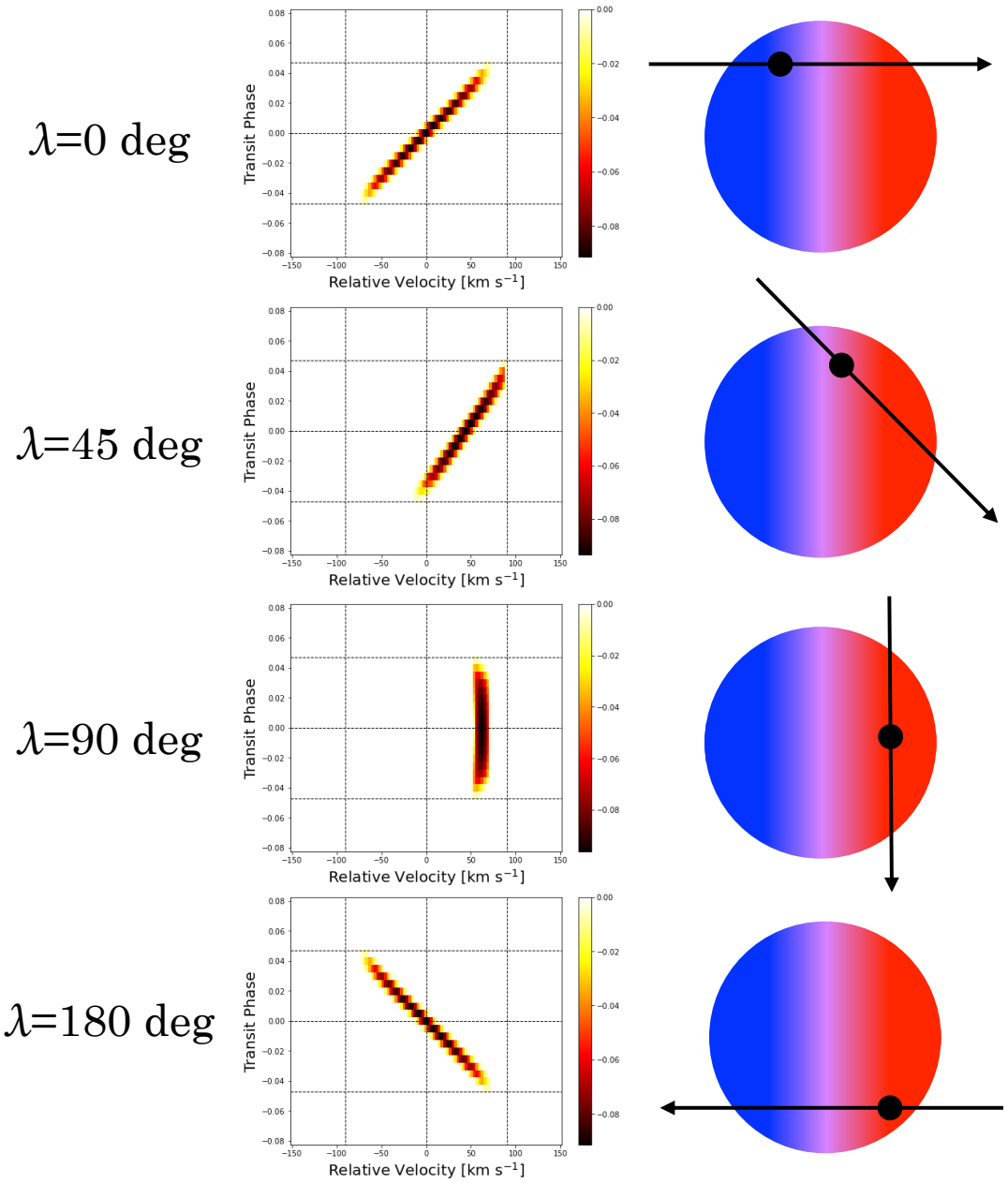

FIGURE 1.14: The same type as Figure 1.13 but $b = 0.7$.

of the star that has high viscosity. Then, tidal torque with the transformed planet occurs to realign more easily and quickly than one of the inner radiative zones with little viscosity, (Zahn, 1977 and Lai, 2012). Albrecht et al. (2012) explained the spin-orbit obliquity trend by the timescale of tidal dissipation from the Zahn's method with more samples than Winn et al. (2010).

There are 15 hot Jupiters around stars with $T_{\rm eff} > 7000$ K in Figure 1.15, which is classified as A- or B- type stars. Despite the small number, they tend to have a wide range of projected spin-orbit obliquities (Martínez et al., 2020). Cantiello and Braithwaite, 2019 indicated that A- or B-type stars almost have radiative structure, whose proportion is greater than ones with $T_{\rm eff} < 7000$. Therefore, the orbital evolution information should remain because the hot Jupiter's orbit can hardly lean its hot star with the full radiative zone. Here I note that while the system of HAT-P-57b is also categorized as a hot Jupiters around a hot star, its plot does not exist in Figure 1.15 because Hartman et al. (2015) could not decide the value of the projected obliquity uniquely. They measured it -16.7 deg $< \lambda <$ 3.3 deg or 27.6 deg $< \lambda <$ 57.4 deg.

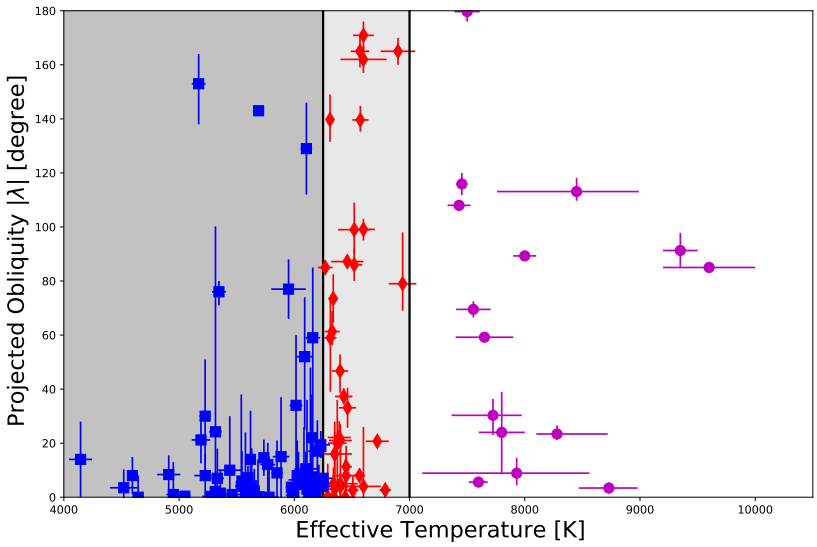

FIGURE 1.15: A current state of distribution between the host star's effective temperature and the hot Jupiter's projected orbital obliquity. Blue square dots in the grayest area, red rhombus dots in the fainter gray area and magenta circular dots in the white area correspond hot Jupiters around stars with $T_{\rm eff} < 6250$ K, 6250 K$< T_{\rm eff} < 7000$ K and $T_{\rm eff} > 7000$ K, respectively. I refered the existence of their companions from https://exoplanetarchive.ipac.caltech.edu.

As I explained in Subsection 1.2.4 and Subsection 1.2.5, hot Jupiter with a stellar companion or one or more planets has a possibility of misaligned orbit. As shown in Figure 1.16, some systems with misaligned hot Jupiters have their stellar companions, which indicates the possibility that Kozai migration has worked. There are the other misaligned hot Jupiters with no detected companions; undetected stellar or planet companions may exist. Moreover, there are few samples with confirmed planet companions: most of their orbits are aligned.

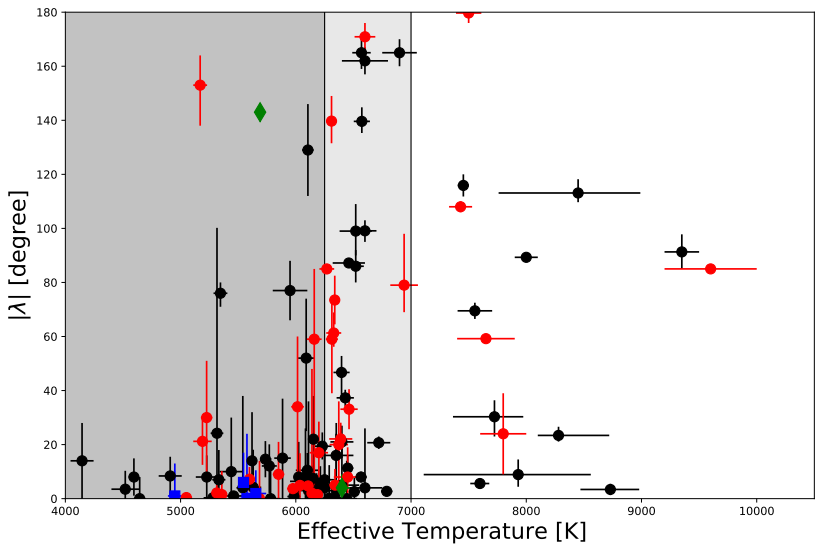

FIGURE 1.16: Similar to Figure 1.15, but colored plots whether the system has any comparison or not. Black circles, red circles, blue squares and green rhombus are the systems with no detected companions, a stellar companion, one or more planetary companions and both types of comparisons, respectively.

To consider the orbital evolution, we have to be aware of not only the obliquity but also the eccentricity. According to Figure 1.17, there are only five eccentric ($e > 0.1$) hot Jupiters whose obliquities are constrained well; two of them revolve with aligned orbits (HAT-P-2b ($e = 0.501 \pm 0.007$): Winn et al., 2007, and HAT-P-34b ($e = 0.441 \pm 0.032$) : Bakos et al., 2012). These two eccentric aligned planets may have undergone planet-planet scattering or Kozai migration, but there are no detected companions in these two planetary systems yet. Queloz et al. (2010) measured WASP-8b's high spin-orbit obliquity and high eccentricity. This planet may have undergone the planet-planet scattering or the Kozai-Lidov mechanism because

this planetary system has another planet and a stellar companion. HAT-P-14b is also an eccentric and misaligned-orbiting hot Jupiter (Winn et al., 2011) because of its stellar comparison whose presence is not confirmed yet (Knutson et al., 2014). The other misaligned eccentric hot Jupiter is XO-3b (Hirano et al., 2011), but no one has detected any companions to make this planet scattered yet.

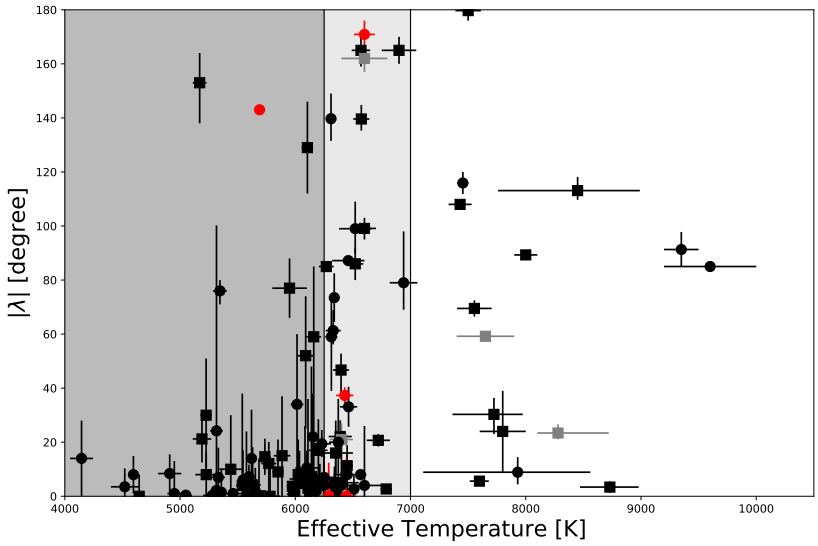

FIGURE 1.17: Similar to Figure 1.15 with eccentricity. Red circular dots are the eccentric hot Jupiters ($e > 0.1$). Black circular dots are the circular orbiting planets ($e < 0.1$). Black square dots are the circular orbiting planets with no eccentricities' errors. Grey square dots show the planets whose eccentricities are not measured.

As a side note, despite the fewer number than one of the hot Jupiters around hot stars, there are about 25 measured hot Saturns. They are lighter gas giant short-orbiting planet and I define them as planets having $M_p < 0.5M_J$, $R_p > 0.8R_J$. I show the projected obliquity distribution of hot Saturns in Figure 1.18.

For the present, most of the measured hot Saturns are around solar-like stars. Their orbits tend to be misaligned comparing with the trend of hot Jupiters around solar-like stars in Figure 1.15. This is because that the realignment time scale is in inverse proportion to M_p^2 (Barker and Ogilvie, 2009). This relation of the inverse proportion can also explain that the massive planets (>$3M_j$) tend to be aligned by the tidal realignment (Hébrard et al., 2011). I plot a distribution between the projected orbital obliquity and the planet mass in Figure 1.19.

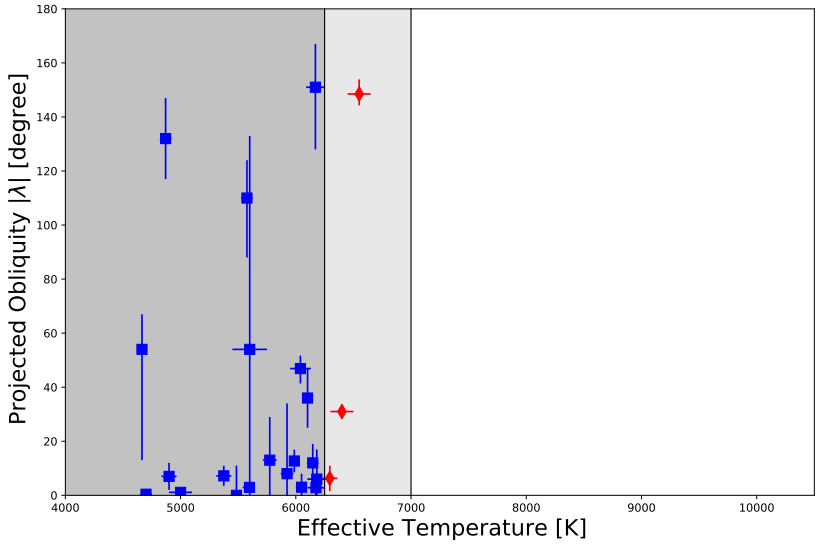

FIGURE 1.18: Same as 1.15, but for hot Saturns ($M_p < 0.5M_J$, $R_p > 0.8R_J$, $P_{\rm orb} > 10$ days).

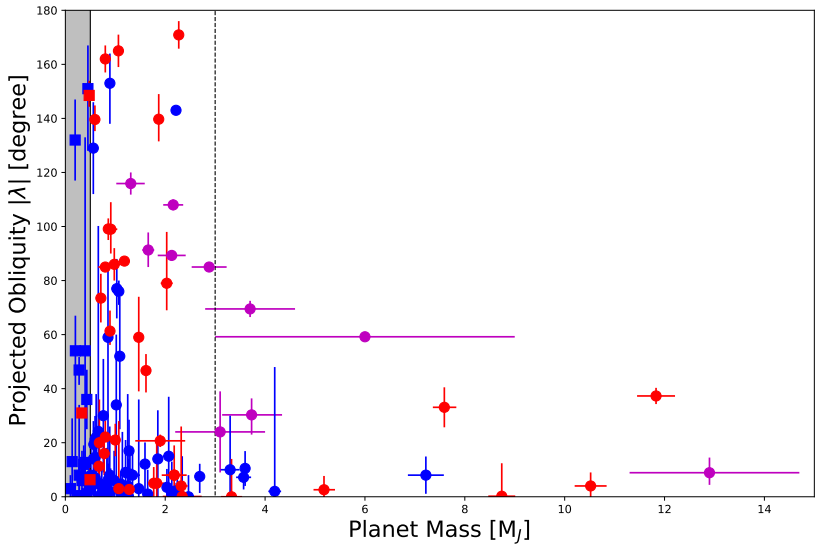

FIGURE 1.19: Distribution between λ and planet mass of hot Jupiters and hot Saturns. Circular dots in the white area are the hot Jupiters, while square dots in the grey area show the hot Saturn. Blue dots, red dots and magenta circular dots correspond short-period gas giant planets with $T_{\rm eff} < 6250$ K, 6250 K$< T_{\rm eff} <$ 7000 K and $T_{\rm eff} > 7000$ K, respectively. The vertical line at $M_p = 3M_J$ is the mass boundary for the realignment defined by Hébrard et al. (2011).

1.4.2 Other Planets

Not only hot Jupiters' spin-orbit obliquities, but also six warm Jupiters' ones ($0.5M_J < M_p < 13M_J$, $R_p > 0.8R_J$, $P_{\rm orb} > 10$ days) have been measured (see Figure 1.20). However, the few number cannot argue their tendency in detail. I note that Kepler-420b (Santerne et al., 2014) and HD 80606b (Hébrard et al., 2010) have a companion star and their spin-orbit obliquities are misaligned ($\lambda > 30$ deg).

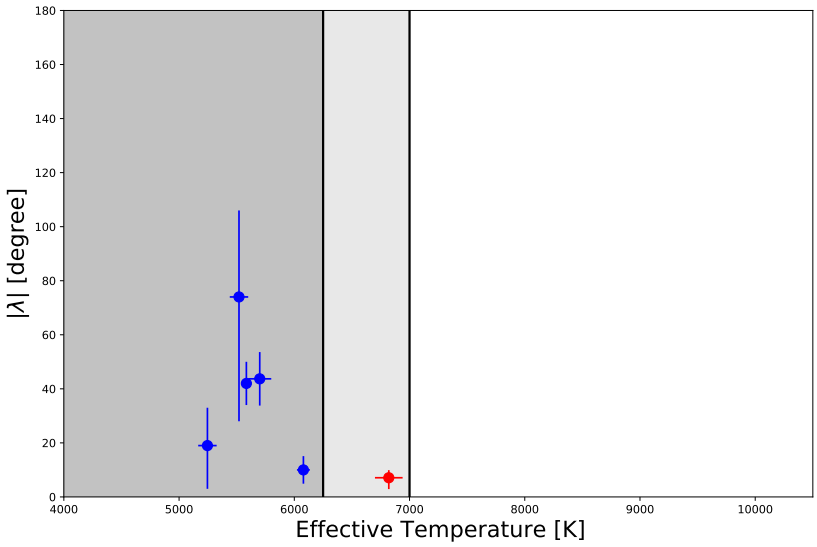

FIGURE 1.20: Same as 1.16, but for warm Jupiters ($0.5M_J < M_p < 13M_J$, $R_p > 0.8R_J$, $P_{\rm orb} > 10$ days).

I also show the trend of small planets ($R_p < 0.5\ R_J$) in Figure 1.22. The three plots at the lowest $T_{\rm eff}$ is three terrestrial planets around TRAPPIST-1, and their obliquities are not strongly misaligned (Hirano et al., 2020). Small planets with aligned orbit may follow the scenario that the stellar spin's torque aligns the inclined orbital momentum vector with the stellar spin axis (Spalding and Batygin, 2016). On the other hand, small planets with misaligned orbit may have experienced the gravitation scattering with outer Jupiter-like planets (Huang, Petrovich, and Deibert, 2017).

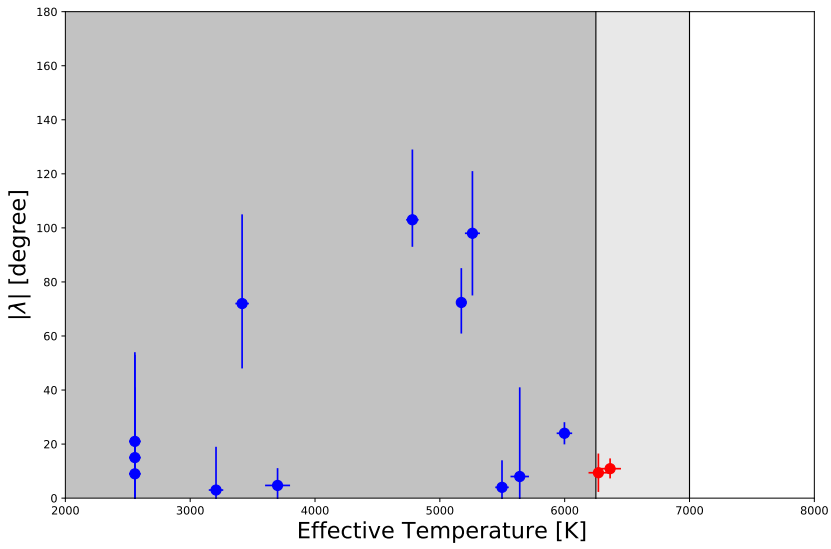

FIGURE 1.21: Same as 1.16, but for small planets ($R_p < 0.5\ R_J$).

1.5 Hot Jupiters around Hot Stars

1.5.1 History of Discovery

Discovery and confirmation of hot Jupiters around hot stars were difficult from an observation view. First, the Kepler space telescope, which has yielded a significant contribution to the exoplanet survey, was good at observation for distant stars. Conversely, this telescope's weak point is that bright stars, including hot stars, saturate its detector. Hot stars are not favorable for RV observation either because of few absorption lines. A hot star rotates faster than a Solar-type stars, namely F- G- K-stars (Gaige, 1993). Hence it is hard to read the RV shift by broadening and squashed absorption lines due to their fast rotation.

Though this difficulty, Collier Cameron et al. (2010b) found a hot Jupiter, WASP-33b, around an A-type star by Doppler tomography. Since this discovery, we recognize Doppler tomography as a method to measure the obliquity and to validate a planet around a hot star. This method revealed 16 confirmed hot Jupiters around hot stars at present (see Figure 1.15). Nowadays, most of the confirmed planets around hot stars are hot Jupiters and have undergone Doppler tomography. The others are outer gas giant planets found by imaging method (HR8799b, c, d, and e; Marois et

al., 2008). I note that all of these planets have circular orbits.

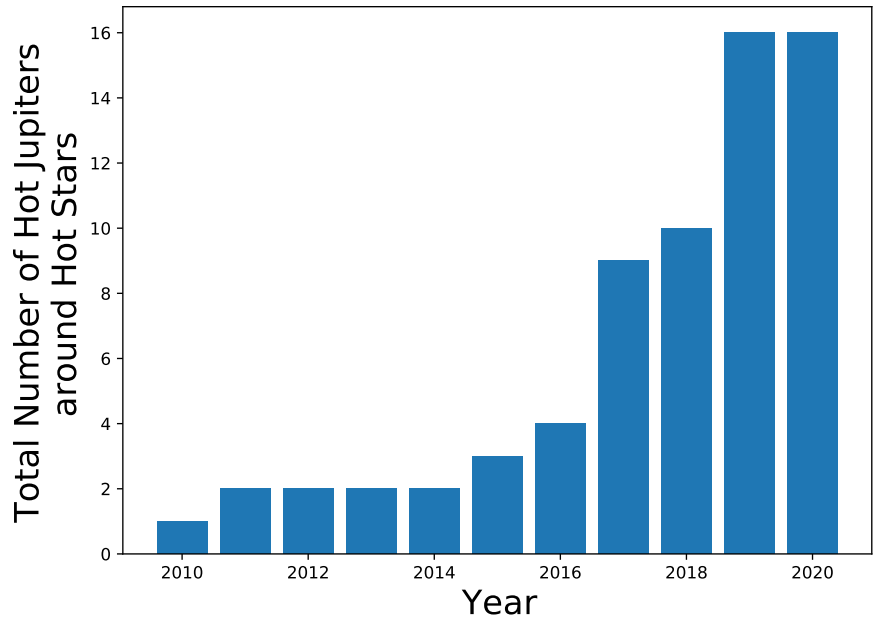

FIGURE 1.22: Bar chart of the total number of confirmed hot Jupiters around hot Stars every year since 2010.

1.5.2 Nodal Precession

Orbital nodal precession is a phenomenon that a planetary orbital momentum vector $\overrightarrow{L_p}$ rotates around the total angular momentum vector $\overrightarrow{L_t}$ ($\overrightarrow{L_t} = \overrightarrow{L_p} + \overrightarrow{L_s}$, $\overrightarrow{L_s}$ is the stellar spin angular momentum vector) by oblate host star (see Figure 1.23). Because hot stars are generally rapidly rotating (Gaige, 1993), their oblateness are larger than those of slowly rotating stars, which makes their orbital nodal precessions faster as Equation 1.3 from Barnes et al. (2013),

$$\dot{\theta} = \frac{3\pi J_2 R_s^2 \cos\phi \sin\phi}{P_{\rm orb} a^2 \sin\phi_p}, \tag{1.3}$$

where θ, J_2, R_s, ϕ, a, ϕ_p are the nodal angle, the stellar rotation-driven quadrupole moment, the stellar radius, the real angle between $\overrightarrow{L_s}$ and $\overrightarrow{L_p}$, the semi-majoer-axis, and the angle between $\overrightarrow{L_t}$ and $\overrightarrow{L_p}$, respectively. Figure 1.23 shows the angle information by illustration. A star with larger J_2 means its shape is more oblate. Iorio (2011)

estimated the nodal precession of WASP-33b with the speed $\dot{\theta} < 1.5$ deg year^{-1} and predicted it can be measured over a 10 years time span. Johnson et al. (2015) actually detected its precession for six years by two-epoch Doppler tomographic observations and calculated it $\dot{\theta} = 0.373$ deg year^{-1}. Iorio (2016) derived $\phi_{2008} = 99^{+5}_{-4}$ deg and $\phi_{2014} = 103^{+5}_{-4}$ deg from information of the nodal precession by Johnson et al. (2015). Masuda (2015) also detected the precession of Kepler-13Ab, which is also a hot Jupiter around an A-type star, by the four-year-transit observation with the Kepler space telescope.

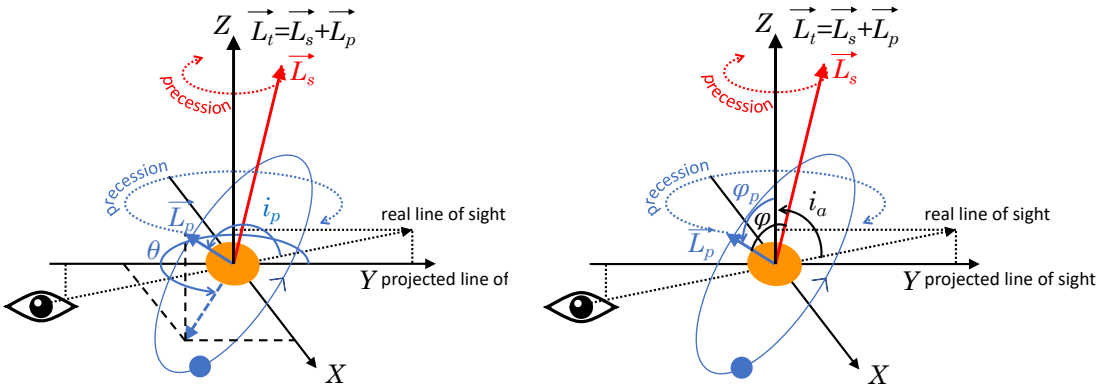

FIGURE 1.23: Illustration of the nodal precession. Left figure shows where θ and i_p is and right figure exhibits where ϕ, ϕ_p and i_a are

1.5.3 Nodal Precession and Observation

I demonstrate how this nodal precession affects the observation of a hot Jupiter around a hot star. Here I assume that the orbit is circular, and there are only two angular momenta, $\vec{L_p}$ and $\vec{L_s}$; I ignore the planetary rotational momentum. This assumption indicates the total angular momentum vector $\vec{L_t}$ is constant, and these three angular momenta are on the same plane. From Ragozzine and Wolf (2009) and Barnes et al. (2013), we can express J_2, ϕ_p, the ratio of $\vec{L_p}$ and $\vec{L_s}$ as

$$J_2 = \frac{k_2 R_s^3}{3a^3}\left(\frac{P_{\rm orb}^2}{P_{\rm spin}^2} + \frac{3m_p}{2M_s}\right) \tag{1.4}$$

$$\sin\phi_p = \frac{\sin\phi}{\sqrt{\frac{|\overrightarrow{L_p}|^2}{|\overrightarrow{L_s}|^2} + 2\frac{|\overrightarrow{L_p}|}{|\overrightarrow{L_s}|}\cos\phi}} \tag{1.5}$$

$$\frac{|\overrightarrow{L_p}|}{|\overrightarrow{L_s}|} = \frac{m_p P_{\rm spin} a^2}{C M_s P_{\rm orb} R_s^2}, \tag{1.6}$$

where k_2, $P_{\rm spin}$ and C mean Love number, the stellar spin period and the moment of inertial coefficient, respectively. We can write a as

$$a = \left(\frac{G M_s P_{\rm orb}^2}{4\pi^2}\right)^{\frac{1}{3}} \tag{1.7}$$

from the Kepler's third law. Then, I regard the stellar rotate velocity V as the observed rotate velocity $V\sin i_s$, which is projected velocity onto the line of sight. i_s is the angle between the line of sight and the stellar spin axis. This is because the distribution of measured V and the relations between measured $V\sin i_s$ and V are not obvious yet.

$$P_{\rm spin} = \frac{2\pi R_s}{V} \sim \frac{2\pi R_s}{V\sin i_s} \tag{1.8}$$

I make the formulation of the time change of impact parameter written as Equation 1.9 with the change of the nodal angle (Equation 1.10).

$$b(t) = \frac{a}{R_s}\left(\cos\phi_p\cos i_a + \cos\theta(t)\sin\phi_p\sin i_a\right) \tag{1.9}$$

$$\theta(t) = \dot{\theta}t + \theta_0 \tag{1.10}$$

where t is time, θ_0 is the initial value of θ and i_a is the angle between line of sight and $\overrightarrow{L_t}$.

As time passes, nodal precession will be able to stop a planet from transiting in front of its host star. To search the fraction of transiting hot Jupiters which will stop transiting in ten years, I make 100,000 models of the system with a hot Jupiter with a hot star to search their nodal precessions. This period corresponds to the observation period of the Kepler telescope. I adopt the numerical values of M_s, R_p, M_p, R_s, $P_{\rm orb}$ and $V\sin i_s$ randomly by the truncated normal distributions from the data of

confirmed hot Jupiters around A-type stars from TEPCaT (Southworth, 2011). I set the median and the dispersion of the observed values, the distribution's mean and dispersion, respectively. Then, I choose the numerical values of ϕ, i_a, θ_0 from the uniform distribution setting the ranges 0 deg $< \phi <$ 180 deg, 0deg $< i_a <$ 180 deg and 0 deg $< \theta_0 <$ 360 deg. I substitute C for 0.3 and k_2 for 0.03 from Iorio (2011). Then, I calculate $b(t = 0 \text{ years})$ and $b(t = 10 \text{ years})$ to count the number of hot Jupiters satisfied $|b(t = 0 \text{ years})| < 1$ and $|b(t = 10 \text{ years})| > 1$; which means transiting hot Jupiters will no longer cross in front of host stars after 10 years. I note that we can observe their transits when $b < 1$, otherwise we cannot.

I found that about 18,000 hot Jupiter models transit at $t = 0$ years and about 2,500 of them will stop transiting in front of host stars at $t = 10$ years. Figure 1.24 shows that hot Jupiters with any impact parameter have a ∼13% probability that their orbital trajectories will be out of their stellar disks. Thus, two of the confirmed 16 hot Jupiters around hot stars may not be available for transit observations after ten years.

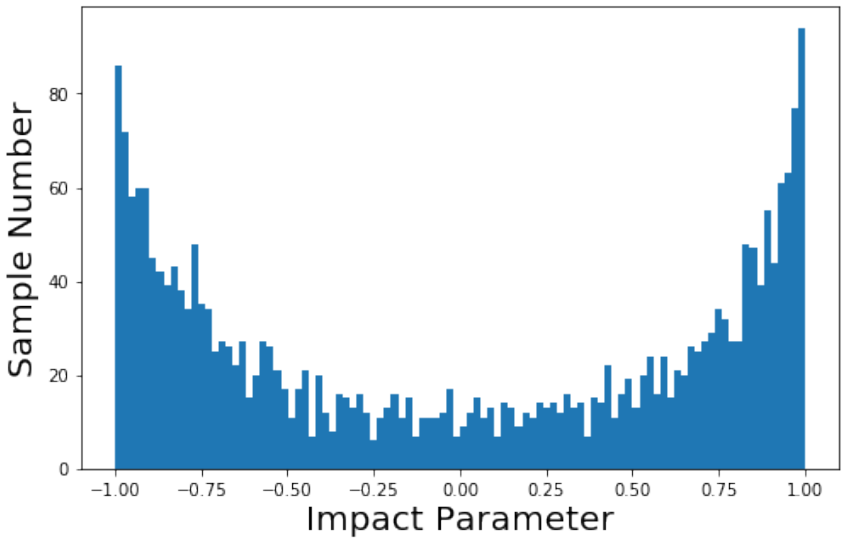

FIGURE 1.24: Histogram of initial impact parameter of transiting hot Jupiter samples which will no longer transit after 10 years.

1.6 Characteristic of WASP-33b

In this section, I briefly introduce the profile of WASP-33b, the target of my thesis. This planet was first validated with Doppler tomography by Collier Cameron et al. (2010b), who found it is a hot Jupiter orbiting in near-polar retrograde way around an A-type ($T_{\rm eff}$=7430$\pm$100 K) and rapidly-rotating ($V \sin i_s$ = 85.6 km s^{-1}) star. Doppler tomography is one method to measure spin-orbit obliquities and impact parameters simultaneously based on the apparent acceleration of a bump, sometimes referred to as a "planetary shadow," in the stellar line profiles during planetary transits. This planetary shadow appears in the line profile because a transiting planet hides a part of its stellar surface and removes spectral contributions to the line profile from the occulted part of the photosphere. Johnson et al. (2015) found that the transit chord of this planetary orbit had slightly changed in six years due to its nodal precession. They measured its projected obliquity $\lambda = -110.06^{+0.40}_{-0.47}$ deg and its impact parameter $b = 0.218^{+0.011}_{-0.029}$ from the spectral data in 2008, and $\lambda = -112.93^{+0.23}_{-0.21}$ deg and $b = 0.0860^{+0.0020}_{-0.0019}$ from the ones in 2014. They then calculated rates of change of these orbital parameters, $\mathrm{d}\lambda/\mathrm{d}t = -0.487^{+0.089}_{-0.076}$ deg yr^{-1} and $\mathrm{d}b/\mathrm{d}t = -0.0228^{+0.0050}_{-0.0018}$ yr^{-1}. From the results of Johnson et al. (2015), Iorio (2016) later measured the angle between the stellar spin axis and the line of sight $i_s = 142^{+10}_{-11}$ deg and the stellar gravitational quadrupole moment $J_2 = 2.1^{+0.23}_{-0.21} \times 10^{-4}$. The system of WASP-33 contains a stellar companion found by Moya et al. (2011), but this candidate has not been confirmed yet. I summarize parameters of WASP-33's system from the previous literature in Table 1.1.

1.7 The Motivation of This Theses

As I presented in Section 1.3, the spin-orbit obliquity of hot Jupiters around hot stars plays a role in clarifying how gas giant planets have migrated. This is an important part of understanding the origin of hot Jupiters. Even though the projected spin-orbit obliquity around hot stars tends to be scattered, there are only four planets whose real spin-orbit obliquities, ϕ, have been derived. The number of measured ϕ around hot stars is too small to determine the orbital evolution by which a hot

TABLE 1.1: Parameters of WASP-33 from the Previous Literature

Parameter	**Value**	**reference**
Planetary Parameter		
λ_{2008} (deg)	$-110.06^{+0.40}_{-0.47}$	Johnson et al. (2015)
λ_{2014} (deg)	$-112.93^{+0.23}_{-0.21}$	Johnson et al. (2015)
b_{2008}	$0.218^{+0.011}_{-0.029}$	Johnson et al. (2015)
b_{2014}	$0.0840^{+0.0020}_{-0.0019}$	Johnson et al. (2015)
R_p/R_s	0.1143 ± 0.0002	Kovács et al. (2013a)
a/R_s	3.69 ± 0.01	Kovács et al. (2013a)
P (days)	1.2198675 ± 0.0000011	von Essen et al. (2014)
T_c (BJD_{TDB})	$2456878.65739 \pm 0.00015$	von Essen et al. (2019)
v_{FWHM}*(km s^{-1})	16.2 ± 0.5 (TLS)†	Collier Cameron et al. (2010b)
	19.2 ± 0.6 (McD)†	Collier Cameron et al. (2010b)
	18.1 ± 0.3 (NOT)†	Collier Cameron et al. (2010b)
Stellar Parameter		
$V \sin i_s$ (km s^{-1})	$86.63^{+0.37}_{-0.32}$	Johnson et al. (2015)
$\log g$ (cgs)	4.3 ± 0.2	Collier Cameron et al. (2010b)
$T_{\rm eff}$ (K)	7430 ± 100	Collier Cameron et al. (2010b)
Fe/H	0.10 ± 0.2	Collier Cameron et al. (2010b)
V_{mag}	8.3	Collier Cameron et al. (2010b)

* v_{FWHM} is the FWHM of the instinct profile assumed as a Gaussian line.
† TLS: Thüringer Landessternwarte Tautenburg; McD: McDonald Observatory; NOT:Nordic Optical Telescope.

Jupiter generally migrates. Gravity-darkened transit photometry has revealed three hot Jupiters' real obliquities, the ϕ of Kepler-13Ab (Masuda, 2015 and Herman et al., 2018), MASCARA-4b (Ahlers et al., 2020), and WASP-189b (Lendl et al., 2020). The other hot Jupiter is WASP-33b. This planet is not favorable for measuring ϕ by this method because the stellar surface has non-radial pulsations excited by the resonant tidal forcing by a very close binary companion (Fekel, Warner, and Kaye, 2003). Johnson et al. (2015) solved this problem by detecting WASP-33b's nodal precession by Doppler tomography. Then, Iorio (2016) derived $\phi_{2008} = 99^{+5}_{-4}$ deg and $\phi_{2014} = 103^{+5}_{-4}$ deg from information of the nodal precession by Johnson et al. (2015). There are no other exoplanets whose real spin-orbit obliquities are known by Doppler tomography. However, these previous studies used only two datasets in 2008 and 2014. Because only Johnson et al. (2015) checked the WASP-33b's nodal precession, I doubted whether these few data could confirm the precession and whether follow-up observations can reproduce the similar nodal precession; then, more observations to measure its projected obliquity and impact parameter can corroborate the precession confidently. Therefore, I established the way to derive ϕ by nodal precession in this research by verifying WASP-33b's precession and deriving more accurate ϕ of the hot Jupiter via Doppler tomography and transit photometric measurement, which I explain in Section 2.1.

Chapter 2

Methodology

In my thesis, transit photometric measurements and Doppler tomographic observations are important to measure real spin-orbit obliquities. In this chapter, I explain the observation methods which I utilized for this thesis.

2.1 Photometric Measurement

When a planet transits in front of its host star, the apparent flux decreases by blocking the stellar disk. I draw a cartoon of the light curve during transit in Fig 2.1. This section shows what parameters we can gain and the theory of the detection of transit depth.

2.1.1 Transit Photometric Observation

The transit photometric observation can reveal the impact parameter, the semi-major axis scaled by the stellar radius, and the ratio between the stellar radius and planetary radius. First, I explain how the apparent stellar flux loses by citing equations from Part II of Seager (2010). The total flux of the star and the planet $F(t)$ during transit is written as

$$F(t) = F_s(t) + F_p(t) - A(t)F_s(t)\frac{R_p^2}{R_s^2} \tag{2.1}$$

where $F_s(t)$ is the star flux, $F_p(t)$ is the planet flux due to the reflection of stellar light and $A(t)$ is a dimensionless function that represents the overlap area between the stellar and the planet disk. $A = 1$ means that the planet is totally on the stellar disk. $F_s(t)$ varies in time when the stellar activity such as pulsations, starspots and plages

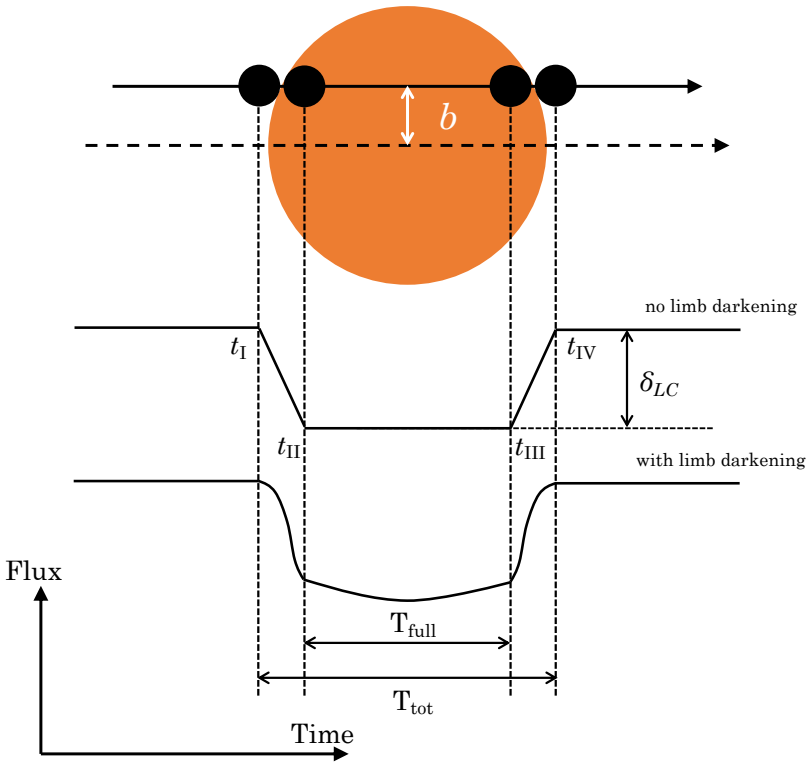

FIGURE 2.1: Cartoon of planet transit and simplified light curves. The middle function shows the trapezoid light curve without limb darkening. Whereas the bottom function is the light curve considering limb dark.

occur, but I simplify $F_s(t)$ is constant $F_s(t) = F_s$. $F_p(t)$ also varies in time thanks to the planetary phase and planetary atmospheric variations but can also be ignored because the planet disk is night side during transit, thereby no lights from the planet. Divided Equation 2.1 by F_s is expressed approximately as

$$f(t) = A(t)\frac{R_p^2}{R_s^2} \tag{2.2}$$

where $f(t) = F(t)/F_s$. Unless grazing transit, the maximum $A(t)$ is 1 while whole planet disk exists on the stellar disk. Thus, the transit depth $\delta_{\rm tr}$ is

$$\delta_{\rm tr} \sim \frac{R_p^2}{R_s^2}. \tag{2.3}$$

from the observed transit light curve, we can measure the radius ratio of the planet and star R_p/R_s. If $A(t)$ is approximately trapezoid, light curves during ingress and egress are linear. However, it is not actual thanks to nonuniform motions of planetary disks and circular shape of the disks (Mandel and Agol, 2002). Moreover, the bottom part of the light curve is not flat because the vertical gradient of temperature in the stellar atmosphere makes limb darkening. The intensity profile $I(X_s, Z_s)$ is

$$I(X_s, Z_s) = I_0 \left\{ 1 - u_1 \left(1 - \sqrt{1 - X_s^2 - Z_s^2} \right) - u_2 \left(1 - \sqrt{1 - X_s^2 - Z_s^2} \right)^2 \right\}, \tag{2.4}$$

where u_1 and u_2 are the limb darkening coefficients calculated based on the stellar parameters, and (X_s, Z_s) is the position on the stellar disk ; X_s and Z_s correspond to x and z of Figure 1.9, respectively.

Here I describe how to measure the impact parameter and the semi-major axis divided by the stellar radius by transit duration. Here I define four times: the ingress beginning time $t_{\rm I}$, the ingress end time $t_{\rm II}$, the egress beginning time $t_{\rm III}$, the egress end time $t_{\rm IV}$. For a circle orbit, citing equations from Part II of Seager (2010), the total duration $T_{\rm tot}$ and the full duration $T_{\rm full}$, measured from the observed light curve (see Figure 2.1), are described as

$$T_{\rm tot} \equiv t_{\rm IV} - t_{\rm I} = \frac{P_{\rm orb}}{\pi} \sin \left\{ \frac{R_s \sqrt{(1 + (R_p/R_s))^2 - b^2}}{a \sin i_p} \right\} \tag{2.5}$$

$$T_{\text{full}} \equiv t_{\text{III}} - t_{\text{II}} = \frac{P_{\text{orb}}}{\pi} \sin\left\{ \frac{R_s \sqrt{(1-(R_p/R_s))^2 - b^2}}{a \sin i_p} \right\} \tag{2.6}$$

where i_p is the angle between the night sky plane and the planet orbit plane, which has the relational expression $b = (a/R_s)\cos i_p$ (see Figure 1.23), and P_{orb} is the orbital period. We can measure P_{orb} by transit frequency from long-term continual observation; space telescopes such as Kepler telescope and TESS have a great advantage about it in terms of observing in dark space. When $R_p \ll R_s \ll a$ and $b \ll 1-(R_p/R_s)$, Equations of 2.5 and 2.6 are approximated as

$$T_{\text{full}} = \frac{P_{\text{orb}} R_s \sqrt{(1+(R_p/R_s))^2 - b^2}}{\pi a \sin i_p} \tag{2.7}$$

$$T_{\text{tot}} = \frac{P_{\text{orb}} R_s \sqrt{(1-(R_p/R_s))^2 - b^2}}{\pi a \sin i_p} \tag{2.8}$$

Thus, using Equation 2.7 and Equation 2.8, we can derive the impact parameters b and the semi-major axis as normalized by stellar radius a/R_s as

$$b^2 = \frac{T_{\text{tot}}^2(1-(R_p/R_s))^2 - T_{\text{full}}^2(1+(R_p/R_s))^2}{T_{\text{tot}}^2 - T_{\text{full}}^2} \tag{2.9}$$

$$\frac{a}{R_s} = \frac{2P_{\text{orb}}\sqrt{R_p/R_s}}{\pi\sqrt{T_{\text{tot}}^2 - T_{\text{full}}^2}} \tag{2.10}$$

2.1.2 Detection of Transit Depth

In this subsection, I consider the proper exposure time for the transit photometric observation. To detect the dimming by transit, we have to avoid the depth buried in the light curve's white noise. Considering the stellar flux is constant without transit, the white noise σ_{LC} is comparable to the reciprocal of signal-to-noise ratio (SNR) of the target star. When the instrument performance of the zero point magnitude m_0, corresponding to 1 ADU per a fixed period T_{fix}, is available, the received photon number per time F_{pho} from a star whose relative magnitude m is

$$F_{\text{pho}} = \frac{10^{-0.4(m-m_0)}G}{T_{\text{fix}}} \tag{2.11}$$

where G is the gain of a CCD camera. Then, the gained photon number $N_{\rm pho}$ with exposure time $T_{\rm exp}$ is derived as

$$N_{\rm pho} = F_{\rm pho} T_{\rm exp} = \frac{10^{-0.4(m-m_0)} G T_{\rm exp}}{T_{\rm fix}} \tag{2.12}$$

Finally, if the star is sufficiently bright, the SNR is calculated as

$$SNR_{\rm pho} = \sqrt{N_{\rm pho}} = \sqrt{10^{-0.4(m-m_0)} \frac{T_{\rm exp}}{T_{\rm fix}} G} \tag{2.13}$$

Thus, from the conditional equation for transit observation

$$\sigma_{LC} \sim \frac{1}{SNR_{\rm pho}} \leq \frac{\delta_{\rm tr}}{3}, \tag{2.14}$$

the requirement exposure time is

$$T_{\rm exp} \geq \frac{9 T_{\rm fix}}{10^{-0.4(m-m_0)} \delta_{\rm tr} G}. \tag{2.15}$$

However, we have to set $T_{\rm exp}$ shorter than one severalth of transit duration considering the time resolution.

2.1.3 Multi-color Transit Photometry

A single-camera can measure some planetary parameters if it is a real planet. However, grazing eclipsing binary and a background eclipsing binary can occur the dimming (See Figure 2.2). These mimics are called false positives. It is not easy to distinguish the darkening origin by a single camera. However, more than one camera with different wavelength-range filters, such as MuSCAT (Narita et al., 2015) and MuSCAT2 (Narita et al., 2019), can tell them apart. This is because a transiting planet is almost dark in all wavelengths, whereas an eclipsing binary shines itself, and its brightness varies significantly with wavelength (Colón, Ford, and Morehead, 2012). Thus, multi-color transit photometry is one of the methods to verify a planet.

When a planet has an atmosphere composed light particles such as hydrogen or including a haze, the ratio between the stellar radius and the planet radius, which corresponds to the transit depth, depends on wavelength slightly. This is because

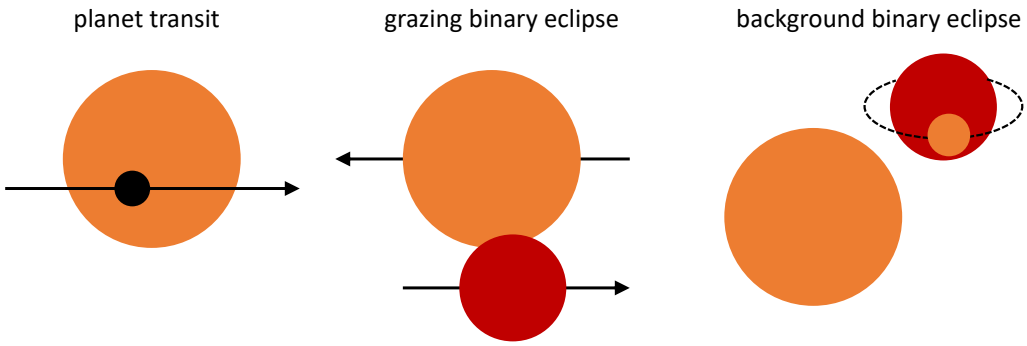

FIGURE 2.2: Illustration of planet transit (left), grazing binary eclipse (middle) and background binary eclipse (right). Binaries like middle and right figures can imitate transit dimming as if the planet transit happened.

bluer wavelength scatters easily in the atmosphere by Rayleigh scattering. In the case of MuSCAT and MuSCAT2 observations, we can ignore the effect of atomic and molecular absorption for the difference of the transit depths because their filters' wavelength ranges ($\sim$ 100 nm) are wider than the widths of the absorption lines ($<$ 1 nm). Thus, multi-color transit photometry can also estimate a condition of the planetary atmosphere or haze; I do not do the atmosphere observation in this thesis.

2.2 Doppler Tomography

I have explained how to measure λ via Doppler Tomography in Section 1.3. I describe how to get the planetary shadow, the shadow model, and the detection theory in this section.

2.2.1 Least Squares Deconvolutions

Regarding an observed spectrum as a convolution of a stellar line profile and a line mask showing information of atomic absorption depth by δ function (see Figure 2.3), Least-squares deconvolution (LSD) can extract the stellar line profile (Donati et al., 1997). This method can be applied even though the spectrum contains broadened absorption lines due to the fast stellar rotation.

I create a pipeline to get the line profile by LSD following the exact mathematical method by Kochukhov, Makaganiuk, and Piskunov (2010). The observed spectrum

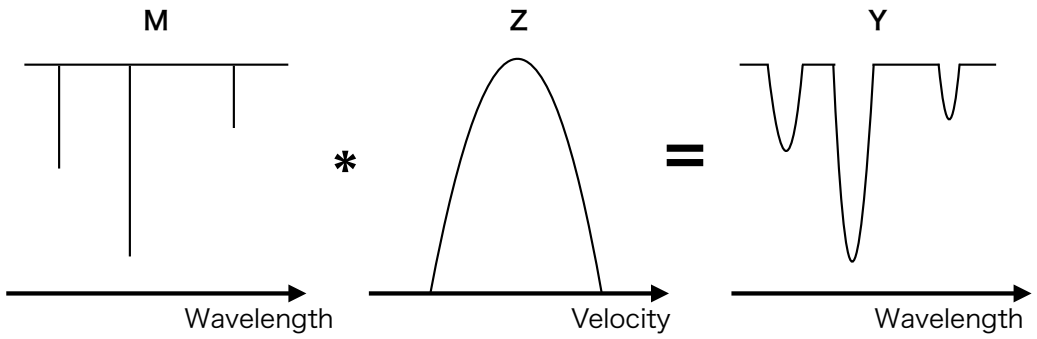

FIGURE 2.3: Cartoons of atomic absorption $\boldsymbol{M}$, stellar line profile $\boldsymbol{Z}$ and observed spectrum $\boldsymbol{Y}$.

$\boldsymbol{Y}$ with n data plots can be expressed by $\boldsymbol{Y} = \boldsymbol{MZ}$, where $\boldsymbol{M}$ is the line mask expressed a matrix of $m \times n$ and $\boldsymbol{Z}$ the line profile with m data points. To calculate the best-fitting profile $\boldsymbol{Z}$, the following parameter $\chi^2_{\rm spec}$ should be minimized by the least square method.

$$\chi^2_{\rm spec} = (\boldsymbol{Y} - \boldsymbol{MZ})^T \boldsymbol{S}^2 (\boldsymbol{Y} - \boldsymbol{MZ}), \tag{2.16}$$

Here $\boldsymbol{S}$ is diagonal square matrix with $S_{j,j} = \sigma_j^{-2}$ $(1 \leq j \leq n)$, where σ_j is a error of the spectrum at the jth pixel. Differentiating Equation 2.16 by $\mathbf{Z}$ partially, we can write the best-fitting $\mathbf{Z}$ as

$$\mathbf{Z} = (\boldsymbol{M}^{\mathbf{T}} \boldsymbol{S}^{\mathbf{2}} \boldsymbol{M})^{-\mathbf{1}} (\boldsymbol{M}^{\mathbf{T}} \boldsymbol{S}^{\mathbf{2}} \boldsymbol{Y}). \tag{2.17}$$

The right part of Equation 2.17, $\boldsymbol{M}^T \boldsymbol{S}^2 \boldsymbol{Y}$, shows the weighted cross-correlation between the line mask and the observation spectrum. The $\boldsymbol{M}^T \boldsymbol{S}^2 \boldsymbol{M}$ is the autocorrelation matrix and determines the uncertainties of the line profile. I calculate σ_j as inverse of the square root of the photon number per pixel element. the element of $\boldsymbol{M}$ can be expressed as

$$\begin{aligned} M_{i,j} &= w_l \frac{v_{j+1} - V_i}{v_{j+1} - v_j}, M_{i,j+1} = w_l \frac{V_i - v_{j+1}}{v_{j+1} - v_j}; V_i = c\frac{\lambda_i - \lambda_l}{\lambda_l} \quad (v_j \leq V_i \leq v_{j+1}) \\ M_{i,j} &= 0 \quad (\text{otherwise}) \end{aligned} \tag{2.18}$$

where λ_i is the series of wavelength ($1 \leq i \leq m$) in the observed spectrum, v_j is the series of velocity ($1 \leq j \leq n$) in the line profile, λ_l is the wavelength of the lth atomic spectrum in ascending order in wavelength, w_l is the depth of lth atomic spectrum and c is the light speed.The index l correspond to the lth bidiagonal component in the matrix $\boldsymbol{M}$. I prepare the line mask from the Vienna Atomic Line Database (VALD; Kupka et al., 2000). This data calculates available atoms and each depth of each atom from effective stellar temperature, metallicity, surface gravity and microturbulence. After the LSD process, I subtract the average line profile of out-of-transit ones from all stellar line profiles to get the planetary shadow.

2.2.2 Model of Planetary Shadow

I adopt an analytic method of a rotational broadening line profile to create a planetary shadow model referring the appendix of Hartman et al. (2015). Here I estimate that a host star is a solid sphere. I also assume that its spin axis is normal to the line of sight though $\sin i_s \neq 1$. These assumptions make $v/V \sin i_s$ equivalent to x, a component perpendicular to stellar spin axis in units of the stellar radius (see Figure 1.9).

A normalized rotational broadening profile $G(x)$ is given as

$$G(x) = \frac{G'(x)}{\int_{-\infty}^{\infty} G'(x)dx} \tag{2.19}$$

with

$$G'(x) = \int_{-z_{\min}}^{z_{\max}} I(x,z)dz, \tag{2.20}$$

where $I(x,z)$ is a stellar surface intensity at (x,z), the projected position relative to the center of the star. When the intensity is a quadratic limb darkening law,

$$I(x,z) = I_0 \left\{ 1 - u_1 \left(1 - \sqrt{1-x^2-z^2} \right) - u_2 \left(1 - \sqrt{1-x^2-z^2} \right)^2 \right\}, \tag{2.21}$$

it works out the rotational broadening line profile to the equation

$$G'(x) = \begin{cases} 2(1-u_1-u_2)\sqrt{1-x^2} + \frac{\pi}{2}(u_1+2u_2)(1-x^2) - \frac{4}{3}u_2(1-x^2)^{3/2} & (|x|<1) \\ 0 & (\text{otherwise}) \end{cases} \tag{2.22}$$

and

$$\int_{-\infty}^{\infty} G'(x)dx = \pi\left(1 - \frac{u_1}{3} - \frac{u_2}{6}\right). \tag{2.23}$$

When a planet with radius $r(= R_p/R_s)$ is at (x_p, z_p), the projected position is written as

$$x_p(t) = \frac{a}{R_s}\sin\left(2\pi\frac{t-T_0}{P_{\rm orb}}\right)\cos\lambda + b\cos\left(2\pi\frac{t-T_0}{P_{\rm orb}}\right)\sin\lambda \tag{2.24}$$

$$z_p(t) = -\frac{a}{R_s}\sin\left(2\pi\frac{t-T_0}{P_{\rm orb}}\right)\sin\lambda + b\cos\left(2\pi\frac{t-T_0}{P_{\rm orb}}\right)\cos\lambda, \tag{2.25}$$

then the broadening profile is decreased due to the planet by

$$\begin{aligned} K(x,t) &= \int_{z_1(x,t)}^{z_2(x,t)} I(x,z)dz \\ &= (1-u_1-u_2(2-x^2))(z_2-z_1) + \frac{u_2}{3}(z_2^3-z_1^3) \\ &\quad -\frac{u_1+2u_2}{2}\left[z_2\sqrt{1-x^2-z_2^2} - z_1\sqrt{1-x^2-z_1^2}\right. \\ &\quad \left. + (1-x^2)\left\{\sin^{-1}\left(\frac{z_2}{\sqrt{1-x^2}}\right) - \sin^{-1}\left(\frac{z_1}{\sqrt{1-x^2}}\right)\right\}\right] \end{aligned} \tag{2.26}$$

with

$$z_1 = \begin{cases} 0 & (|x|>1 \text{ or } |x-x_p|>r) \\ \sqrt{1-x^2} & \left(z_p - \sqrt{r^2-(x-x_p)^2} > \sqrt{1-x^2}\right) \\ -\sqrt{1-x^2} & \left(z_p - \sqrt{r^2-(x-x_p)^2} < -\sqrt{1-x^2}\right) \\ z_p - \sqrt{r^2-(x-x_p)^2} & (\text{otherwise}) \end{cases}$$

(2.27)

and

$$z_2 = \begin{cases} 0 & (|x| > 1 \text{ or } |x - x_p| > r) \\ \sqrt{1-x^2} & \left(z_p + \sqrt{r^2 - (x-x_p)^2} > \sqrt{1-x^2}\right) \\ -\sqrt{1-x^2} & \left(z_p + \sqrt{r^2 - (x-x_p)^2} < -\sqrt{1-x^2}\right) \\ z_p + \sqrt{r^2 - (x-x_p)^2} & (\text{otherwise}) \end{cases} \tag{2.28}$$

The convolution between $K(x,t)$ and the stellar intrinsic Gaussian profile is our model of the planetary shadow. We note that in the appendix of Hartman et al. (2015), a part of the above expression

$$z_2\sqrt{1-x^2-z_2^2} - z_1\sqrt{1-x^2-z_1^2}, \tag{2.29}$$

in equation (2.26) appears to be mistakenly expressed as

$$z_2(1-x^2-z_2^2) - z_1(1-x^2-z_1^2). \tag{2.30}$$

2.2.3 Detection of Planetary Shadow

I calculate the required SNR per resolution element to detect a planetary shadow clearly. First, I estimate the depth of the spectral line of a fast rotating star, $D_{\rm fast}$, roughly. The normalized rotational broadening line profile $G'(v)$ is expressed as

$$\begin{aligned} G'(v) \quad = \quad & \frac{12(1-u_1-u_2)}{\pi(6-2u_1-u_2)V\sin i_s}\sqrt{1-\left(\frac{v}{V\sin i_s}\right)^2} \\ & + \frac{3u_1-6u_2}{(6-2u_1-u_2)V\sin i_s}\left[1-\left(\frac{v}{V\sin i_s}\right)^2\right] \\ & - \frac{8u_2}{\pi(6-2u_1-u_2)V\sin i_s}\left[(1-\left(\frac{v}{V\sin i_s}\right)^2\right]^{3/2} \end{aligned} \tag{2.31}$$

from Equation 2.22 and Equation 2.23. Thus, $G'(v=0) \propto 1/V\sin i_s$. Here I approximate the atomic line as the shape of the $dG'(v)$, with the width $v_{\rm mic}$, where d is the depth from the VALD data and $v_{\rm mic}$ is the microturbulent velocity (typically ~ 2 km

s^{-1}). Hence, $D_{\rm fast}$ is

$$D_{\rm fast} = d\frac{v_{\rm mic}}{V \sin i_s}. \tag{2.32}$$

When there are n absorption lines in the spectrum, about 700 lines with $d > 0.55$ between 5000Å and 6000Å, the averaged depth $D_{\rm fast,ave}$ is

$$D_{\rm fast,ave} = \frac{1}{n}\sum_i^n D_{{\rm fast},i} = \frac{1}{n}\sum_i^n d_i \frac{v_{\rm mic}}{V \sin i_s}. \tag{2.33}$$

If the all depths are the same,

$$D_{\rm fast,ave} = D_{\rm fast}. \tag{2.34}$$

On the other hand, the noise of each absorption line $\sigma_{\rm sp}$ is expressed as

$$\sigma_{\rm sp} = \frac{1}{\sqrt{N}} \tag{2.35}$$

N is the photon number per resolution element and described as

$$N = N_\lambda f \Delta\lambda \Delta x T_{\rm exp} = \frac{10^{-0.4m} F_\lambda A \eta f \Delta\lambda \Delta x T_{\rm exp}}{h\nu}, \tag{2.36}$$

where m is the magnitude, F_λ is the flux of zeroth-magnitude; $F_\lambda = 3.631 \times 10^9$ erg cm^{-2} s^{-1} Å^{-1} is one of V-band flux of A0 star (Bessell, Castelli, and Plez, 1998), A is the area of telescope's mirror, f is the fraction of the light entering the slit, η is the total throughput, $\Delta\lambda$ is the dispersion (typically 0.015 Å pixel^{-1} at 5500Å), Δx is the width of the spectrum line (typically 5 pixel), h is the Planck constant and ν is the frequency of light. $N_\lambda (= 10^{-0.4m} F_\lambda A\eta/h\nu)$ expresses the number of photon per wavelength and per pixel through the telescope and the instrument before reaching the slit; I make a equation of N_λ from Section 5.2 in Johnson (2013). Then, the noise of average line profile is

$$\sigma^2_{\rm sp,ave} = \frac{1}{n^2}\sum_i^n \sigma^2_{{\rm sp},i} = \frac{1}{n^2}\sum_i^n \frac{1}{N_i}. \tag{2.37}$$

When the photon number of each line profile is same ($N_i = N$), the average noise is approximated as

$$\sigma_{\mathrm{sp,ave}} = \sqrt{\frac{1}{n^2}\sum_i^n \frac{1}{N_i}} = \frac{1}{\sqrt{nN}}. \tag{2.38}$$

Here I note this noise is for the line profile with the interval of velocity data points Δv_0 which is written as

$$\Delta v_0 = c\frac{\Delta\lambda}{\lambda_0}, \tag{2.39}$$

where $\Delta\lambda$ is the wavelength interval of the observed spectrum, and λ_0 is the center of the line profile in the wavelength field. When the lines are in the range of 5000Å to 6000Å, the interval of velocity data points is $\Delta v_0 \sim 1$ km s^{-1} roughly. It is possible to make the interval narrow ($\Delta v < \Delta v_0$) but the noise will increase as $\sigma_{\mathrm{sp,ave}}\sqrt{\Delta v_0/\Delta v}$. To avoid that too wide interval of velocity data points hides the planetary shadow, $V \sin i_s$ should be satisfied

$$V \sin i_s > 3\frac{R_s}{R_p}\Delta v \tag{2.40}$$

Thus, from Equation 2.40, it is difficult to detect the planetary shadow around a too slow rotation star.

When the stellar rotation speed is fast enough, the width of planetary shadow is so wide that its points in stellar line profile can shape the shadow's depth with D_{fast}. Thus, the condition of detecting planetary shadow is

$$3\sigma_{\mathrm{sp,ave}} < D_{\mathrm{fast,ave}}\frac{R_p}{R_s}, \tag{2.41}$$

where the right side of Equation 2.41 shows the depth of the planetary shadow. Equation 2.41 can be transformed using Equation 2.32, Equation 2.34 and Equation 2.38 into

$$N > \frac{9}{n}\frac{R_s^2}{R_p^2}\left(\frac{V \sin i_s}{v_{\mathrm{mic}} d}\right)^2. \tag{2.42}$$

Therefore, the required SNR per resolution element is

$$SNR_{\rm min} = \sqrt{N_{\rm min}} = \frac{3}{\sqrt{n}} \frac{R_s}{R_p} \frac{V \sin i_s}{v_{\rm mic} d} \sim 120 \times 0.1 \left(\frac{R_p}{R_s} \right)^{-1} \left(\frac{V \sin i_s}{100 {\rm km\ s^{-1}}} \right). \quad (2.43)$$

Here, the coefficient of the right side of Equation 2.43 is calculated assuming that a spectrum has 700 absorption lines with $d = 0.05$ and $v_{\rm mic} = 2 {\rm km\ s^{-1}}$ from 5000 Å to 6000 Å.

In the end of Chapter 2, I summarized parameters shown in this chapter in Table 2.1. I distinguished their values from measured, calculated and fixed ones.

TABLE 2.1: Summary of Parameters in Section 2

Parameter	**Name**	Type of Value	Note
$P_{\rm orb}$	orbital period	measured value	from long-term photometry
$T_{\rm tot}$	total duration	measured value	from a single transit photometry
$T_{\rm full}$	full duration	measured value	from a single transit photometry
$\delta_{\rm full}$	transit depth	measured value	from a single transit photometry
u_1, u_2	limb darkening coefficients	calculated value	from stellar parameters
R_p/R_s	impact parameter by stellar radius	calculated value	from Equation 2.3
b	impact parameter	calculated value	from Equation 2.9
G	gain of CCD	fixed value	depending on CCD
a/R_s	scaled semi-major axis by stellar radius	calculated value	from Equation 2.10
$\boldsymbol{M}$	line mask matrix	calculated value	from VALD data
$\boldsymbol{Y}$	observed spectral line	observed value	from spectral data
$V \sin i_s$	apparent stellar rotation speed	measured value	from observed dline profile
$v_{\rm mic}$	microturbulent velocity	fixed value	assuming $v_{\rm mic} \sim 2$ km s^{-1}
d	depth of absorption line	fixed value	assuming $d = 0.05$
n	number of lines	fixed value	assuming $n = 700$
$D_{\rm fast}$	depth of line profile	calculated value	from Equation 2.32
A	are of telescope's mirror	fixed value	depending on telescopes
m	stellar magnitude	fixed value	depending on stars
η	total throughput	fixed value	depending on instruments
f	fraction of the light entering slit	fixed value	depending on instruments
$\Delta\lambda$	wavelength dispersion	fixed value	depending on instruments
Δx	width of spectrum line	fixed value	depending on instruments
N	photon number per resolution element	calculated value	assuming from 2.36

Chapter 3

Nodal Precession of WASP-33b

3.1 Methodology for WASP-33b Measurement

3.1.1 Spectroscopic Observation of WASP-33b's Transit

I used five spectroscopic data sets of WASP-33 around planetary transits. One of them was taken by the 8.2 m Subaru telescope with High Dispersion Spectrograph (HDS, Noguchi et al., 2002) on 2011 October 19th UT. Others are the data sets observed by Harlan J. Smith Telescope (HJST) with Robert G. Tull Coudé Spectrograph (TS23; Tull et al., 1995) at McDonald Observatory on 2008 November 12th UT, 2014 October 4th UT and 2016 December 11th UT. The other is the data I observed with HIgh Dispersion Echelle Spectrograph (HIDES; Izumiura (1999)) on 2019 December 29th UT.

The data set of HDS includes 35 spectra obtained with a resolution of $R = 110,000$; 16 spectra are taken in-transit. The exposure times are 600 s for 33 spectra and 480 s for two spectra. I adopted a range of wavelength from 4930Å to 6220Å except for Na D lines and regions of wavelength around bad pixels. From these spectra, I took continua, corrected them to eliminate the Earth's atmospheric dispersion by dividing spectra of a rapidly rotating star HR8634 ($V \sin i_s \sim 140$ km s^{-1}: Abt, Levato, and Grosso, 2002), and shifted these spectra to the barycentric frame. For these processes, I used PyRAF and the calculating tools from Wright and Eastman (2014) and Eastman, Siverd, and Gaudi (2010). Then I found that each SNR per pixel of each spectrum was ∼160 at 5500 Å. To pick up each line profile from each spectrum, I adopted least-squares deconvolution (LSD; Donati et al., 1997). In this method, I regard an observed spectrum as a convolution of a line profile and a series of delta

functions. I referred to depths of about 1,000 atomic absorption lines from Vienna Atomic Line Database (VALD; Kupka et al., 2000) and considered these lines delta functions. Then I derived all of the line profiles and their error bars by the deconvolution using the matrix calculations in Kochukhov, Makaganiuk, and Piskunov (2010). Finally, I shifted these profiles by the velocity of this system $\gamma = -3.69$ km s^{-1} (Collier Cameron et al., 2010b).

On the other hand, three data sets of TS23 have $R = 60,000$ resolution. One data set for the 2008 epoch has 13 spectra and SNR per pixel of $\sim$140. Another set for the 2014 epoch has 21 spectra and SNR per pixel of $\sim$280. Both of them include ten in-transit spectra. All of their exposure times are 900 s. I note that the two data sets have already been extracted and published in Johnson et al. (2015), and I used the extracted line profile series. I also utilized the other reduced and extracted data set for the 2016 epoch having 21 spectra and SNR per pixel of $\sim$250. The data for 2016 also includes ten in-transit spectra.

Moreover, the HIDES data set includes 12 spectra obtained with a resolution of $R = 65,000$; 8 spectra taken in-transit. All of their exposure times are 1200 s. I utilized a range of wavelength from 4980 Å to 6220 Å except for Na D lines and regions of wavelength around bad pixels. I reduced these spectral data by subtracting bias and dark features, flat dividing, making one-dimensional spectrum, and wavelength calibration. I then took continua of them as well as the process of HDS. I chose alp Leo as a rapid star ($V \sin i_s \sim 300$ km s^{-1}; Abt, Levato, and Grosso, 2002) to erase the Earth's atmospheric absorption lines. Then, I shifted these spectra to the barycentric frame by `PyRAF`. I measured each SNR per pixel of each spectrum $\sim$ 100 at 5500 Å, which was the limitation. Finally, I extracted stellar line profiles in the same way as the analysis of HDS data.

3.1.2 Extracting planetary shadow

I computed a median line profile for each data set. I subtracted the median line profile from each exposure's line profile to calculate the time series of line profile residuals. In the time series of residuals, there is not only a planetary shadow caused by the WASP-33b's transit but also a striped pattern (see Figure 3.1). The different tracks occur from non-radial pulsations on the surface of WASP-33 (Collier Cameron

et al., 2010b). Herrero et al. (2011) showed the pulsation period is about 68 min, but it is hard to determine the period from the Doppler tomographic results due to the irregular patterns.

To extract only the planetary shadow, I applied a Fourier filtering technique (Johnson et al., 2015). First, I did a two-dimensional Fourier transform. There are gathered pulsation's components in the Fourier space in the first and third quadrants and planetary shadow's components in the second and fourth quadrants. Second, I made a filter in which I set unity in two diagonal quadrants, including power from the planetary shadow, and zero in the other quadrants, including power from the pulsation with a Hann function between these quadrants. Finally, I multiplied the Fourier space by the filter and performed an inverse Fourier transform on the filtered Fourier space to extract the planetary shadow'. These procedures are shown from top to bottom in Figure 3.1.

3.1.3 Deriving parameters

To obtain best-fit values and uncertainties of transit parameters, I adopted Markov chain Monte Carlo (MCMC) using the code `EMCEE` (Foreman-Mackey et al., 2013).

I modeled a planetary shadow by a convolution between Equation 2.26 in Section 2.2 and a Gaussian line profile due to intrinsic broadening, thermal broadening, and micro-turbulence. I then applied the same filter to the planetary shadow model following the procedures described in Section 2.2

I fitted the observed residuals of the five data sets to the models with 21 parameters using MCMC: λ, b and transit mid-time T_c of each epoch, $V \sin i_s$, R_p/R_s, a/R_s, two quadratic limb darkening coefficients and FWHM of Gaussian line profile. Note that limb darkening coefficients are derived by the triangular sampling method of Kipping (2013), q_1 and q_2. Here I estimated that q_1 and q_2 of HDS and TS23 are equivalent. They can be calculated from the stellar parameters, i.e., effective temperature $T_{\rm eff}$, surface gravity $\log g$, and metallicity. I set priors of λ and b for all epochs and the FWHM as uniform functions, otherwise as Gaussian priors. For values and widths of Gaussian priors, I set priors of R_p/R_s and a/R_s based on the values and uncertainties from Kovács et al. (2013b), ones of each T_c of each epoch from P_{orb} in von Essen et al. (2014) and T_0 in von Essen et al. (2019), ones of q_1 and q_2 calculated

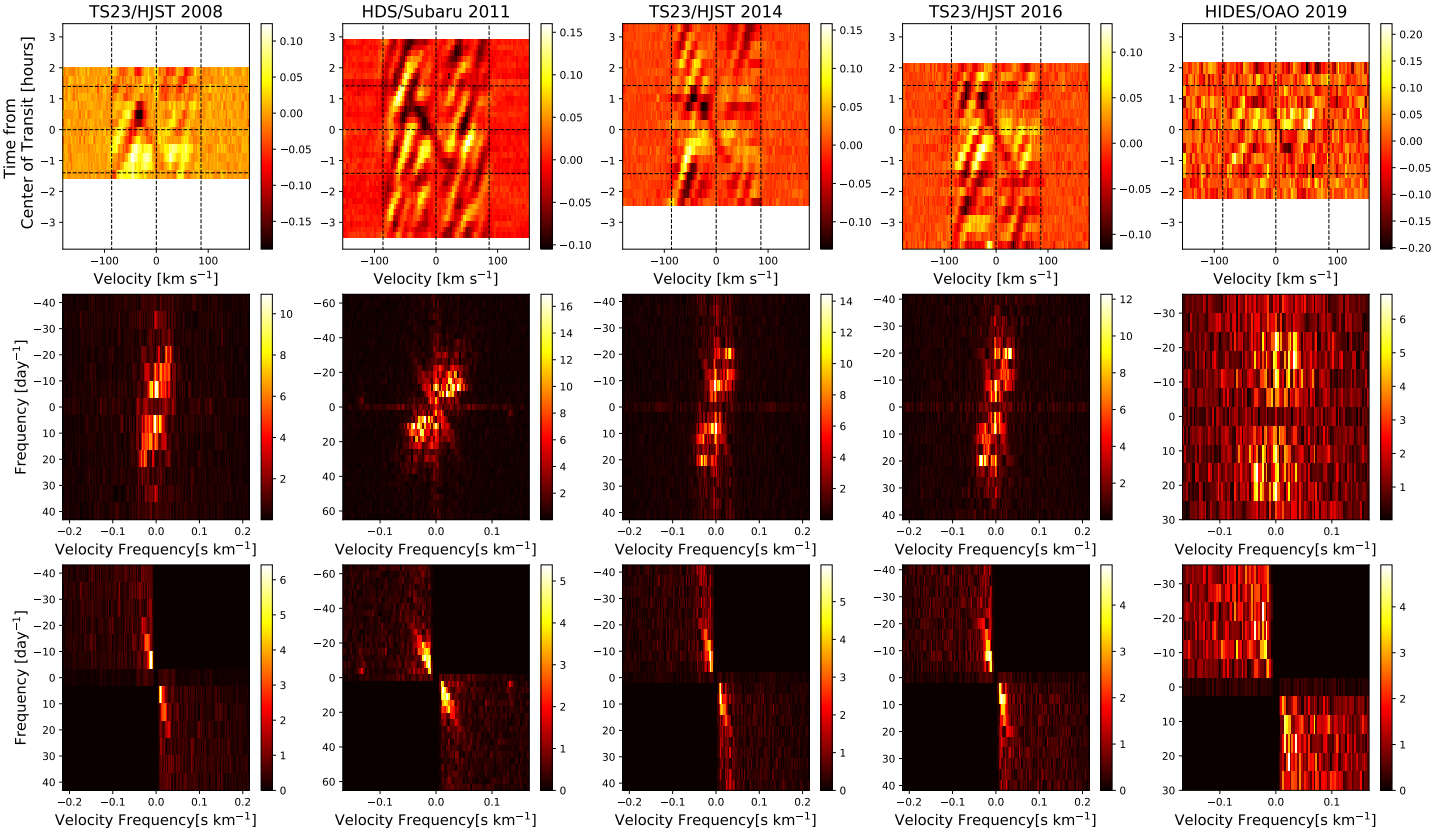

FIGURE 3.1: Doppler tomographic data sets and Fourier filters. The first, second, and third columns are the data sets of TS23 in 2008, HDS in 2011, TS23 in 2014, TS23 in 2016, and HIDES in 2019, respectively. Top row: observed residuals of line profile series. Virtual dotted lines show $v = 0, \pm v \sin i_s$. Bottom, middle and upper horizontal dotted lines show the beginning, middle, and end of WASP-33b's transit, respectively. Second row: Fourier spaces after Fourier transform of the residuals of line profile series. These color scales are shown in square-roots. A faint narrow structure from the right bottom to the left upper is a component of WASP-33b's planetary transit. On the other hand, a bright wide structure from the left bottom to the right upper is a pulsation component. Third row: filtered Fourier space so that only the transit component remains.

by PyLDTk (Parviainen and Aigrain, 2015, Husser et al., 2013), and ones of $V \sin i_s$ from Johnson et al. (2015).

For the fitting, I maximize the logarithm of the posterior probability $\ln L_{\rm post}$,

$$\ln L_{\rm post} = -\sum_i \frac{(O_i - C_i)^2}{\sigma_i^2} - \sum_j \frac{(p_j - \mu_j)^2}{s_j^2}, \tag{3.1}$$

where O_i is the data, C_i is the model, σ_i is the error for the ith data point, p is the parameter value at the gained iteration of the Markov chain, μ is the value from the literature, and s is the uncertainty from literature. Indices j denotes the parameters for the Gaussian priors. Here I note that there are no parameters related to the uniform priors. However, when the Markov chain's gained iteration shows the values out of range in the uniform prior, the posterior $L_{\rm post}$ turns zero. To converge these parameters' values, I ran 4,000 steps, cut off the first 2,000 steps as burn-in, and iterated this set 100 times. The posterior distributions are plotted in Figure 3.2.

3.2 Photometric Measurement of WASP-33b

3.2.1 Photometric Observation of WASP-33b's Transit

I also observed transit of WASP-33b by photometry with two instruments of simultaneous cameras: Multicolor Simultaneous Camera for studying Atmospheres of Transiting exoplanets (MuSCAT; Narita et al., 2015) on 188cm telescope at Okayama Astrophysical Observatory (OAO) and MuSCAT2 (Narita et al., 2019) on Telescopio Carlos Sánchez (TCS) 152cm telescope at Teide Observatory (OT). MuSCAT has three different filters, $g_2^{'}$ (400-550 nm), $r_2^{'}$ (550-700 nm) and $z_{\rm s,2}$ (820-920 nm) bands. On the other hand, MuSCAT2 contains four filters, $g_2^{'}$, $r_2^{'}$, $z_{\rm s,2}$ and $i_2^{'}$ (700-820 nm). These bands are the types of Astrodon Photometrics Generation 2 Sloan filters. I gained the dataset of MuSCAT on November 5th UT. I set exposure times of $g_2^{'}$, $r_2^{'}$ and $z_{\rm s,2}$ bands for 4 s, 4 s and 10 s, respectively. I also analyzed the data set of MuSCAT2 on October 18th UT. The exposure time of $g_2^{'}$, $r_2^{'}$, $i_2^{'}$ and $z_{\rm s,2}$ are 3 s, 2 s, 5 s and 12 s, respectively.

I reduced both data sets using the pipeline created by Fukui et al. (2011), which

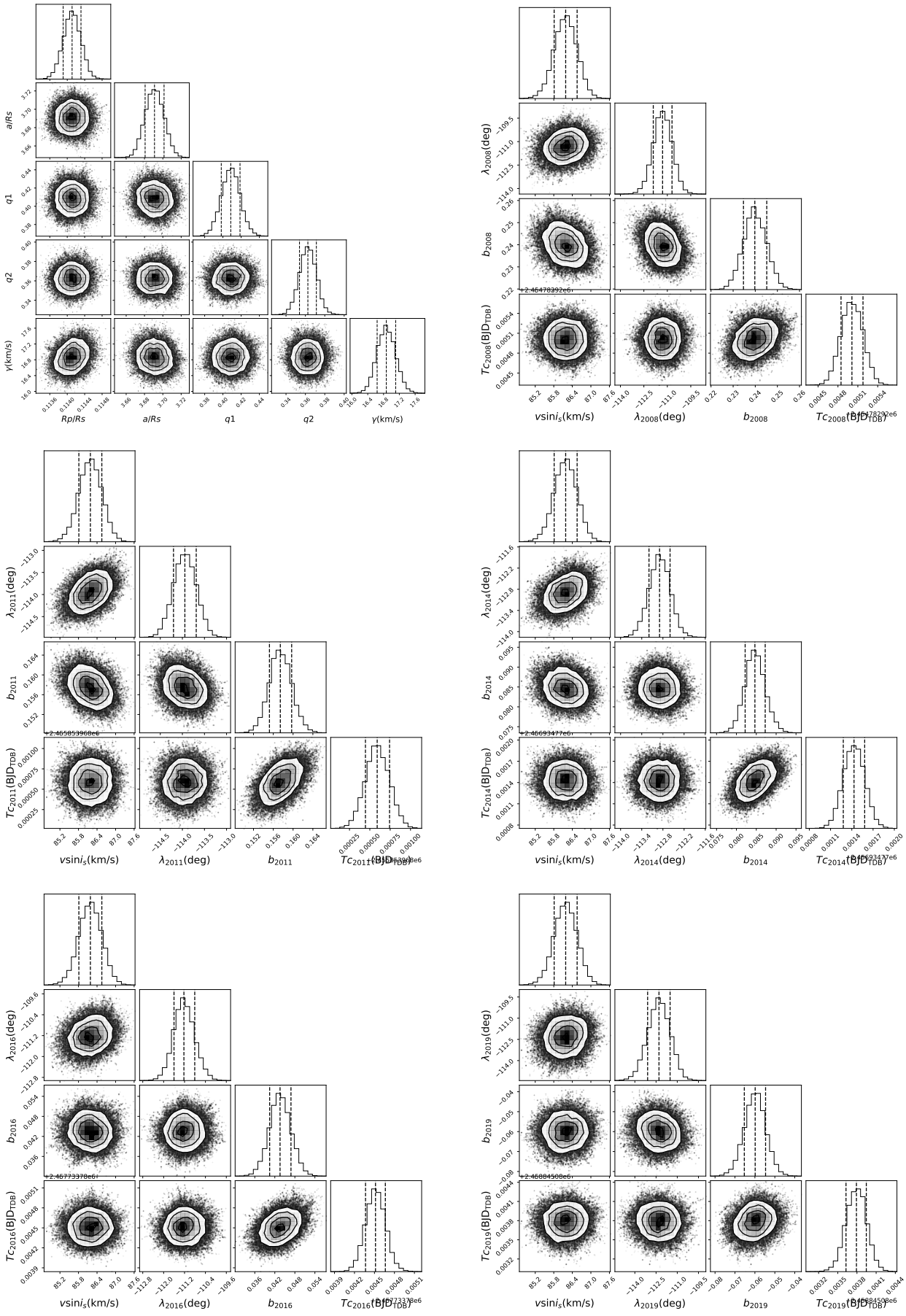

FIGURE 3.2: Corner plots for the free parameters after using MCMC in section 2.3. Black circles indicate 68%, 95% and 99.7% confidence from the inside. In each posterior distribution of each parameter, vertical dotted lines show its best-fit value (middle) and 1σ confidence (both ends). We created these plots with corner.py (Foreman-Mackey, 2016).

executes flat division and dark subtraction. Then, to make light curves of WASP-33b, I performed aperture photometry using the pipeline by Fukui et al. (2016). This process finds the stellar barycenter on every frame. I used BD+36 488, the second brightest star image in the frame, as a companion star to erase the variation of raw flux from the sky weather, atmospheric turbulence, airmass, and so on. Next, the pipeline reads the shift of the stellar position comparing with the reference frame. It photometers the target star and the comparison star in the aperture radius. Here I set the radii 36 pixels for MuSCAT and 40 pixels for MuSCAT2. After the sky background in the torus area centered on the stellar barycenter, the pipeline subtracts the sky background from WASP-33b's flux and the comparison's one. Finally, dividing WASP-33b's flux by the comparison's one makes its light curve.

3.2.2 Light Curve Fitting

To measure the WASP-33b's impact parameter b in 2017 and 2018, I produced light curve models with Gaussian process by using the python code `exoplanet` (Foreman-Mackey et al., 2020). WASP-33b's light curve contains not only the dimming by the transit, but also a short sinusoidal-wave-like feature due to the stellar pulsations. Thus, Following the previous study Johnson et al. (2015), I applied a Matern 3/2 kernel $\mathbf{K_{ker}}$ whose element is expressed as

$$k_{i,j} = \alpha^2 \left(1 + \frac{\sqrt{3}|t_i - t_j|}{l}\right) \exp\left(-\frac{\sqrt{3}|t_i - t_j|}{l}\right) + \sigma_i^2 \delta_{i,j} \tag{3.2}$$

for the Gaussian process. i and j denote the orders of photometic observation's data, t_i and t_j are the observation times, α and l are the hyper parameters indicates the amplitude and timescale of the stellar variations, and σ is the error of data point i respectively.

Then, I fitted the light curves on two epochs to the models with 30 parameters using MCMC: base line B for each light curve, b and T_c of each epoch, R_p/R_s, two quadratic limb darkening coefficients u_1, u_2 and α of each bands, l, a/R_s and $P_{\rm orb}$. I set priors of b for both epochs and R_p/R_s for all bands as uniform functions, otherwise as Gaussian priors. For values and widths of Gaussian priors, I referred values and widths of Gaussian priors from Johnson et al. (2015) for α and l and von Essen et

al. (2014) for $P_{\rm orb}$; the other ones are quoted in the same way as the spectral analysis. I measured these parameters so that the likelihood with Gaussian process

$$\ln P_{\rm like} = -\frac{1}{2}(\ln|\mathbf{K_{ker}}| + \mathbf{r^T K_{ker}^{-1} r}) \tag{3.3}$$

is maximized. $\mathbf{r}$ is a series of residuals by subtracting model data from observation data. In the MCMC process by `PyMC` (Salvatier, Wiecki, and Fonnesbeck, 2016), I ran 1,000 steps, cut off the first 500 steps as burn-in, and iterated this set 50 times. The posterior distributions are plotted in Figure 3.3 and Figure 3.4.

3.3 Fitting with Nodal Precession Model

The angular momentum of WASP-33b's planetary orbit $|\overrightarrow{L_p}|$ $(= 2\pi M_p a^2/P_{\rm orb})$ is much smaller than the stellar rotational angular momentum of its host star $|\overrightarrow{L_s}|$; $|\overrightarrow{L_p}|/|\overrightarrow{L_s}|$ is ~ 0.05 using the value of $|\overrightarrow{L_s}|$ from Iorio (2011), ones of M_p from Lehmann et al. (2015), a and P from Collier Cameron et al. (2010b). In this case, we can regard the stellar rotational axis as a stable vector, thereby approximating $\phi_p \sim \phi$ and $i_a \sim i_s$. Thus, I calculated the changes of b and λ

$$b(t) = \frac{a}{R_s}(\cos\phi\cos i_s + \sin\phi\sin i_s\cos\theta(t)) \tag{3.4}$$

$$\tan\lambda(t) = \frac{\sin\phi\sin\theta(t)}{\sin\phi\cos i_s\cos\theta(t) - \cos\phi\sin i_s}. \tag{3.5}$$

Here θ can be expressed as

$$\theta(t) = \frac{3\pi J_2 R_s^2\cos\phi}{P_{\rm orb}a^2}t + \theta_0, \tag{3.6}$$

where the slope of Equation 3.6 is the precession speed.

Then, I fitted the model of Equations 3.4 and 3.5 with the measured values by MCMC using `PyMC`. I considered ϕ, $\theta(t = 2008)$, i_s and J_2 as free parameters and set their priors as uniform functions. Here I regard θ in 2008 as the intercept of Equation 3.6 instead of θ_0. For this fitting, I minimize the $\chi_{\rm pre}$,

$$\chi^2_{\rm pre} = \sum_i \frac{(O_{{\rm mes},i} - C_{{\rm mod},i})^2}{\sigma^2_{{\rm mes},i}} \tag{3.7}$$

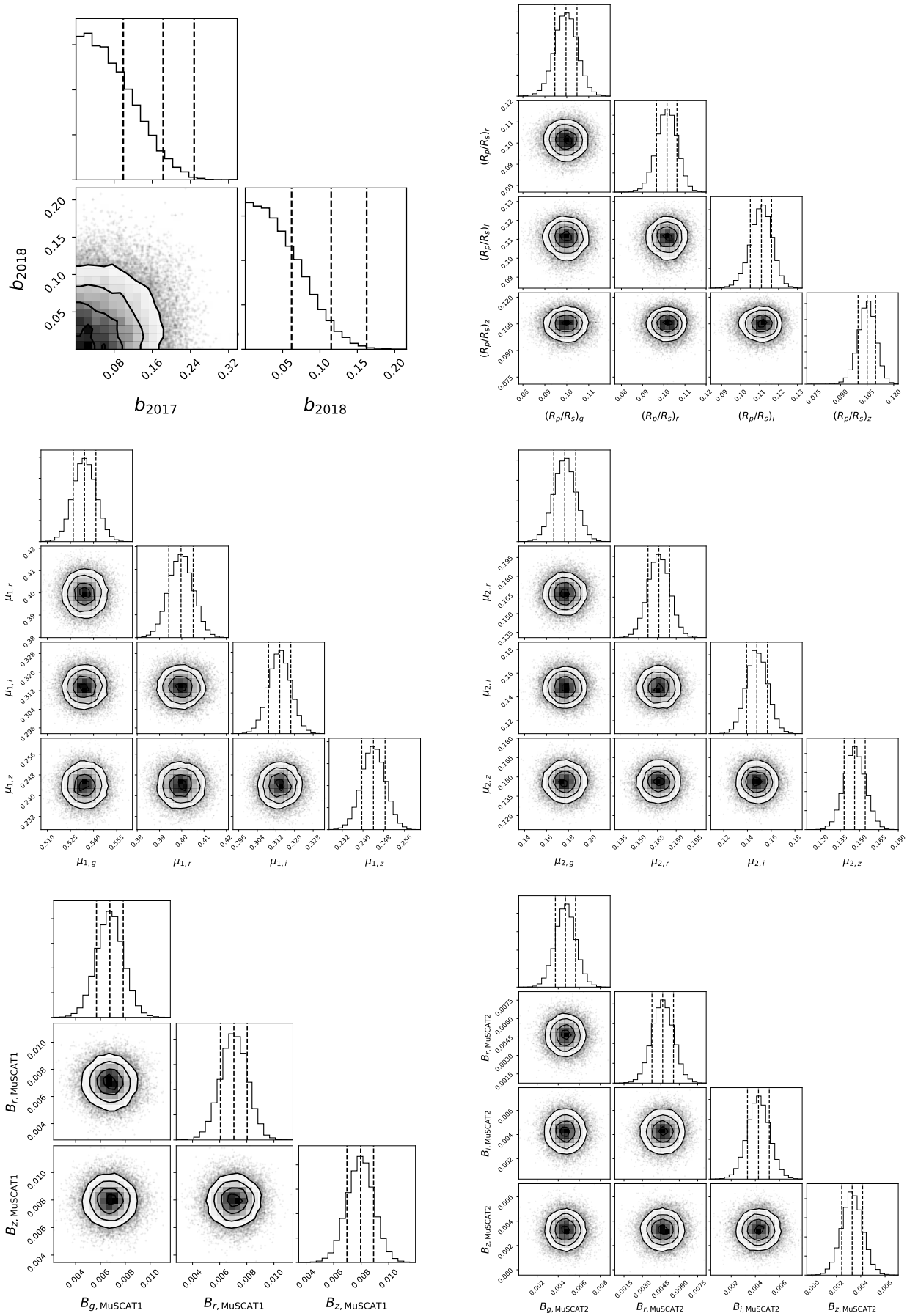

FIGURE 3.3: Same corner plots as Figure 3.2, but for the transit photometry by MuSCAT1 and MuSCAT2. This figure describes plot distributions for impact parameter of each epoch, radial-ratio of each band, limb darkening coefficients of each band and base line of each light curve.

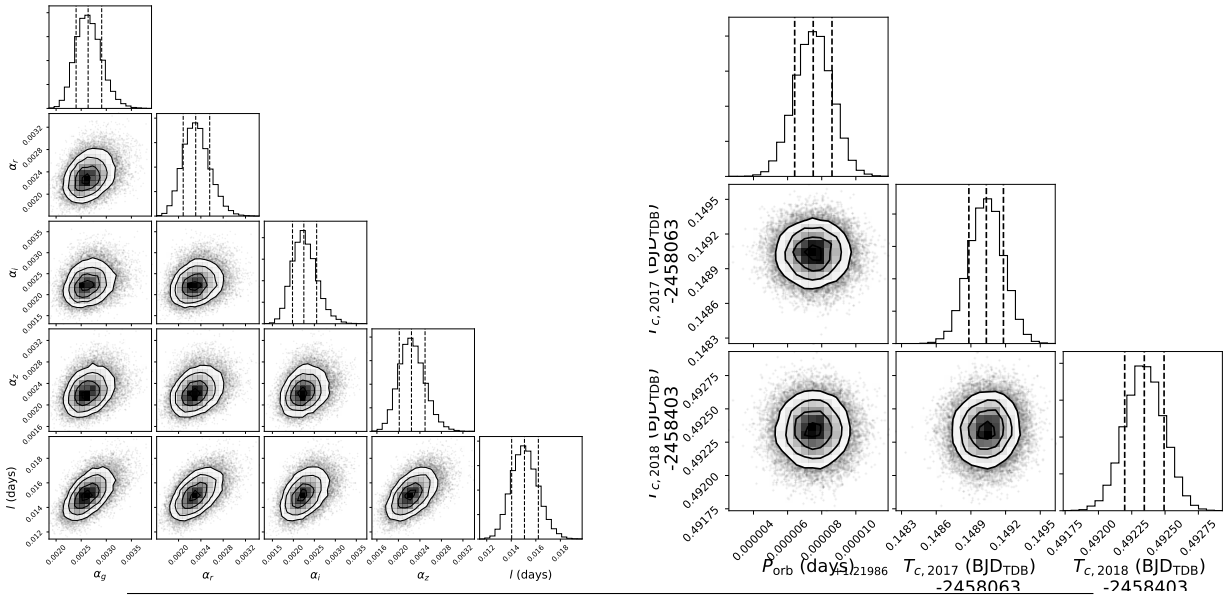

FIGURE 3.4: Continuance of Figure 3.3. This figure describes plot distributions for impact parameter of each epoch, σ of each band, l, period and transit mid-time of each epoch.

where $O_{\mathrm{mes},i}$ is the measured value of λ and b of each epoch, $C_{\mathrm{mod},i}$ is the model value of λ and b, and $\sigma_{\mathrm{mes},i}$ is the uncertainty of the measured λ and b. I concerned that the values b in 2017 and 2018 are zero from Figure 3.3. I ran 20,000 steps, cut off the first 10,000 steps as burn-in, and iterated this set 20 times. The posteriors from MCMC is shown in Figure 3.8 and the values are written in Table 3.2. I exhibit the change of λ and b of WASP-33b in Figure 3.9.

3.4 Results

I show the line profile residuals and the best fitted filtered models in Figure 3.5. The best values of λ and b are listed in Table 3.1. Our results of λ and b in 2014 are in excellent agreement with the values of Johnson et al. (2015), whereas ones in 2008 are marginally consistent with Johnson et al. (2015) within 2σ.

I also display the best fit light curve models in Figure 3.9. The range of b from MuSCAT and MuSCAT2 are written in Table 3.1. The posteriors of both b in Figure 3.3 look like truncated normal distribution with the minimum value ~ 0. Hence, I set 1 σ as a 68% confidence interval from the minimum value 0 because the same values but the opposite signs of impact parameters make the same transit light curves.

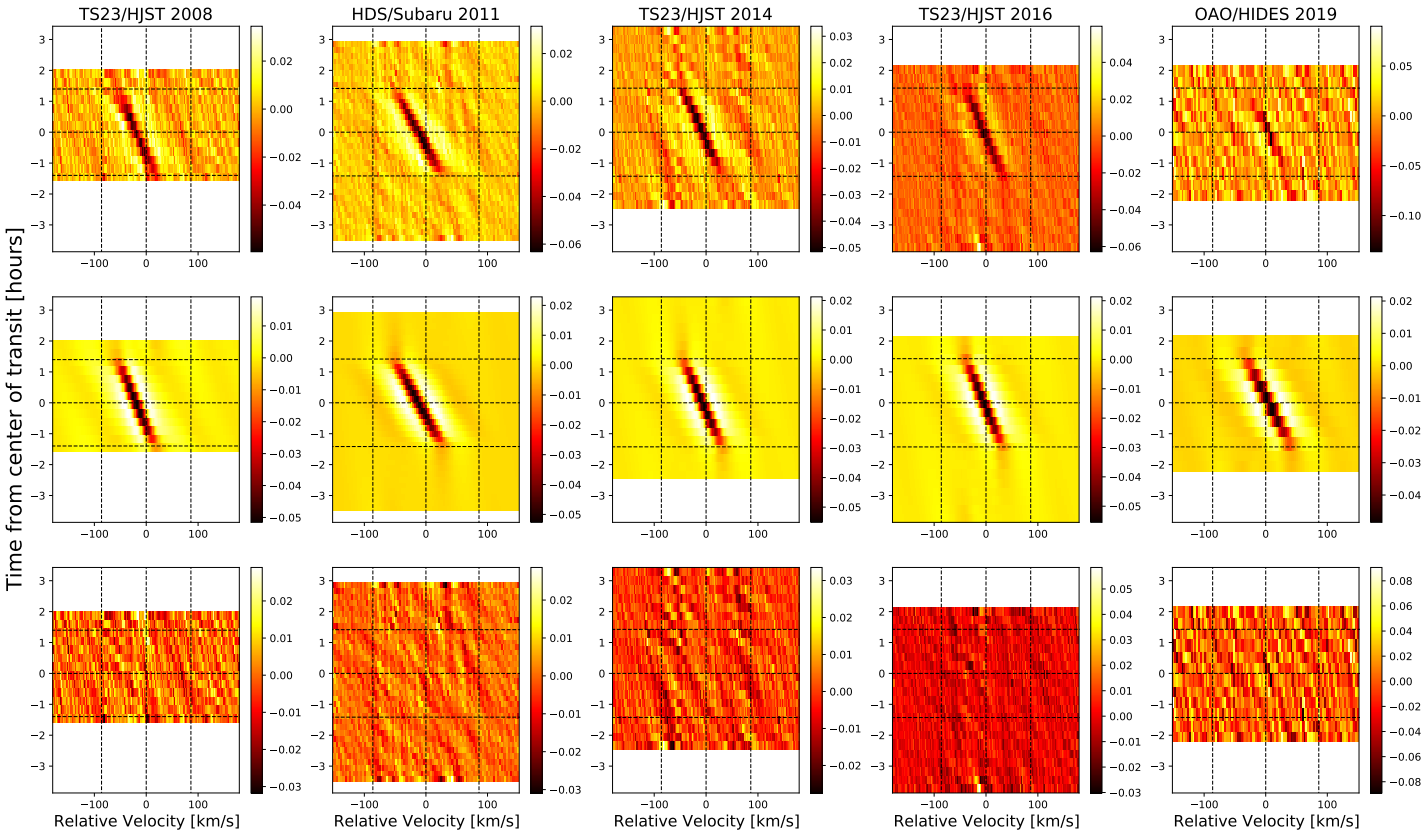

FIGURE 3.5: Fitting for filtered residual data by MCMC. These are the same type of colorscale as ones of the first row in Figure 3.1. First row: residual data remained only a planetary shadow. Second row: filtered models of a planetary shadow using best-fit values. Third row: the difference between the first row and the second row.

TABLE 3.1: Observed Parameters of WASP-33b

Date	λ (deg)	b	$T_c(\mathrm{BJD_{TDB}})$	**Method**
2008 November 12th	-111.30 ± 0.60	$0.2398^{+0.0054}_{-0.0051}$	$2454782.92501^{+0.00017}_{-0.00016}$	Doppler tomography
2011 October 19th	-113.94 ± 0.26	$0.1574^{+0.0023}_{-0.0022}$	$2455853.96859^{+0.00015}_{-0.00014}$	Doppler tomography
2014 October 4th	-112.90 ± 0.30	$0.0847^{+0.0026}_{-0.0025}$	$2456934.77143 \pm 0.00015$	Doppler tomography
2016 December 11th	$-111.22^{+0.41}_{-0.38}$	$0.0436^{+0.0033}_{-0.0031}$	$2457733.78452 \pm 0.00015$	Doppler tomography
2017 November 5th	-	$\lvert b\rvert < 0.099$	$2458063.14903 \pm 0.00015$	Photometry
2018 October 18th	-	$\lvert b\rvert < 0.061$	$2458403.49234 \pm 0.00015$	Photometry
2019 December 27th	$-112.29^{+0.79}_{-0.80}$	$-0.0599^{+0.0052}_{-0.0055}$	$2458845.08379^{+0.00015}_{-0.00016}$	Doppler tomography

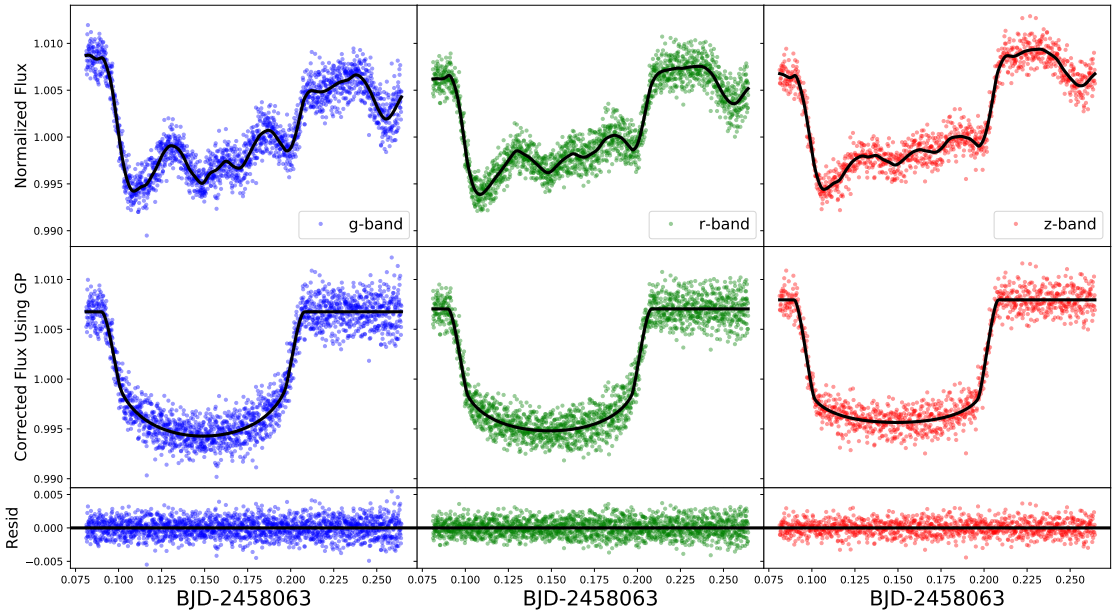

FIGURE 3.6: Light curves of MuSCAT in 2017. Top row: light curves from photometric observation data. the black solid lines are the models from MCMC fitting. Second row: light curves subtracted using Gaussian process. Bottom row: Residuals between the observed data and model data.

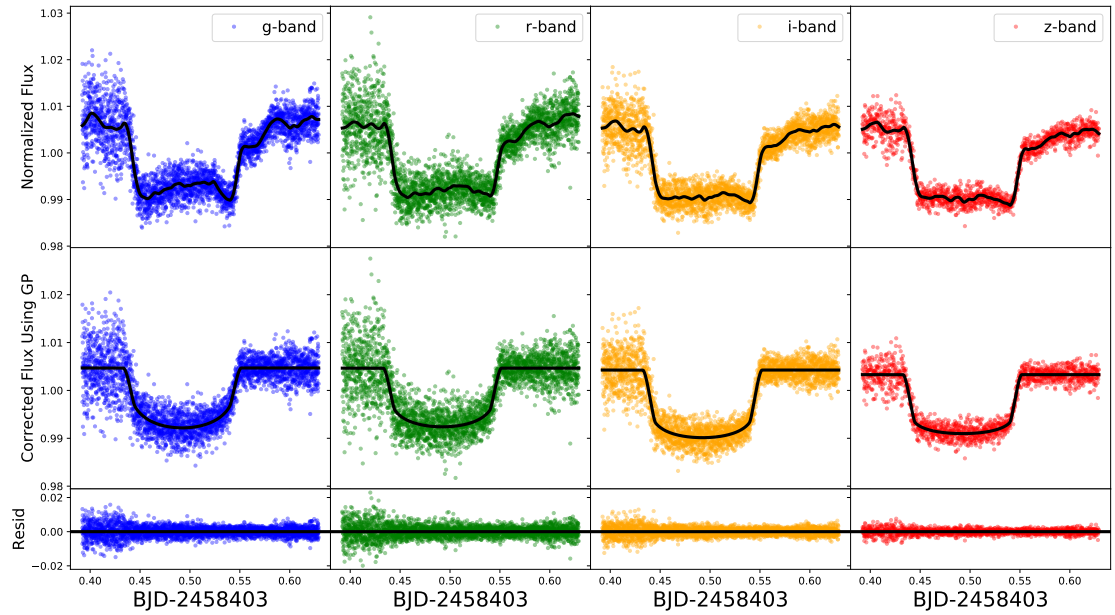

FIGURE 3.7: Similar light curves as Figure 3.6, but for MuSCAT2 data set.

Moreover, I show the posteriors from MCMC with the nodal precession model in Figure 3.8 and the values of ϕ, $\theta(t = 2008)$, i_s and J_2 in Table 3.2. Here I note that Iorio (2016) may have considered ϕ as a variable value. I exhibit the change of λ and b of WASP-33b in Figure 3.9.

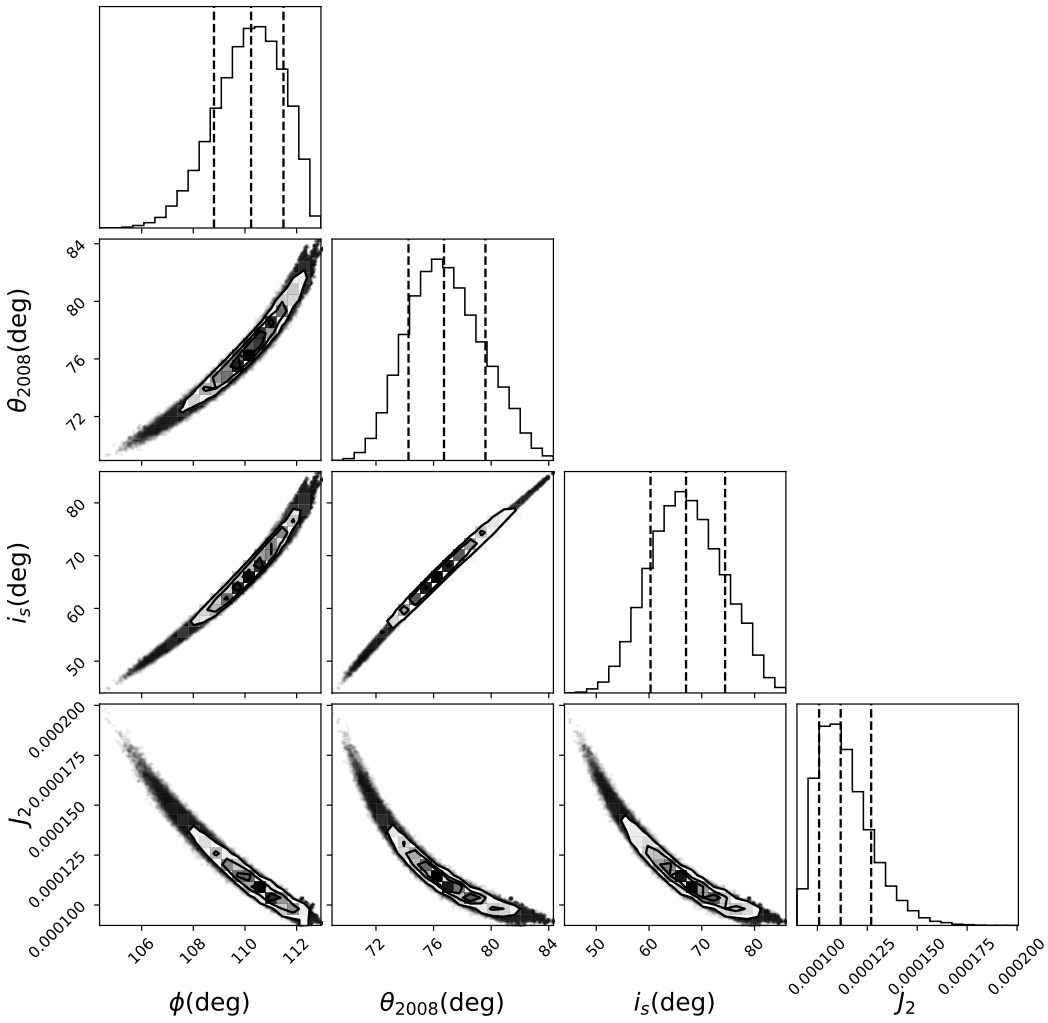

FIGURE 3.8: MCMC corner plots for architecture angles, ϕ, θ_{2008} and i_s, and stellar quadrupole moment J_2 of WASP-33b System

3.5 Discussion

I inspected the nodal precession of WASP-33b by more extended observations than Johnson et al. (2015) and Iorio (2016). It is the first time to verify the nodal precession by Doppler tomographic observation and transit photometry. The errors from

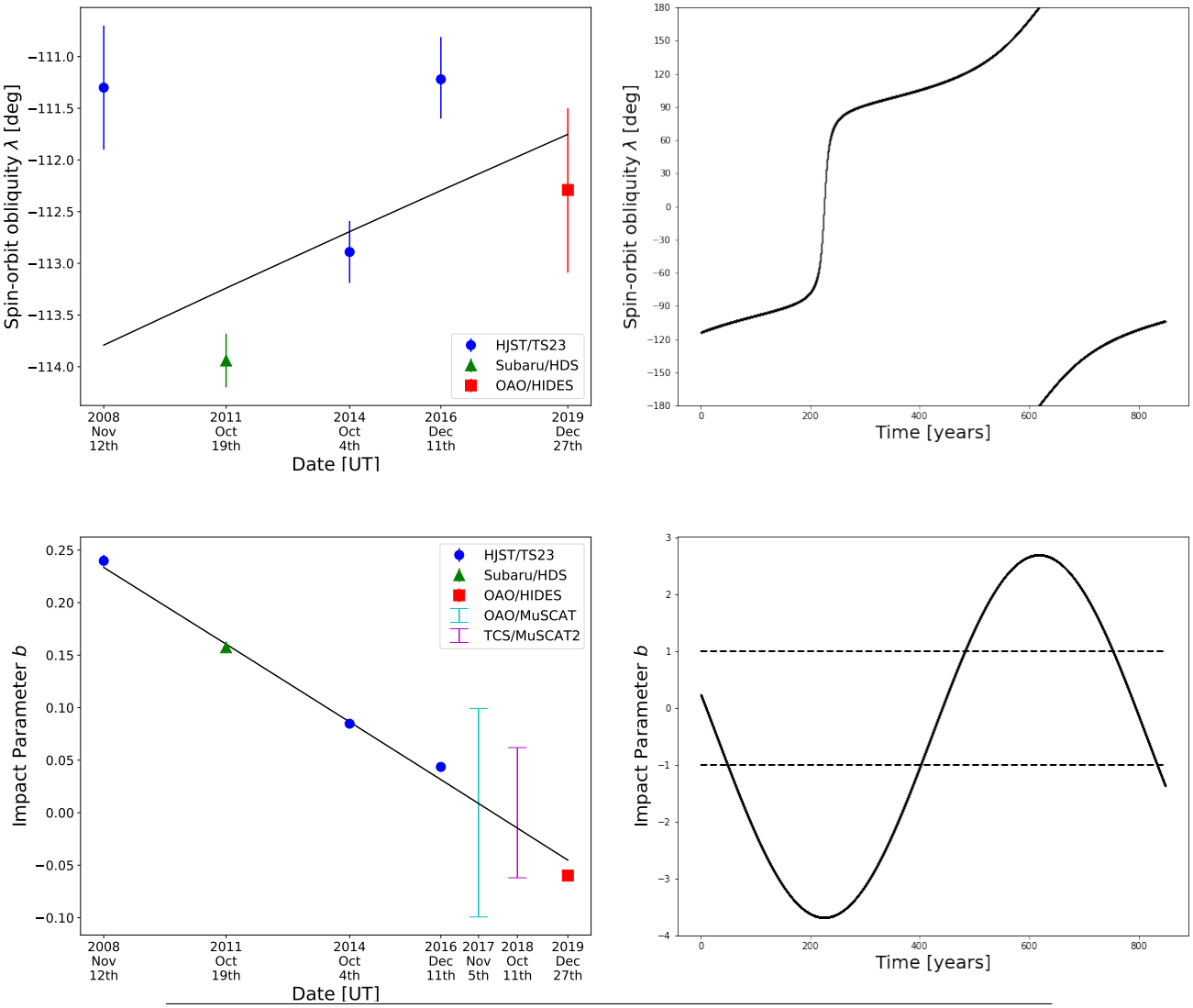

FIGURE 3.9: Changes of λ (upper row) and b (lower row). Left and right column shows the change in short term and long term respectively. The x-axis of left column is time in years from the epoch of 2008. The blue circles show values from the data sets of HJST/TS23, the green triangles are values from Subaru/HDS, the red squares are values from OAO/HIDES, the cyan line is value range from OAO/MuSCAT, the magenta line is value range from TCS/MuSCAT2 and the black solid lines are model. In the right bottom figure, two black dotted lines show edges of a stellar disk of WASP-33b.

TABLE 3.2: Calculated Parameters of WASP-33b

Parameter	Iorio (2016)	Results of This thesis	Fitting with fixed i_s
ϕ (deg)	99^{+5}_{-4} (in 2008)	$110.2^{+1.3}_{-1.4}$	105.26 ± 0.10
	103^{+5}_{-4} (in 2014)		
θ_{2008} (deg)	-	$76.7^{+2.9}_{-2.5}$	104.14 ± 0.15
i_s (deg)	142^{+10}_{-11}	$67.0^{+7.4}_{-6.8}$	142 (fixed)
J_2	$(2.1^{+0.8}_{-0.5}) \times 10^{-4}$	$(1.11^{+0.15}_{-0.11}) \times 10^{-4}$	$(2.118 \pm 0.045) \times 10^{-4}$
$\chi^2_{\rm pre}$	-	57	187

the transit photometric observations are large. However, in the change of impact parameter (See the left bottom part of Figure 3.9), the results from the transit photometry are consistent with the predicted values from decreasing trend from the Doppler tomographic observations. This means that transit photometry can contribute to the measurement of the nodal precession using Doppler tomographic data at the same time.

3.5.1 Verification of Stellar Spin Inclination and Quadrupole Moment

The ϕ and J_2 agrees with one of Iorio (2016) within 3σ. However, i_s disagrees with the previous study within 3σ. Once I tried to calculate ϕ, $\theta(t = 2008)$ and J_2 fixing the value of i_s from Iorio (2016) by the same way as ; The MCMC result and The these values are shown in Figure 3.10 and Table 3.2, respectively. I also display the changes of λ and b in Figure 3.11 with this thesis's result. Although the values of ϕ and J_2 from fitting with fixed i_s agree with those of Iorio (2016) and the uncertainties are smaller than our result, $\chi^2_{\rm pre}$ is larger. Moreover, the λ variation model fits worse than those of our result (see Figure 3.11). This inaccuracy may happen because λ does not vary as Iorio (2016) expected from only two data points. Thus, our values seem to be more accurate than the previous study. To measure more accurate i_s, we need more Doppler tomographic observations to measure λ.

I also derived WASP-33b's stellar quadrupole moment $J_2 = (1.11^{+0.15}_{-0.11}) \times 10^{-4}$. For comparison, the solar value of J_2 is $\sim 2 \times 10^{-7}$. Iorio (2011) calculated the stellar quadrupole moment $J_2 = 3.8 \times 10^{-4}$ in theory by Equation 1.4; Iorio (2011) considers the Love number, as known as the internal structure constant, for WASP-33 is $k_2 =$

0.03 from Claret and Gimenez (1995). Comparing these values, this result shows that observed WASP-33's shape is more spherical than the model. From Equation 1.4 This difference is possibly due to the actual WASP-33b's internal structure constant that is less than 0.03; which indicates that WASP-33 is slightly more rigid than that in theory by Claret and Gimenez (1995).

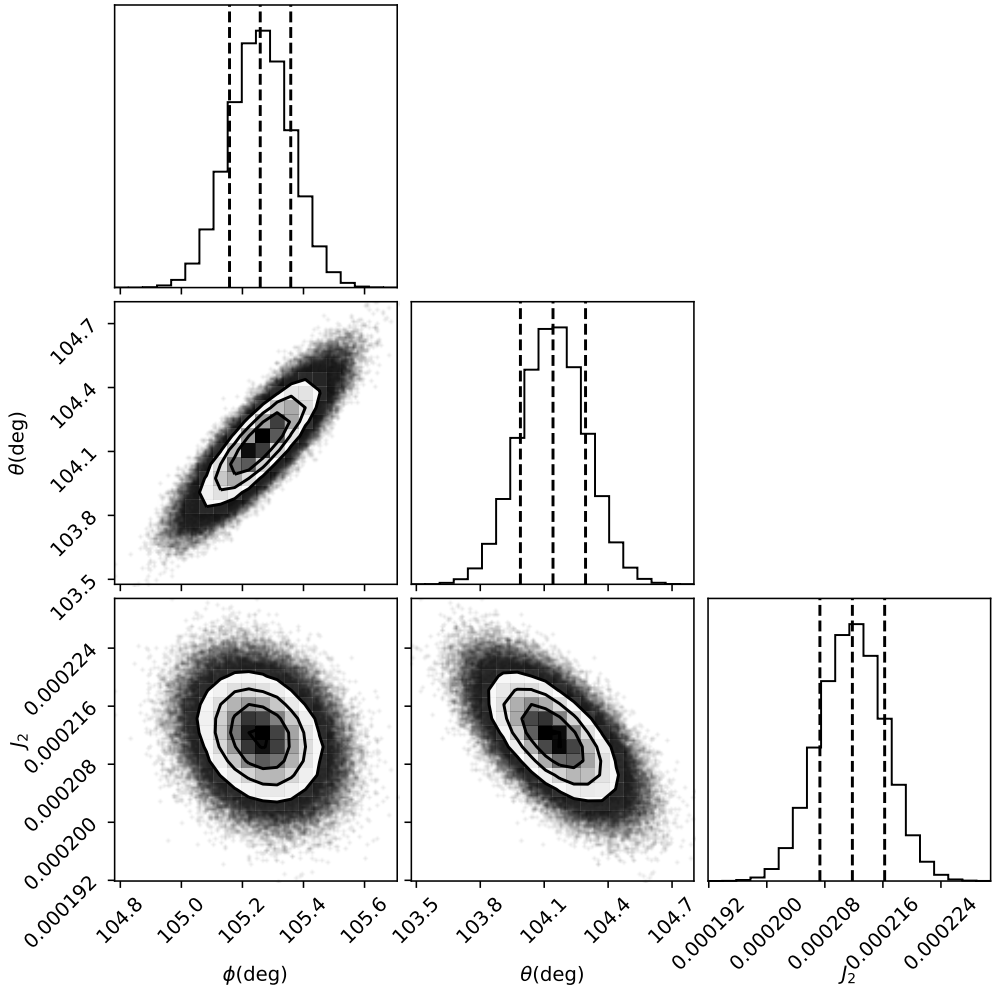

FIGURE 3.10: MCMC corner plots for architecture angles, ϕ, θ_{2008}, and stellar quadrupole moment J_2 of WASP-33b system.

3.5.2 Nodal Precession with Eccentricity

In the calculation of the nodal precession of WASP-33b, I estimated its orbit completely circle because the age of WASP-33b (∼100 Myrs; Moya et al., 2011) is enough to have already undergone the tidal circularization, whose timescale is ∼ 1.72 Myrs

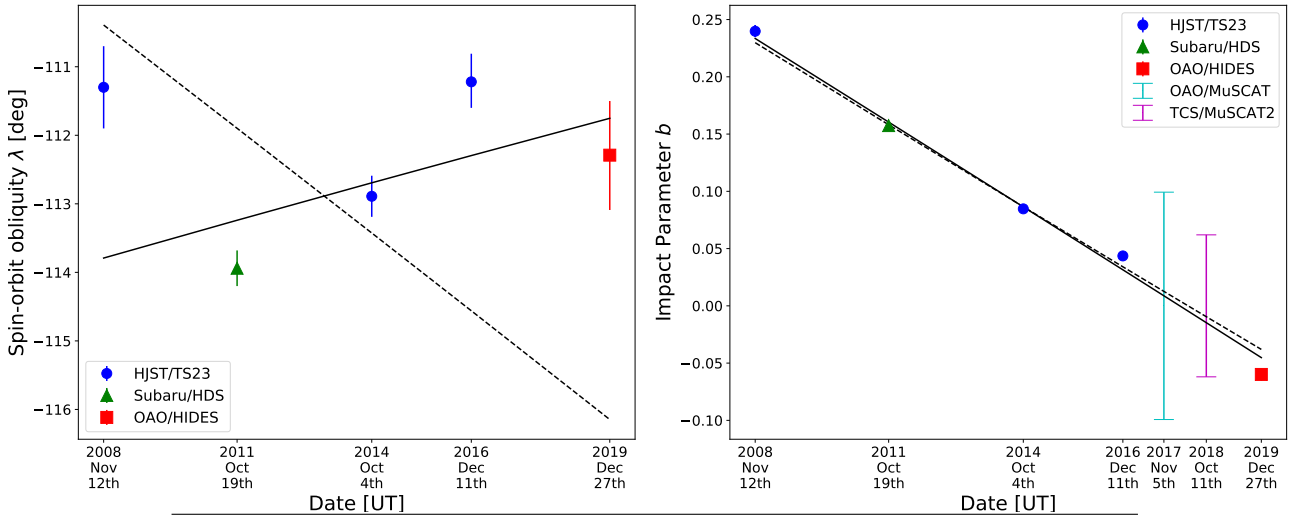

FIGURE 3.11: The same graphs as the left column of Figure 3.9, but including the model with fixing i_s showing as dashed lines

(Smith et al., 2011). There is the fact that no one has measured its value yet. Lehmann et al. (2015) derived RV's change by this hot Jupiter, and its shape looked like from the circular orbit. Considering the eccentricity, the nodal precession's speed, the slope part of Equation 3.6, become

$$\dot{\theta} = \frac{3\pi J_2 R_s^2 \cos\phi}{P_{\rm orb} a^2 (1-e^2)^2} \tag{3.8}$$

from Equation 10 of Iorio (2016). When the exact value of WASP-33b's eccentricity is clear, we can expect that the nodal precession becomes slightly faster; the speed when $e = 0.1$ is ~ 1.02 times as fast as the circular orbit.

If the eccentricity is not a fixed parameter for the parameter fitting in Section 3.3, comparing with Equation 3.8 and the slope of Equation 3.6, the best-fit value of $J_2/(1-e^2)^2$ in Equation 3.8 is probably similar to that of J_2 in Equation 3.6. However, determining the best-fit values of J_2 and e is difficult from that of $J_2/(1-e^2)^2$. Thus, another way to derive e, RV observation for instance, is needed to derive J_2 with an eccentric planet.

3.5.3 Orbital Evolution of WASP-33b

I found the real spin-orbit obliquity of WASP-33b $\phi = 110.2^{+1.3}_{-1.4}$ deg and could reduce the uncertainty thanks to dealing with more data than Johnson et al. (2015).

Our value of ϕ is slightly close to the ones of projected spin-orbit obliquities $|\lambda|$. The derived value indicates the possibility that WASP-33b has undergone the mechanisms which makes the orbit misaligned easily (e.g. planet-planet scattering or Kozai migration). Because the absolute value of our ϕ is slightly larger than one of Iorio (2016), it has a little possibility that WASP-33b may have evolved by Kozai migration than planet-planet scattering according to the histograms in Section 1.2.4 and 1.2.5. The existence of WASP-33b's companion star is necessary to distinguish these two evolution models clearly. Nevertheless, Doppler tomographic observations and transit photometry cannot detect the companion star.

Moya et al. (2011) found a companion candidate estimated a dwarf star or brown dwarf, located at 227 AU ($P_{\rm orb} \sim 2,200$ yrs) from the host star by direct imaging. SEEDS project (Tamura, 2016) also detected the companion candidate by High Contrast Instrument for the Subaru Next Generation Adaptive Optics (HiCIAO) on Subaru telescope (see Figure 3.12). However, it is not confirmed as a companion star yet due to the lack of its proper motion. Thus, one more direct imaging observation is essential to confirm whether the companion moves in the same proper motion as the host star or not. If the stellar companion candidate with 0.1 $M_\star$ revolves in a circular orbit ($e = 0$) and WASP-33b has been formed near the snow line, $\sim$ 5 AU ($P_{\rm orb} \sim 12$ yrs), the planet has undergone a Kozai oscillation with the Kozai cycle period $P_{\rm Kozai} \sim 6$ Myrs following Equation 3.9,

$$P_{\rm Kozai} = \frac{M_s P_c^2}{M_c P_b}(1 - e_c^2)^{3/2}, \tag{3.9}$$

where M_s, M_c, P_c, P_b and e_c are the stellar mass, the companion's mass, the companion's period, the planetary mass and the companion's eccentricity, respectively (Wu, Murray, and Ramsahai, 2007). Though we have to be aware that the distance from the host star to the companion star is the sky-projected one and the eccentricity of the companion star may exist, the Kozai cycle period can be shorter than the age of WASP-33 ($\sim$ 100 Myrs). Therefore, if the companion candidate is confirmed, the stellar companion have had the possibility of causing Kozai mechanism of WASP-33b.

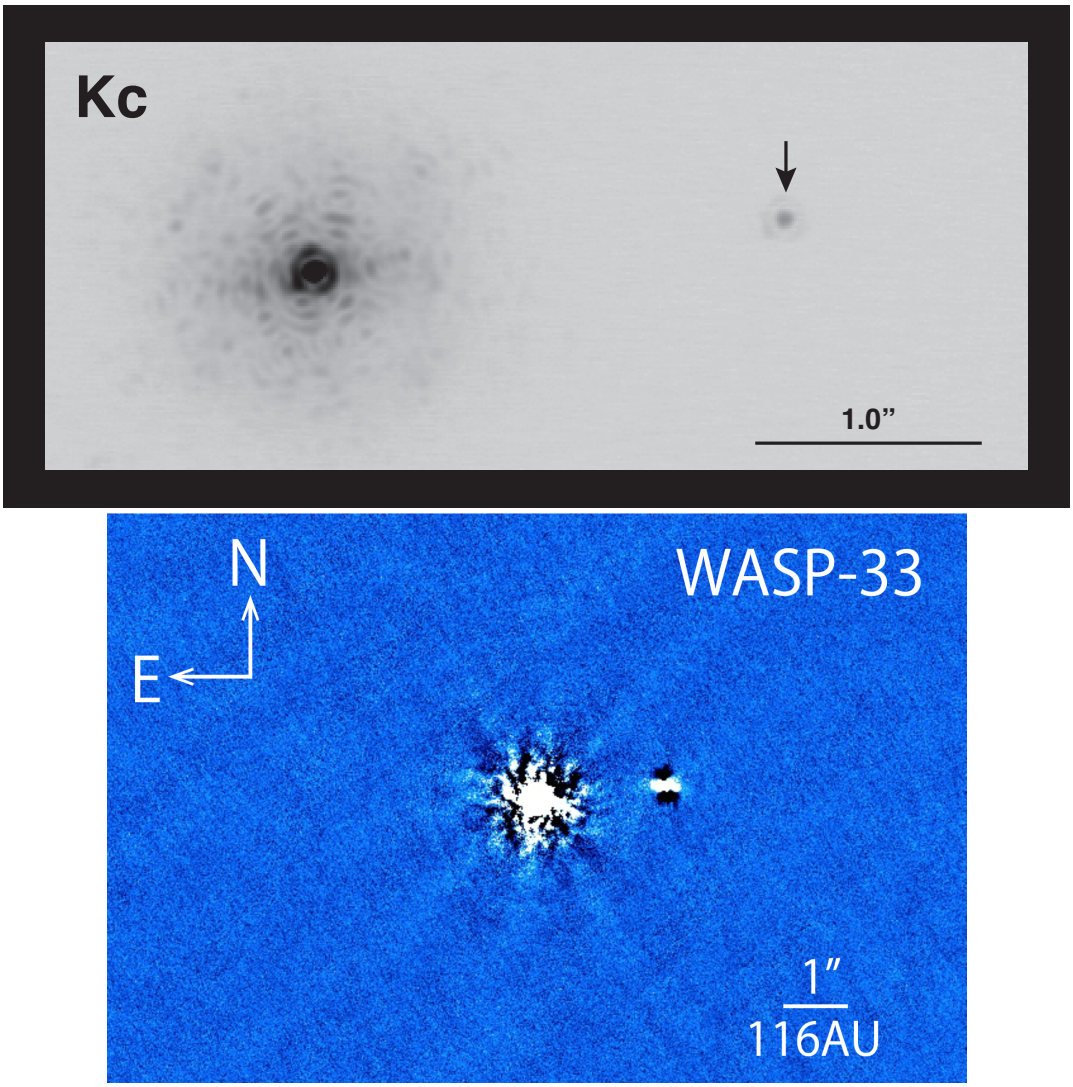

FIGURE 3.12: Top: Direct imaging of WASP-33b from Keck-II/NIRC2 in the K-band (Moya et al., 2011). The vector points a companion candidate star while the largest dark image shows the host star. Bottom: Direct imaging of WASP-33b from HiCHAO/Subaru (Tamura, 2016). Takahashi, 2014 analyzed this image and Ryu, 2018 used this data. The white circle locates the position of the host star and the image showing in the right side is the companion star.

3.5.4 Nodal Precession Speed

From the slope of Equation 3.6, I also calculated the nodal precession speed $\dot{\theta} = 0.458^{+0.027}_{-0.020}$ deg year^{-1} and its period $P_{\rm pre} = 785^{+36}_{-44}$ years; the precession is faster than one from Iorio (2016) ($\dot{\theta} = 0.37^{+0.04}_{-0.03}$). Then I found that WASP-33b transits in front of the host star for only $\sim$ 20 % of the whole nodal precession period, which means that it is rare to discover WASP-33b as a transit. This implies that WASP-33b began to transit in 1976 ± 2 and stop to transit in 2057 ± 2. Therefore, we can observe its transit until 40 years later.

Chapter 4

Conclusion

I have presented the observations to detect the nodal precession of hot Jupiters around hot stars and the derivation of spin-orbit obliquities via measuring nodal precessions.

I confirmed the WASP-33b's more accurately and more precisely than the previous study Johnson et al. (2015) using various high spectrograph instruments, Subaru/HDS, HJST/TS23, OAO/HIDES, and two simultaneous cameras, OAO/MuSCAT and TCS/MuSCAT2. I established how to observe planetary nodal precession using two methods, Doppler tomography and transit photometry.

I acquired the method to measure the real spin-orbit obliquity of WASP-33b $\phi = 110.2^{+1.3}_{-1.4}$ from the nodal precession. This measurement will help calculate the real spin-orbit obliquity and make its *real* distribution. Therefore, this research is the first step to make the distribution of spin-orbit obliquity, which may have the potential to determine the evolution trend of hot Jupiters more accurately.

I also derived the stellar quadrupole moment of WASP-33b $J_2 = (1.11^{+0.15}_{-0.11}) \times 10^{-4}$ from the observation of its nodal precession at the same time. WASP-33 has the propability that WASP-33's internal structure is slightly different than that estimated from the method in Claret and Gimenez (1995). The measurement of J_2 may be a clue to search the internal structure of hot stars.

4.1 Future Plans

4.1.1 Nodal Precession Observation of Other Confirmed Hot Jupiters

There are 16 confirmed hot Jupiters around hot stars by Doppler tomography. Four of them disclose their real spin-orbit obliquities (WASP-33b, Kepler-13Ab, MASCARA-4b, and WASP-189b): the rest of them reveal only their projected one.

For hot Jupiters with near-polar orbits, KELT-9b, KELT-17b, MASCARA-1b, HAT-P-70b, and WASP-178b have a possibility of their observable nodal precessions. Even if λ is near 0 deg or 180 deg, we can observe the change of transit trajectory and measure ϕ close to 90 deg when the star rotates nearly pole-on for the line of sight. On the other hand, when λ is near 0 or 180 deg and the star rotation axis is almost perpendicular to the line of sight, the transit trajectory moves scarcely because ϕ should also be near 0 deg or 180 deg. In this case, we can estimate ϕ as λ. Therefore, we should observe their nodal precessions around hot stars regularly to measure their ϕ by Doppler tomography and transit photometry.

Kepler-13Ab, orbiting around an A-type star, is the other hot Jupiter whose nodal precession detected by only transit photometries (Szabó et al., 2011 and Barnes, Linscott, and Shporer, 2011). Other previous studies measured ϕ of this hot Jupiter by gravity-darkened transit photometry, but the values are different between these two results ($\phi = 60 \pm 2$ deg in Masuda, 2015 and $\phi = 29 \pm 1$ deg in Herman et al., 2018). Even though Kepler-13Ab is likely to have evolved with Kozai migration due to its companion star, Kepler-13B (Santerne et al., 2012), we have to double-check the value of its ϕ by adding Doppler tomographic observations and transit photometries for the proper histogram of derived ϕ. Because Johnson et al. (2014) measured Kepler-13Ab's λ on 2014 by Doppler tomography, one more transit spectroscopic observation can be detected the change of λ then derive its ϕ independently to the gravity-darkened transit photometry.

Ahlers et al., 2020 measured ϕ of MASCARA-4b by gravity-darkened transit photometry ($\phi = 104^{+7}_{-13}$ deg). Lendl et al., 2020 also did the same observation for ϕ of WASP-189b ($\phi = 85.4 \pm 4.3$ deg). These planets are hot Jupiters around A-type stars. In fact, no one has detected their nodal precessions yet. Observing the nodal precessions of MASCARA-4b and WASP-189b is important to crosscheck the values of

their ϕ.

4.1.2 Confirmation of Hot Jupiter

Even though there are 16 hot Jupiters around hot stars whose spin-orbit obliquities are measured and their obliquities tend to have a wide range, the number of those is still few to determine the orbital evolution tendency. If normal planet-disk interaction is the main migration, the distribution should gather at $\phi = 0$ deg (Lai, Foucart, and Lin, 2011). If the orbital evolution by planet-planet scattering is the majority, the orbits are likely to incline about $\phi = 60$ (Nagasawa and Ida, 2011). When Kozai migration is the primary evolution, ϕ takes a wide range from 10 deg to 140 deg (Petrovich, 2015). Barclay, Pepper, and Quintana (2018) predicted the TESS mission could find 500 hot Jupiters around A-type stars for the two-year-observation. Thus, I will increase the number of hot Jupiter samples around hot stars by validating a TESS candidate to contribute to the ϕ distribution in detail.

Bibliography

Abt, H. A., H. Levato, and M. Grosso (July 2002). "Rotational Velocities of B Stars". In: 573, pp. 359–365. DOI: 10.1086/340590.

Ahlers, John P. et al. (Jan. 2020). "Gravity-darkening Analysis of the Misaligned Hot Jupiter MASCARA-4 b". In: 888.2, 63, p. 63. DOI: 10.3847/1538-4357/ab59d0. arXiv: 1911.05025 [astro-ph.EP].

Albrecht, Simon et al. (Sept. 2012). "Obliquities of Hot Jupiter Host Stars: Evidence for Tidal Interactions and Primordial Misalignments". In: 757.1, 18, p. 18. DOI: 10.1088/0004-637X/757/1/18. arXiv: 1206.6105 [astro-ph.SR].

Bakos, G. Á. et al. (Sept. 2002). "System Description and First Light Curves of the Hungarian Automated Telescope, an Autonomous Observatory for Variability Search". In: 114.799, pp. 974–987. DOI: 10.1086/342382. arXiv: astro-ph/0206001 [astro-ph].

Bakos, G. ¥'A. et al. (2012). "HAT-P-34b-HAT-P-37b: FOUR TRANSITING PLANETS MORE MASSIVE THAN JUPITER ORBITING MODERATELY BRIGHT STARS". In: *The Astronomical Journal* 144.1, p. 19. DOI: 10.1088/0004-6256/144/1/19. URL: https://doi.org/10.1088/0004-6256/144/1/19.

Barclay, Thomas, Joshua Pepper, and Elisa V. Quintana (Nov. 2018). "A Revised Exoplanet Yield from the Transiting Exoplanet Survey Satellite (TESS)". In: 239.1, 2, p. 2. DOI: 10.3847/1538-4365/aae3e9. arXiv: 1804.05050 [astro-ph.EP].

Barge, P. et al. (Dec. 2005). "CoRoT: a first space mission to find terrestrial planets". In: *SF2A-2005: Semaine de l'Astrophysique Francaise*. Ed. by F. Casoli et al., p. 193.

Barker, Adrian J. and Gordon I. Ogilvie (June 2009). "On the tidal evolution of Hot Jupiters on inclined orbits". In: 395.4, pp. 2268–2287. DOI: 10.1111/j.1365-2966.2009.14694.x. arXiv: 0902.4563 [astro-ph.EP].

Barnes, Jason W. (Nov. 2009). "Transit Lightcurves of Extrasolar Planets Orbiting Rapidly Rotating Stars". In: 705.1, pp. 683–692. DOI: 10.1088/0004-637X/705/1/683. arXiv: 0909.1752 [astro-ph.EP].

Barnes, Jason W., Ethan Linscott, and Avi Shporer (Nov. 2011). "Measurement of the Spin-Orbit Misalignment of KOI-13.01 from Its Gravity-darkened Kepler Transit Lightcurve". In: 197.1, 10, p. 10. DOI: 10.1088/0067-0049/197/1/10. arXiv: 1110.3514 [astro-ph.EP].

Barnes, Jason W. et al. (Sept. 2013). "Measurement of Spin-orbit Misalignment and Nodal Precession for the Planet around Pre-main-sequence Star PTFO 8-8695 from Gravity Darkening". In: 774.1, 53, p. 53. DOI: 10.1088/0004-637X/774/1/53. arXiv: 1308.0629 [astro-ph.EP].

Bate, M. R., G. Lodato, and J. E. Pringle (Jan. 2010). "Chaotic star formation and the alignment of stellar rotation with disc and planetary orbital axes". In: 401, pp. 1505–1513. DOI: 10.1111/j.1365-2966.2009.15773.x. arXiv: 0909.4255 [astro-ph.SR].

Beck, J. G. and P. Giles (Mar. 2005). "Helioseismic Determination of the Solar Rotation Axis". In: 621, pp. L153–L156. DOI: 10.1086/429224.

Bessell, M. S., F. Castelli, and B. Plez (May 1998). "Model atmospheres broad-band colors, bolometric corrections and temperature calibrations for O - M stars". In: 333, pp. 231–250.

Borucki, William J. et al. (Feb. 2010). "Kepler Planet-Detection Mission: Introduction and First Results". In: *Science* 327.5968, p. 977. DOI: 10.1126/science.1185402.

Boss, A. P. (Jan. 1997). "Giant planet formation by gravitational instability." In: *Science* 276, pp. 1836–1839. DOI: 10.1126/science.276.5320.1836.

Bouvier, J. et al. (Jan. 2007). "Magnetospheric Accretion in Classical T Tauri Stars". In: *Protostars and Planets V*. Ed. by Bo Reipurth, David Jewitt, and Klaus Keil, p. 479. arXiv: astro-ph/0603498 [astro-ph].

Brown, D. J. A. et al. (Dec. 2012). "Analysis of Spin-Orbit Alignment in the WASP-32, WASP-38, and HAT-P-27/WASP-40 Systems". In: 760, 139, p. 139. DOI: 10.1088/0004-637X/760/2/139. arXiv: 1303.5649 [astro-ph.EP].

Cameron, A. G. W. (Feb. 1978). "Physics of the Primitive Solar Accretion Disk". In: *Moon and Planets* 18.1, pp. 5–40. DOI: 10.1007/BF00896696.

Campbell, B. et al. (Dec. 1979). "Precision Radial Velocities with the Hydrogen Fluoride Absorption Cell". In: *Bulletin of the American Astronomical Society*. Vol. 11. P. 647.

Cantiello, Matteo and Jonathan Braithwaite (Sept. 2019). "Envelope Convection, Surface Magnetism, and Spots in A and Late B-type Stars". In: 883.1, 106, p. 106. DOI: 10.3847/1538-4357/ab3924. arXiv: 1904.02161 [astro-ph.SR].

Charbonneau, David et al. (Jan. 2000). "Detection of Planetary Transits Across a Sun-like Star". In: 529.1, pp. L45–L48. DOI: 10.1086/312457. arXiv: astro-ph/9911436 [astro-ph].

Chatterjee, S. et al. (Oct. 2008). "Dynamical Outcomes of Planet-Planet Scattering". In: 686, 580-602, pp. 580–602. DOI: 10.1086/590227. eprint: astro-ph/0703166.

Claret, A. and A. Gimenez (Dec. 1995). "Stellar models for a wide range of initial chemical compositions until helium burning. II. From X=0.63 to X=0.80, for Z=0.01." In: 114, p. 549.

Collier Cameron, A. et al. (Mar. 2007). "WASP-1b and WASP-2b: two new transiting exoplanets detected with SuperWASP and SOPHIE". In: 375, pp. 951–957. DOI: 10.1111/j.1365-2966.2006.11350.x. eprint: astro-ph/0609688.

Collier Cameron, A. et al. (Mar. 2010a). "Line-profile tomography of exoplanet transits - I. The Doppler shadow of HD 189733b". In: 403, pp. 151–158. DOI: 10.1111/j.1365-2966.2009.16131.x. arXiv: 0911.5361 [astro-ph.SR].

Collier Cameron, A. et al. (Sept. 2010b). "Line-profile tomography of exoplanet transits - II. A gas-giant planet transiting a rapidly rotating A5 star". In: 407, pp. 507–514. DOI: 10.1111/j.1365-2966.2010.16922.x. arXiv: 1004.4551 [astro-ph.EP].

Colón, Knicole D., Eric B. Ford, and Robert C. Morehead (Oct. 2012). "Constraining the false positive rate for Kepler planet candidates with multicolour photometry from the GTC". In: 426.1, pp. 342–353. DOI: 10.1111/j.1365-2966.2012.21711.x. arXiv: 1207.2481 [astro-ph.EP].

Donati, J.-F. et al. (Nov. 1997). "Spectropolarimetric observations of active stars". In: 291, p. 658. DOI: 10.1093/mnras/291.4.658.

Eastman, J., R. Siverd, and B. S. Gaudi (Aug. 2010). "Achieving Better Than 1 Minute Accuracy in the Heliocentric and Barycentric Julian Dates". In: 122, p. 935. DOI: 10.1086/655938. arXiv: 1005.4415 [astro-ph.IM].

Fabrycky, D. and S. Tremaine (Nov. 2007). "Shrinking Binary and Planetary Orbits by Kozai Cycles with Tidal Friction". In: 669, pp. 1298–1315. DOI: 10.1086/521702. arXiv: 0705.4285.

Fekel, Francis C., Phillip B. Warner, and Anthony B. Kaye (Apr. 2003). "Spectroscopy of Early F Stars: γ Doradus Candidates and Possible Metallic Shell Stars". In: 125.4, pp. 2196–2214. DOI: 10.1086/368239.

Foreman-Mackey, D. et al. (Mar. 2013). "emcee: The MCMC Hammer". In: 125, p. 306. DOI: 10.1086/670067. arXiv: 1202.3665 [astro-ph.IM].

Foreman-Mackey, Daniel (2016). "corner.py: Scatterplot matrices in Python". In: *The Journal of Open Source Software* 24. DOI: 10.21105/joss.00024. URL: http://dx.doi.org/10.5281/zenodo.45906.

Foreman-Mackey, Daniel et al. (Oct. 2020). *exoplanet-dev/exoplanet v0.4.0*. DOI: 10.5281/zenodo.1998447. URL: https://doi.org/10.5281/zenodo.1998447.

Fukui, Akihiko et al. (Feb. 2011). "Measurements of Transit Timing Variations for WASP-5b". In: 63, p. 287. DOI: 10.1093/pasj/63.1.287. arXiv: 1009.5769 [astro-ph.EP].

Fukui, Akihiko et al. (Dec. 2016). "Ground-based Transit Observation of the Habitable-zone Super-Earth K2-3d". In: 152.6, 171, p. 171. DOI: 10.3847/0004-6256/152/6/171. arXiv: 1610.01333 [astro-ph.EP].

Gaige, Yves (Mar. 1993). "Stellar rotational velocities from the V sin i observations : inversion procedures and applications to open clusters." In: 269, pp. 267–281.

Galvagni, M. and L. Mayer (Jan. 2014). "Early evolution of clumps formed via gravitational instability in protoplanetary discs: precursors of Hot Jupiters?" In: 437.3, pp. 2909–2921. DOI: 10.1093/mnras/stt2108.

Gaudi, B. S. and J. N. Winn (Jan. 2007). "Prospects for the Characterization and Confirmation of Transiting Exoplanets via the Rossiter-McLaughlin Effect". In: 655, pp. 550–563. DOI: 10.1086/509910. eprint: astro-ph/0608071.

Hartman, J. D. et al. (Dec. 2015). "HAT-P-57b: A Short-period Giant Planet Transiting a Bright Rapidly Rotating A8V Star Confirmed Via Doppler Tomography". In: 150, 197, p. 197. DOI: 10.1088/0004-6256/150/6/197. arXiv: 1510.08839 [astro-ph.EP].

Hayashi, C., K. Nakazawa, and Y. Nakagawa (1985). "Formation of the solar system". In: *Protostars and Planets II*. Ed. by D. C. Black and M. S. Matthews, pp. 1100–1153.

Hébrard, G. et al. (June 2010). "Observation of the full 12-hour-long transit of the exoplanet HD 80606b. Warm-Spitzer photometry and SOPHIE spectroscopy". In: 516, A95, A95. DOI: 10.1051/0004-6361/201014327. arXiv: 1004.0790 [astro-ph.EP].

Hébrard, G. et al. (Sept. 2011). "Transiting exoplanets from the CoRoT space mission. XVIII. CoRoT-18b: a massive hot Jupiter on a prograde, nearly aligned orbit". In: 533, A130, A130. DOI: 10.1051/0004-6361/201117192. arXiv: 1107.2032 [astro-ph.EP].

Herman, M. K. et al. (Jan. 2018). "SpinOrbit Misalignment and Precession in the Kepler-13Ab Planetary System". In: 155, 13, p. 13. DOI: 10.3847/1538-3881/aa991f. arXiv: 1711.02681 [astro-ph.EP].

Herrero, E. et al. (Feb. 2011). "WASP-33: the first δ Scuti exoplanet host star". In: 526, L10, p. L10. DOI: 10.1051/0004-6361/201015875. arXiv: 1010.1173 [astro-ph.EP].

Hirano, Teruyuki et al. (Dec. 2011). "Further Observations of the Tilted Planet XO-3: A New Determination of Spin-Orbit Misalignment, and Limits on Differential Rotation". In: 63.6, pp. L57–L61. DOI: 10.1093/pasj/63.6.L57. arXiv: 1108.4493 [astro-ph.EP].

Hirano, Teruyuki et al. (Feb. 2020). "Evidence for SpinOrbit Alignment in the TRAPPIST-1 System". In: 890.2, L27, p. L27. DOI: 10.3847/2041-8213/ab74dc. arXiv: 2002.05892 [astro-ph.EP].

Huang, C. X., C. Petrovich, and E. Deibert (May 2017). "Dynamically Hot Super-Earths from Outer Giant Planet Scattering". In: 153, 210, p. 210. DOI: 10.3847/1538-3881/aa67fb. arXiv: 1609.08110 [astro-ph.EP].

Husser, T.-O. et al. (2013). "Astrophysics A new extensive library of PHOENIX stellar atmospheres". In: *A&A* 553, A6. DOI: 10.1051/0004-6361/201219058.

Ida, Shigeru et al. (Sept. 2018). "Slowing Down Type II Migration of Gas Giants to Match Observational Data". In: 864.1, 77, p. 77. DOI: 10.3847/1538-4357/aad69c. arXiv: 1807.10871 [astro-ph.EP].

Iorio, L. (Feb. 2011). "Classical and relativistic node precessional effects in WASP-33b and perspectives for detecting them". In: 331, pp. 485–496. DOI: 10.1007/s10509-010-0468-x. arXiv: 1006.2707 [gr-qc].

— (Jan. 2016). "Accurate characterization of the stellar and orbital parameters of the exoplanetary system WASP-33 b from orbital dynamics". In: 455, pp. 207–213. DOI: 10.1093/mnras/stv2328. arXiv: 1508.06231 [gr-qc].

Ivanov, P. B. and J. C. B. Papaloizou (Apr. 2007). "Dynamic tides in rotating objects: orbital circularization of extrasolar planets for realistic planet models". In: 376.2, pp. 682–704. DOI: 10.1111/j.1365-2966.2007.11463.x. arXiv: astro-ph/0512150 [astro-ph].

Izumiura, H. (Dec. 1999). "HIDES: a high dispersion echelle spectrograph." In: *Publications of the Yunnan Observatory*, pp. 77–81.

Jackson, Brian, Richard Greenberg, and Rory Barnes (May 2008). "Tidal Evolution of Close-in Extrasolar Planets". In: 678.2, pp. 1396–1406. DOI: 10.1086/529187. arXiv: 0802.1543 [astro-ph].

Jacob, W. S. (June 1855). "On certain Anomalies presented by the Binary Star 70 Ophiuchi". In: 15, p. 228. DOI: 10.1093/mnras/15.9.228.

Johnson, M. C. et al. (Sept. 2015). "Measurement of the Nodal Precession of WASP-33 b via Doppler Tomography". In: 810, L23, p. L23. DOI: 10.1088/2041-8205/810/2/L23. arXiv: 1508.02398 [astro-ph.EP].

Johnson, Marshall C. et al. (July 2014). "A Misaligned Prograde Orbit for Kepler-13 Ab via Doppler Tomography". In: 790.1, 30, p. 30. DOI: 10.1088/0004-637X/790/1/30. arXiv: 1406.0512 [astro-ph.EP].

Johnson, Marshall Caleb (2013). "Doppler tomographic observations of exoplanetary transits". In:

Kipping, D. M. (Nov. 2013). "Efficient, uninformative sampling of limb darkening coefficients for two-parameter laws". In: 435, pp. 2152–2160. DOI: 10.1093/mnras/stt1435. arXiv: 1308.0009 [astro-ph.SR].

Knutson, Heather A. et al. (Apr. 2014). "Friends of Hot Jupiters. I. A Radial Velocity Search for Massive, Long-period Companions to Close-in Gas Giant Planets". In: 785.2, 126, p. 126. DOI: 10.1088/0004-637X/785/2/126. arXiv: 1312.2954 [astro-ph.EP].

Kochukhov, O., V. Makaganiuk, and N. Piskunov (Dec. 2010). "Least-squares deconvolution of the stellar intensity and polarization spectra". In: 524, A5, A5. DOI: 10.1051/0004-6361/201015429. arXiv: 1008.5115 [astro-ph.SR].

Kovács, G. et al. (May 2013a). "Comprehensive time series analysis of the transiting extrasolar planet WASP-33b". In: 553, A44, A44. DOI: 10.1051/0004-6361/201219642. arXiv: 1205.5060 [astro-ph.EP].

Kovács, G. et al. (May 2013b). "Comprehensive time series analysis of the transiting extrasolar planet WASP-33b". In: 553, A44, A44. DOI: 10.1051/0004-6361/201219642. arXiv: 1205.5060 [astro-ph.EP].

Kozai, Y. (Nov. 1962). "Secular perturbations of asteroids with high inclination and eccentricity". In: 67, p. 591. DOI: 10.1086/108790.

Kuiper, Gerard P. (Jan. 1951). "On the Origin of the Solar System". In: *Proceedings of the National Academy of Science* 37.1, pp. 1–14. DOI: 10.1073/pnas.37.1.1.

Kupka, F. G. et al. (2000). "VALD-2 – The New Vienna Atomic Line Database". In: *Baltic Astronomy* 9, pp. 590–594.

Lai, Dong (June 2012). "Tidal dissipation in planet-hosting stars: damping of spin-orbit misalignment and survival of hot Jupiters". In: 423.1, pp. 486–492. DOI: 10.1111/j.1365-2966.2012.20893.x. arXiv: 1109.4703 [astro-ph.EP].

Lai, Dong, Francois Foucart, and Douglas N. C. Lin (Apr. 2011). "Evolution of spin direction of accreting magnetic protostars and spin-orbit misalignment in exoplanetary systems". In: 412.4, pp. 2790–2798. DOI: 10.1111/j.1365-2966.2010.18127.x. arXiv: 1008.3148 [astro-ph.EP].

Latham, D. W. et al. (May 1989). "The unseen companion of HD114762 - A probable brown dwarf". In: 339, pp. 38–40. DOI: 10.1038/339038a0.

Lehmann, H. et al. (June 2015). "Mass of WASP-33b". In: 578, L4, p. L4. DOI: 10.1051/0004-6361/201526176.

Lendl, M. et al. (Nov. 2020). "The hot dayside and asymmetric transit of WASP-189 b seen by CHEOPS". In: 643, A94, A94. DOI: 10.1051/0004-6361/202038677. arXiv: 2009.13403 [astro-ph.EP].

Lidov, M. L. (Oct. 1962). "The evolution of orbits of artificial satellites of planets under the action of gravitational perturbations of external bodies". In: 9.10, pp. 719–759. DOI: 10.1016/0032-0633(62)90129-0.

Lin, D. N. C., P. Bodenheimer, and D. C. Richardson (Apr. 1996). "Orbital migration of the planetary companion of 51 Pegasi to its present location". In: 380, pp. 606–607. DOI: 10.1038/380606a0.

Lin, D. N. C. and John Papaloizou (Oct. 1986). "On the Tidal Interaction between Protoplanets and the Protoplanetary Disk. III. Orbital Migration of Protoplanets". In: 309, p. 846. DOI: 10.1086/164653.

Mandel, Kaisey and Eric Agol (Dec. 2002). "Analytic Light Curves for Planetary Transit Searches". In: 580.2, pp. L171–L175. DOI: 10.1086/345520. arXiv: astro-ph/0210099 [astro-ph].

Marois, Christian et al. (Nov. 2008). "Direct Imaging of Multiple Planets Orbiting the Star HR 8799". In: *Science* 322.5906, p. 1348. DOI: 10.1126/science.1166585. arXiv: 0811.2606 [astro-ph].

Martínez, Romy Rodríguez et al. (Sept. 2020). "KELT-25 b and KELT-26 b: A Hot Jupiter and a Substellar Companion Transiting Young A Stars Observed by TESS". In: 160.3, 111, p. 111. DOI: 10.3847/1538-3881/ab9f2d.

Masuda, Kento (May 2015). "Spin-Orbit Angles of Kepler-13Ab and HAT-P-7b from Gravity-darkened Transit Light Curves". In: 805.1, 28, p. 28. DOI: 10.1088/0004-637X/805/1/28. arXiv: 1503.05446 [astro-ph.EP].

Mayor, M. et al. (Oct. 1995). "51 Pegasi". In: 6251.

McLaughlin, D. B. (July 1924). "Some results of a spectrographic study of the Algol system." In: 60. DOI: 10.1086/142826.

Moulton, F. R. (May 1899). "The limits of temporary stability of satellite motion, with an application to the question of the existence of an unseen body in the binary system 70 Ophiuchi". In: 20, pp. 33–37. DOI: 10.1086/103096.

Moya, A. et al. (Nov. 2011). "High spatial resolution imaging of the star with a transiting planet WASP-33". In: 535, A110, A110. DOI: 10.1051/0004-6361/201116889. arXiv: 1110.3160 [astro-ph.EP].

Nagasawa, M. and S. Ida (Dec. 2011). "Orbital Distributions of Close-in Planets and Distant Planets Formed by Scattering and Dynamical Tides". In: 742.2, 72, p. 72. DOI: 10.1088/0004-637X/742/2/72.

Nagasawa, M., S. Ida, and T. Bessho (May 2008). "Formation of Hot Planets by a Combination of Planet Scattering, Tidal Circularization, and the Kozai Mechanism". In: 678.1, pp. 498–508. DOI: 10.1086/529369. arXiv: 0801.1368 [astro-ph].

Narita, N. et al. (Oct. 2015). "MuSCAT: a multicolor simultaneous camera for studying atmospheres of transiting exoplanets". In: *Journal of Astronomical Telescopes, Instruments, and Systems* 1.4, 045001, p. 045001. DOI: 10.1117/1.JATIS.1.4.045001. arXiv: 1509.03154 [astro-ph.IM].

Narita, Norio et al. (Jan. 2019). "MuSCAT2: four-color simultaneous camera for the 1.52-m Telescopio Carlos Sánchez". In: *Journal of Astronomical Telescopes, Instruments, and Systems* 5, 015001, p. 015001. DOI: 10.1117/1.JATIS.5.1.015001. arXiv: 1807.01908 [astro-ph.IM].

Nelson, Richard P. et al. (Oct. 2000). "The migration and growth of protoplanets in protostellar discs". In: 318.1, pp. 18–36. DOI: 10.1046/j.1365-8711.2000.03605.x. arXiv: astro-ph/9909486 [astro-ph].

Noguchi, Kunio et al. (Dec. 2002). "High Dispersion Spectrograph (HDS) for the Subaru Telescope". In: *Publications of the Astronomical Society of Japan* 54.6, pp. 855–864. ISSN: 0004-6264. DOI: 10.1093/pasj/54.6.855. eprint: http://oup.prod.sis.lan/pasj/article-pdf/54/6/855/17446863/pasj54-0855.pdf. URL: https://doi.org/10.1093/pasj/54.6.855.

Parviainen, Hannu and Suzanne Aigrain (Nov. 2015). "ldtk: Limb Darkening Toolkit". In: *MNRAS* 453.4, pp. 3821–3826. DOI: 10.1093/mnras/stv1857. URL: http://mnras.oxfordjournals.org/lookup/doi/10.1093/mnras/stv1857.

Pepper, Joshua, Andrew Gould, and D. L. Depoy (June 2004). "KELT: The Kilodegree Extremely Little Telescope". In: *The Search for Other Worlds*. Ed. by Stephen S. Holt and Drake Deming. Vol. 713. American Institute of Physics Conference Series, pp. 185–188. DOI: 10.1063/1.1774522. arXiv: astro-ph/0401220 [astro-ph].

Petrovich, Cristobal (Jan. 2015). "Steady-state Planet Migration by the Kozai-Lidov Mechanism in Stellar Binaries". In: 799.1, 27, p. 27. DOI: 10.1088/0004-637X/799/1/27. arXiv: 1405.0280 [astro-ph.EP].

Queloz, D. et al. (July 2000). "Detection of a spectroscopic transit by the planet orbiting the star HD209458". In: 359, pp. L13–L17. eprint: astro-ph/0006213.

Queloz, D. et al. (July 2010). "WASP-8b: a retrograde transiting planet in a multiple system". In: 517, L1, p. L1. DOI: 10.1051/0004-6361/201014768. arXiv: 1006.5089 [astro-ph.EP].

Ragozzine, Darin and Aaron S. Wolf (June 2009). "Probing the Interiors of very Hot Jupiters Using Transit Light Curves". In: 698.2, pp. 1778–1794. DOI: 10.1088/0004-637X/698/2/1778. arXiv: 0807.2856 [astro-ph].

Rasio, Frederic A. and Eric B. Ford (Nov. 1996). "Dynamical instabilities and the formation of extrasolar planetary systems". In: *Science* 274, pp. 954–956. DOI: 10.1126/science.274.5289.954.

Rice, J. B. (July 2002). "Doppler imaging of stellar surfaces - techniques and issues". In: *Astronomische Nachrichten* 323, pp. 220–235. DOI: 10.1002/1521-3994(200208)323:3/4<220::AID-ASNA220>3.0.CO;2-P.

Ricker, G. R. et al. (July 2016). "The Transiting Exoplanet Survey Satellite". In: *Space Telescopes and Instrumentation 2016: Optical, Infrared, and Millimeter Wave*. Vol. 9904. Society of Photo-Optical Instrumentation Engineers (SPIE) Conference Series, 99042B. DOI: 10.1117/12.2232071.

Rossiter, R. A. (July 1924). "On the detection of an effect of rotation during eclipse in the velocity of the brigher component of beta Lyrae, and on the constancy of velocity of this system." In: 60. DOI: 10.1086/142825.

Ryu, Tsuguru (2018). "Direct Imaging of Intermediate Mass Giants with RV Trends". PhD thesis. The Graduate University for Advanced Studies, SOKENDAI.

Safronov, V. S. (1972). *Evolution of the protoplanetary cloud and formation of the earth and planets.*

Salvatier, John, Thomas V Wiecki, and Christopher Fonnesbeck (2016). "Probabilistic programming in Python using PyMC3". In: *PeerJ Computer Science* 2, e55.

Sanchis-Ojeda, Roberto and Joshua N. Winn (Dec. 2011). "Starspots, Spin-Orbit Misalignment, and Active Latitudes in the HAT-P-11 Exoplanetary System". In: 743.1, 61, p. 61. DOI: 10.1088/0004-637X/743/1/61. arXiv: 1107.2920 [astro-ph.EP].

Santerne, A. et al. (Aug. 2012). "SOPHIE velocimetry of Kepler transit candidates. VI. An additional companion in the KOI-13 system". In: 544, L12, p. L12. DOI: 10.1051/0004-6361/201219899. arXiv: 1207.1715 [astro-ph.EP].

Santerne, A. et al. (Nov. 2014). "SOPHIE velocimetry of Kepler transit candidates. XII. KOI-1257 b: a highly eccentric three-month period transiting exoplanet". In: 571, A37, A37. DOI: 10.1051/0004-6361/201424158. arXiv: 1406.6172 [astro-ph.EP].

Seager, S. (2010). *Exoplanets*.

See, T. J. J. (Sept. 1896). "Micrometrical measures of the stellar system, 70 Ophiuchi". In: 16, pp. 211–211. DOI: 10.1086/102529.

Smith, A. M. S. et al. (Sept. 2011). "Thermal emission from WASP-33b, the hottest known planet". In: 416.3, pp. 2096–2101. DOI: 10.1111/j.1365-2966.2011.19187.x. arXiv: 1101.2432 [astro-ph.EP].

Southworth, John (Nov. 2011). "Homogeneous studies of transiting extrasolar planets - IV. Thirty systems with space-based light curves". In: 417.3, pp. 2166–2196. DOI: 10.1111/j.1365-2966.2011.19399.x. arXiv: 1107.1235 [astro-ph.EP].

Spalding, C. and K. Batygin (Oct. 2016). "Spin-Orbit Misalignment as a Driver of the Kepler Dichotomy". In: 830, 5, p. 5. DOI: 10.3847/0004-637X/830/1/5. arXiv: 1607.03999 [astro-ph.EP].

Struve, O. (Oct. 1952). "Proposal for a project of high-precision stellar radial velocity work". In: *The Observatory* 72, pp. 199–200.

Szabó, G. M. et al. (July 2011). "Asymmetric Transit Curves as Indication of Orbital Obliquity: Clues from the Late-type Dwarf Companion in KOI-13". In: 736, L4, p. L4. DOI: 10.1088/2041-8205/736/1/L4. arXiv: 1105.2524 [astro-ph.EP].

Takahashi, Yasuhiro (2014). "Study of Exoplanet Migration Mechanisms with the Direct Imaging Method". PhD thesis. University of Tokyo.

Tamura, M. (Feb. 2016). "SEEDS - Strategic explorations of exoplanets and disks with the Subaru Telescope -". In: *Proceeding of the Japan Academy, Series B* 92, pp. 45–55. DOI: 10.2183/pjab.92.45.

Toomre, A. (May 1964). "On the gravitational stability of a disk of stars." In: 139, pp. 1217–1238. DOI: 10.1086/147861.

Tull, R. G. et al. (Mar. 1995). "The high-resolution cross-dispersed echelle white-pupil spectrometer of the McDonald Observatory 2.7-m telescope". In: 107, pp. 251–264. DOI: 10.1086/133548.

van de Kamp, P. (Sept. 1963). "Astrometric study of Barnard's star from plates taken with the 24-inch Sproul refractor." In: 68, pp. 515–521. DOI: 10.1086/109001.

von Essen, C. et al. (2014). "Pulsation analysis and its impact on primary transit modeling in WASP-33". In: 561, A48, A48. DOI: 10.1051/0004-6361/201322453. arXiv: 1311.3614 [astro-ph.EP].

von Essen, C. et al. (Feb. 2019). "An optical transmission spectrum of the ultra-hot Jupiter WASP-33 b. First indication of aluminum oxide in an exoplanet". In: 622, A71, A71. DOI: 10.1051/0004-6361/201833837. arXiv: 1811.02573 [astro-ph.EP].

Walker, G. A. H. et al. (Aug. 1995). "A search for Jupiter-mass companions to nearby stars." In: 116, pp. 359–375. DOI: 10.1006/icar.1995.1130.

Ward, W. R. (July 1986). "Density waves in the solar nebula: Diffential Lindblad torque". In: 67.1, pp. 164–180. DOI: 10.1016/0019-1035(86)90182-X.

Winn, J. N. et al. (Aug. 2010). "Hot Stars with Hot Jupiters Have High Obliquities". In: 718, pp. L145–L149. DOI: 10.1088/2041-8205/718/2/L145. arXiv: 1006.4161 [astro-ph.EP].

Winn, Joshua N. et al. (Aug. 2007). "Spin-Orbit Alignment for the Eccentric Exoplanet HD 147506b". In: 665.2, pp. L167–L170. DOI: 10.1086/521362. arXiv: 0707.0503 [astro-ph].

Winn, Joshua N. et al. (Feb. 2011). "Orbital Orientations of Exoplanets: HAT-P-4b is Prograde and HAT-P-14b is Retrograde". In: 141.2, 63, p. 63. DOI: 10.1088/0004-6256/141/2/63. arXiv: 1010.1318 [astro-ph.EP].

Wright, J. T. and J. D. Eastman (Sept. 2014). "Barycentric Corrections at 1 cm s^{-1} for Precise Doppler Velocities". In: 126, p. 838. DOI: 10.1086/678541. arXiv: 1409.4774 [astro-ph.IM].

Wu, Y. and N. Murray (May 2003). "Planet Migration and Binary Companions: The Case of HD 80606b". In: 589.1, pp. 605–614. DOI: 10.1086/374598. arXiv: astro-ph/0303010 [astro-ph].

Wu, Yanqin, Norman W. Murray, and J. Michael Ramsahai (Nov. 2007). "Hot Jupiters in Binary Star Systems". In: 670.1, pp. 820–825. DOI: 10.1086/521996. arXiv: 0706.0732 [astro-ph].

Zahn, J. P. (May 1977). "Reprint of 1977A&A....57..383Z. Tidal friction in close binary stars." In: 500, pp. 121–132.